國立臺灣大學理學院物理學研究所

碩士論文

Department of Physics

College of Science

National Taiwan University

Master's Thesis

波導量子電動力學中的超導人造原子波混頻研究

Wave Mixing via a Superconducting Artificial Atom in Waveguide Quantum Electrodynamics

謝子研

Tzu-Yen Hsieh

指導教授：林俊達博士

Advisor: Guin-Dar Lin, Ph.D.

中華民國 114 年 8 月

August 2025

doi:10.6342/NTU202503909

doi:10.6342/NTU202503909

國立臺灣大學碩士學位論文
口試委員會審定書
MASTER'S THESIS ACCEPTANCE CERTIFICATE
NATIONAL TAIWAN UNIVERSITY

波導量子電動力學中的超導人造原子波混頻研究

Wave Mixing via a Superconducting Artificial Atom in Waveguide Quantum Electrodynamics

本論文係謝子研(R10222008)在國立臺灣大學物理學研究所完成之碩士學位論文，於民國 114 年 7 月 11 日承下列考試委員審查通過及口試及格，特此證明。

The undersigned, appointed by the Department of Physics, National Taiwan University on 11 July, 2025, have examined a Master's thesis entitled above presented by Tzu-Yen Hsieh candidate and hereby certify that it is worthy of acceptance.

口試委員 Oral examination committee:

林俊達	林晏詳	仇祥華
（指導教授 Advisor）		
許耀銓		

doi:10.6342/NTU202503909

doi:10.6342/NTU202503909

致謝

在本論文完成之際，謹向所有在研究過程中給予我指導與協助的師長、學長姐與同儕致上最深的感謝。

首先，誠摯感謝指導教授林俊達教授在整個研究期間的耐心指導與支持。每當我在研究中遇到困難時，教授總能適時提供關鍵的方向與建議，讓我得以釐清思路、繼續推進研究，對本論文的完成有著至關重要的幫助。

我也衷心感謝林冠廷學長一路以來的協助與指導。從我對研究一無所知開始，學長便細心地引導我進入研究的世界，無論是基礎觀念的建立、問題的思考方式，還是實際操作與撰寫，學長的幫助都讓我受益良多，逐步建立起做研究的能力。

同時，也感謝李鎮宇學長與許婷學姊在研究期間提供許多實用建議與鼓勵，幫助我更快解決問題。

在實驗合作方面，感謝許耀銓教授與 Mr. Fahad 的協助與交流，提供實驗資料與重要的技術背景，使本研究能與實驗相互印證。

此外，也謝謝劉鎮瑜、許瑾懷、洪秉宏與李欣璉等同學在研究生活中的陪伴與討論，讓整個過程不再孤單，多了許多珍貴的回憶。

誠摯感謝本次口試委員撥冗審閱本論文，並提供寶貴的意見與建議，使本論文得以更加完善。

最後，感謝我的家人始終如一的支持與理解，是我能夠安心投入研究、完成學業的重要力量。

doi:10.6342/NTU202503909

doi:10.6342/NTU202503909

摘要

在本論文中，我們以理論方式研究一維波導量子電動力學系統中的量子波混頻現象。該系統是由一個多能階 transmon 同時受到兩組相干微波場的驅動所組成。我們結合 Floquet 理論與 Dyson 展開，系統性地分析導致頻譜邊帶產生的多光子過程。本研究架構顯示，透過調控兩組驅動場的相對功率與失諧量，可以實現可調式頻率轉換，從而產生可調式頻率梳。進一步地，當我們將 transmon 的更高能階納入考量時，發現新的量子途徑會對頻譜響應產生顯著影響。根據本理論進行的數值模擬結果與實驗頻譜高度吻合，驗證了我們方法的正確性。本研究成果對於發展量子光子元件具有重要意義，包括頻率轉換器、具頻率選擇性的光子路由器，以及片上光源等。

中文關鍵字**:** 量子波混頻、頻率轉換、相干控制、多能階人工原子、Floquet 分析

doi:10.6342/NTU202503909

doi:10.6342/NTU202503909

Abstract

In this thesis, we theoretically investigate quantum wave mixing in a one-dimensional waveguide quantum electrodynamics (QED) system comprising a multi-level transmon qubit driven by two coherent microwave fields. By combining Floquet theory with Dyson series formalism, we systematically analyze the multi-photon processes responsible for generating spectral sidebands. Our framework shows that frequency conversion can be engineered by tuning the relative powers and detunings of the driving fields, enabling the creation of tunable and symmetric frequency combs. By including higher energy levels of the transmon, we identify new quantum pathways that significantly affect the spectral response. Numerical simulations based on our theory show excellent agreement with experimental spectra, validating our approach. These findings provide valuable insights for the development of quantum photonic devices such as frequency converters, frequency-selective photon routers, and on chip light sources.

Keywords: quantum wave mixing, frequency conversion, coherent control, multi-level artificial atom, Floquet analysis

doi:10.6342/NTU202503909

doi:10.6342/NTU202503909

Contents

doi:10.6342/NTU202503909

doi:10.6342/NTU202503909

doi:10.6342/NTU202503909

doi:10.6342/NTU202503909

List of Figures

doi:10.6342/NTU202503909

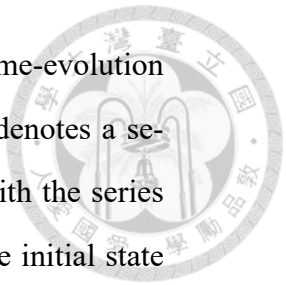

doi:10.6342/NTU202503909

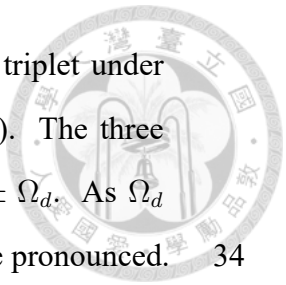

doi:10.6342/NTU202503909

doi:10.6342/NTU202503909

doi:10.6342/NTU202503909

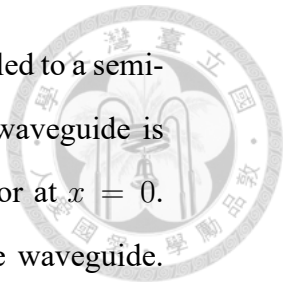

doi:10.6342/NTU202503909

List of Tables

doi:10.6342/NTU202503909

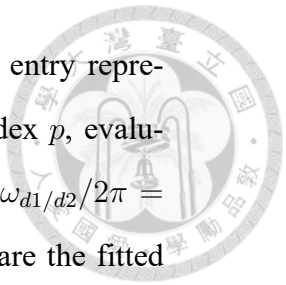

doi:10.6342/NTU202503909

Chapter 1

Introduction

1.1 Motivation

Controlling the interaction between light and matter at the quantum level is essential for realizing key functionalities in quantum technologies, including quantum communication, computing, and metrology [3, 4, 5, 6, 7, 8]. In these applications, light is widely used as a carrier of quantum information, thus necessitating the ability to generate and manipulate specific quantum states, such as entangled photons and single-photon states [9, 10, 11, 12], and precise engineering of their frequency and temporal properties through frequency conversion [13, 14, 15]. Such operations inherently rely on nonlinear light–matter interactions, which mediate effective photon–photon coupling, enable quantum interference, and support coherent transformation between frequency modes [16, 17, 18]. A particularly important mechanism for implementing these nonlinear interactions is wave mixing [19, 20].

Realizing wave mixing at the quantum level requires strong interaction between light and matter [21]. In conventional three-dimensional (3D) systems involving natural atoms, achieving such interactions is challenging because atoms emit light isotropically, while the incident field typically occupies only a limited number of spatial modes [22, 23]. This spatial mode mismatch significantly weakens the light–matter interaction. To overcome this limitation, the electromagnetic field can be confined to a one-dimensional (1D) waveguide, thereby enabling strong light–atom interactions [24, 25, 26]. This configuration

doi:10.6342/NTU202503909

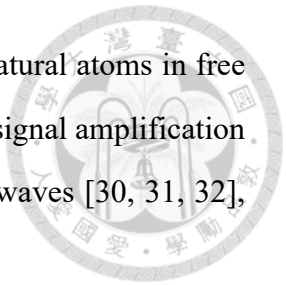

opens access to regimes that are difficult or even inaccessible with natural atoms in free space, such as elastic and inelastic scattering of photons [25, 27, 28], signal amplification without population inversion [29], non-reciprocal transport of microwaves [30, 31, 32], and collective Lamb shift [33, 34, 35, 36], among others.

Within this architecture, wave-mixing processes have been investigated using two- or three-level artificial atoms, typically under resonant or symmetrically detuned driving at weak to moderate power levels [37, 38, 39, 40, 41, 42]. These studies have demonstrated fundamental nonlinear effects such as sum- and difference-frequency generation [39, 43], as well as the influence of photon statistics on spectral properties [40, 41, 42, 44, 45].

More recent research suggests that higher energy levels can play a significant role in light–atom interaction applications under intense driving conditions [2, 29]. However, the influence of these higher levels on wave-mixing processes under strong driving remains unexplored. This gap motivates us to investigate wave mixing beyond the low- and moderate-power regimes commonly considered in the literature [46], which forms a central focus of this thesis. Specifically, we study three key topics:

1. The origin of sidebands arising from quantum dynamics.

2. The control of sideband asymmetry by tuning the relative strengths of the two driving fields.

3. The enhancement of wave mixing by higher transmon levels compared to few-level approximations.

In the remainder of this chapter, we provide the theoretical and conceptual foundations necessary for analyzing wave mixing in superconducting systems. Sec. 1.2 introduces superconducting artificial atoms, with a focus on the transmon. Sec. 1.3 reviews classical and quantum wave-mixing processes. Sec. 1.4 presents the open quantum system framework, including the master equations used in our analysis. Finally, Sec. 1.5 summarizes the overall structure of this thesis.

doi:10.6342/NTU202503909

1.2 Superconducting Atoms

Superconducting atoms are artificial quantum systems based on Josephson junctions, fabricated on micron-scale chips. These systems exhibit discrete energy levels analogous to those of natural atoms, but with the added benefits of design flexibility and experimental controllability [47, 48]. Their ability to strongly interact with microwave photons has opened the door to a wide range of quantum optical phenomena on a chip, leading to the development of circuit quantum electrodynamics (circuit QED) [49, 50], a platform for exploring light–matter interaction at the quantum level.

In the following sections, we introduce the physical origin of nonlinearity in Josephson junctions (Sec. 1.2.1), and present the transmon artificial atom (Sec. 1.2.2), a widely used architecture in circuit QED experiments.

1.2.1 Josephson Junction: a Nonlinear Inductor

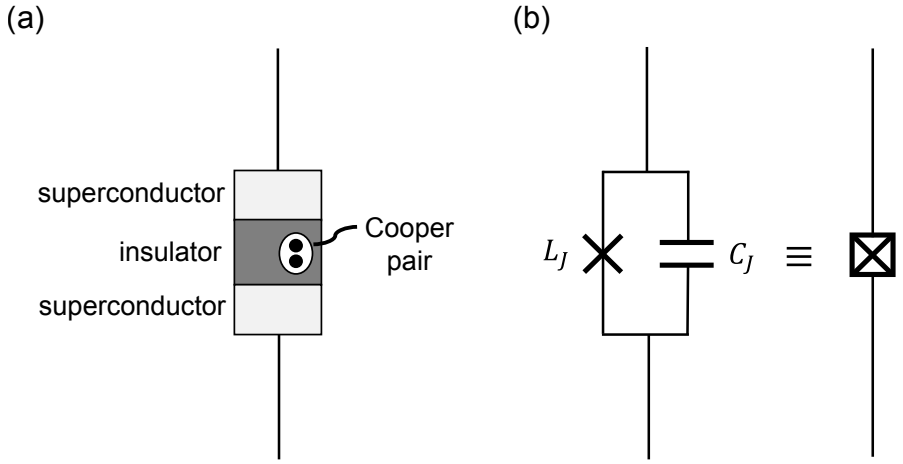

Figure 1.1: The Josephson junction. (a) Schematic diagram of a Josephson junction, consisting of two superconducting layers separated by an insulating barrier. The Cooper pairs can pass through the insulating layer via quantum tunneling, forming a supercurrent. (b) The standard circuit representation of a Josephson junction. The right side shows the conventional circuit symbol, a cross inside a square box, indicating the presence of both the Josephson element and the junction capacitance C_J. The left side shows the equivalent circuit model, where the junction is decomposed into a nonlinear Josephson inductance L_J and a junction capacitance C_J, forming a nonlinear parallel LC oscillator.

A Josephson junction consists of two superconductors separated by a thin insulator as illustrated in Fig. 1.1(a). In a superconductor, electrons form bound pairs known as Cooper

doi:10.6342/NTU202503909

pairs [51, 52]. Despite the presence of the potential barrier created by the insulator, these Cooper pairs can tunnel through the barrier via the quantum tunneling effect [52]. The resulting tunneled current is a dissipationless supercurrent $I(t)$, which is governed by the Josephson relations [52, 53]:

$$I(t) = I_c \sin\varphi(t), \tag{1.2.1}$$

$$\frac{d\varphi(t)}{dt} = \frac{2|e|}{\hbar} V(t), \tag{1.2.2}$$

where I_c is the critical current, $\varphi(t)$ the superconducting phase difference, and $V(t)$ the voltage across the junction. The fact or $2|e|$ corresponds to the charge of a Cooper pair. Applying the chain rule,

$$\frac{dI\,(t)}{dt} = \frac{dI\,(t)}{d\phi} \cdot \frac{d\phi}{dt}, \tag{1.2.3}$$

the voltage can be recast as

$$V(t) = L_J \frac{dI}{dt}, \tag{1.2.4}$$

which resembles the voltage-current relation for an inductor in classical circuit theory [54, 55]. From this perspective, the Josephson junction behaves like an electrical circuit consisting of a nonlinear inductor with inductance $L_J = \hbar/2|e|I_c \cos\varphi$ along with an intrinsic capacitor C_J [56].

The total energy of this junction is given by

$$E_{JJ} = E_{C_J} + E_{L_J}, \tag{1.2.5}$$

doi:10.6342/NTU202503909

where $E_{L_J} = -E_J \cos\varphi$ represents the energy stored in the nonlinear inductor and the Josephson energy is $E_J = \hbar I_c/2|e|$. The capacitive energy is $E_{C_J} = 2n^2e^2/C_J$ and n denotes the net number of Cooper pairs accumulated on the superconducting electrode connected to the junction. Following the standard quantization procedure [54, 56], we replace n and φ with quantum operator $\hat{n}$ and $\hat{\varphi}$, which satisfy the canonical commutation relation [56]:

$$[\hat{\varphi}, \hat{n}] = -i. \tag{1.2.6}$$

This leads to the quantum Hamiltonian of the Josephson junction:

$$\hat{H}_{JJ} = \frac{2e^2}{C_J}\hat{n}^2 - E_J \cos\hat{\varphi}. \tag{1.2.7}$$

1.2.2 Transmon Artificial Atom

Building on the nonlinear properties of the Josephson junction described in the previous section, one can implement external control by embedding it into a suitably designed superconducting circuit, as shown in Fig. 1.2(a). This allows us to tune the energy levels via gate voltage and circuit parameters. The total capacitance $C_\Sigma = C_J + C_g$ determines the charging energy $E_C = e^2/2C_\Sigma$. The Hamiltonian is

$$\hat{H} = 4E_C\left(\hat{n} - n_g\right)^2 - E_J \cos\hat{\varphi}. \tag{1.2.8}$$

The eigenenergies of the Hamiltonian Eq. (1.2.8) are periodic functions of the offset charge n_g [21], as shown in Fig. 1.2(b). In practice, the offset charge n_g inevitably fluctuates due to background noise, such as that caused by stray electric fields or material imperfections [57]. These fluctuations lead to variations in the transition frequencies, resulting in decoherence. To suppress the sensitivity to charge noise, the transmon is typically operated in the regime $E_J/E_C \gg 1$, where the Josephson energy dominates and forms a deep poten-

doi:10.6342/NTU202503909

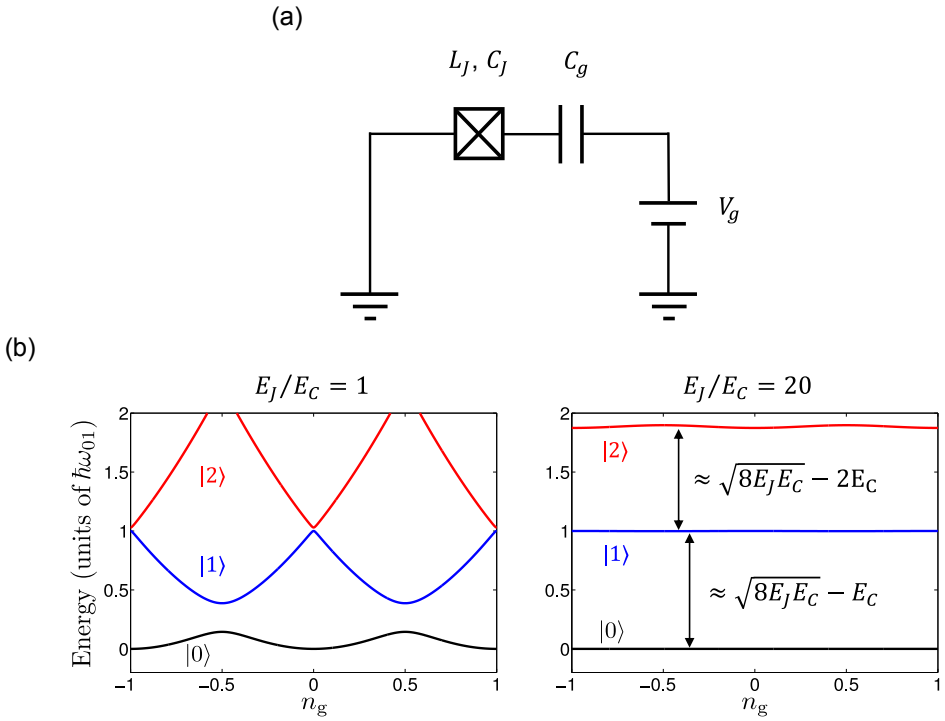

Figure 1.2: The standard transmon circuit and its energy-level configuration. (a) A transmon circuit consists of a small superconducting island connected to ground through a Josephson junction, characterized by a nonlinear inductance L_J and capacitance C_J. A gate capacitor C_g allows external control via the gate voltage V_g, which influences the charge states on the island. (b) First three energy levels as a function of the offset charge n_g. The left panel corresponds to the regime $E_J/E_C = 1$, where the energy levels depend strongly on n_g. The right panel shows the transmon regime $E_J/E_C = 20$, where the levels become nearly independent of n_g due to phase localization. Here, $\hbar\omega_{10}$ denotes the energy difference between the ground and first excited state, defined at integer values of n_g. (retrieved from Ref. [1])

doi:10.6342/NTU202503909

tial well around $\varphi = 0$ (and other points $\varphi = 2\pi N$, with $N \in \mathbb{Z}$). This localizes the phase and makes the energy levels nearly independent of n_g [21, 58, 59].

In this limit, the Hamiltonian can be approximated by expanding the cosine potential:

$$\hat{H} \approx 4E_C\hat{n}^2 + \frac{E_J}{2}\hat{\varphi}^2 - \frac{E_J}{24}\hat{\varphi}^4 + \mathcal{O}(\hat{\varphi}^6). \tag{1.2.9}$$

The first two terms describe a harmonic oscillator, resulting in equally spaced energy levels with spacing $\sqrt{8E_CE_J}$ [21, 58]. The quartic term introduces anharmonicity, yielding the following expression for the energy levels [21]:

$$E_m \approx \sqrt{8E_JE_C}\left(m + \frac{1}{2}\right) - \frac{E_C}{12}\left(6m^2 + 6m + 3\right), \tag{1.2.10}$$

where m is the energy level index. The first transition energy shifted by an anharmonicity

$$\alpha \equiv E_{m+1,m} - E_{m,m-1} \approx -E_C. \tag{1.2.11}$$

Such anharmonicity is essential for enabling selective qubit control and, more broadly, allows the transmon to serve as a controllable quantum system for exploring nonlinear phenomena in quantum optics and wave mixing.

1.3 Nonlinear Optics: Wave-Mixing Processes

A wave-mixing process refers to the generation of new frequency components when two or more electromagnetic waves interact with a nonlinear material, typically resulting in the creation of sum and difference frequencies.

In the following sections, we first present the classical description based on nonlinear polarization and Maxwell's equations (Sec. 1.3.1). We then introduce the basic concepts of quantum wave mixing via atom–field interactions (Sec. 1.3.2).

doi:10.6342/NTU202503909

1.3.1 Classical Wave-Mixing Processes

From a classical perspective, wave-mixing process arises when the polarization **P** of a medium responds nonlinearly to the applied electric field **E**. This polarization acts as a source term in Maxwell's equation:

$$\nabla^2\mathbf{E} - \mu_0\epsilon_0\frac{\partial^2\mathbf{E}}{\partial t^2} = \mu_0\frac{\partial^2\mathbf{P}}{\partial t^2}. \tag{1.3.1}$$

When **P** includes higher-order responses to the applied electric field **E**, the carrier frequency of the resultant electric fields differs from the incident frequency, resulting in the generation of new frequencies. To illustrate the underlying mechanism, we express the polarization **P** as [60]

$$\mathbf{P} = \epsilon_0\left(\chi^{(1)}\mathbf{E} + \chi^{(2)}\mathbf{E}^2 + \chi^{(3)}\mathbf{E}^3 + \dots\right), \tag{1.3.2}$$

where $\chi^{(n)}$ denotes the nth-order susceptibility tensor.

To illustrate the effect of nonlinear terms, let us begin with the lowest-order nonlinearity, represented by the second-order susceptibility $\chi^{(2)}$. This gives rise to three-wave mixing (TWM), a fundamental nonlinear process in which two input waves at frequencies ω_{d1} and ω_{d2} generate a third wave at ω_{new}. Consider an input signal:

$$E(t) = E_1 e^{i\omega_{d1}t} + E_2 e^{i\omega_{d2}t} + \text{c.c.}, \tag{1.3.3}$$

with E_1 and E_2 are amplitudes and c.c. denotes the complex conjugate, interacting with the a nonlinear material. The resultant waves are determined by the induced polarizations. The response of the first-order susceptibility tensor corresponds to the scattering of the incident waves [61], while the effect of the second-order tensor on the polarization is

doi:10.6342/NTU202503909

given by

$$\begin{aligned} P^{(2)}(t) &= \epsilon_0 \chi^{(2)} E^2 \\ &= E_1^2 e^{2i\omega_{d1}t} + E_2^2 e^{2i\omega_{d2}t} + 2E_1E_2 e^{i(\omega_{d1}+\omega_{d2})t} + 2E_1E_2^* e^{i(\omega_{d1}-\omega_{d2})t} + \text{c.c.}. \end{aligned} \tag{1.3.4}$$

This reveals new frequency components $2\omega_{d1}$, $2\omega_{d2}$ and $\omega_{d1} \pm \omega_{d2}$, corresponding to second-harmonic generation (SHG), sum-frequency generation (SFG), and difference-frequency generation (DFG) [60].

We now further consider the third-order response, in which case the input signal consists of three electric fields with frequencies ω_{d1}, ω_{d2}, and ω_{d3}. The frequencies ω_{new} of the resulting waves are given by

$$\begin{aligned} &3\omega_{d1},\ 3\omega_{d2},\ 3\omega_{d3}, \\ &\omega_{d1}+\omega_{d2}+\omega_{d3},\ \omega_{d1}+\omega_{d2}-\omega_{d3},\ \omega_{d1}+\omega_{d3}-\omega_{d2},\ \omega_{d2}+\omega_{d3}-\omega_{d1}, \\ &2\omega_{d1}\pm\omega_{d2},\ 2\omega_{d1}\pm\omega_{d3},\ 2\omega_{d2}\pm\omega_{d1},\ 2\omega_{d2}\pm\omega_{d3},\ 2\omega_{d3}\pm\omega_{d1},\ 2\omega_{d3}\pm\omega_{d2}. \end{aligned} \tag{1.3.5}$$

However, when only two distinct input frequencies are applied, the generated frequencies reduce to:

$$3\omega_{d1},\ 3\omega_{d2},\ 2\omega_{d1}\pm\omega_{d2},\ 2\omega_{d2}\pm\omega_{d1}. \tag{1.3.6}$$

Higher-order nonlinearities beyond $\chi^{(3)}$ can, in principle, generate even more frequencies. However, they typically require extremely high field strengths and are rarely significant in standard optical media. In practice, for typical materials, nonlinear optical effects are well described by the second- and third-order susceptibilities [60, 62].

doi:10.6342/NTU202503909

1.3.2 Quantum Wave-Mixing Processes

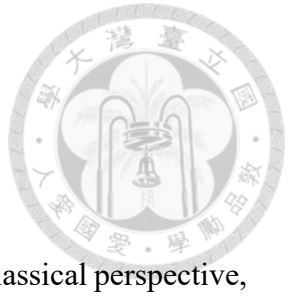

In the previous sections, we introduced wave-mixing process from a classical perspective, where the nonlinear effects of electric polarization play a significant role in determining the frequencies of the resulting electric fields. New frequencies arise from the nonlinear polarization response of a material, typically due to structural asymmetry and strong driving. At the quantum level, however, wave mixing arises from a subtler mechanism: the interaction between discrete atomic energy levels and quantized electromagnetic fields.

To illustrate this quantum process, we begin by examining a typical case where a M-level transmon coupled to two quantized radiation fields with frequency ω_{d1} and ω_{d2}. The Hamiltonian that describes this system is given by

$$H_{\text{int}}^{(I)}(t) = \sum_{i=1}^{2}\sum_{m=1}^{M-1} \hbar\sqrt{m}g_i\Big(a_i\sigma_{m,m-1}e^{-i\Delta_i^{(m)}t} + a_i^\dagger\sigma_{m-1,m}e^{i\Delta_i^{(m)}t}\Big), \tag{1.3.7}$$

where $\Delta_i^{(m)} = \omega_{di} - \omega_{m,m-1}$ denotes the detuning between the frequency of ith radiation field ($i = 1, 2$) and the transition frequency $\omega_{m,m-1} = \omega_m - \omega_{m-1}$ between mth and $(m-1)$th atomic energy level for $m = 1, 2, \cdots, M$. The coupling strength between the ith field and the mth atomic level is given by $\sqrt{m}g_i$ [47]. The operator a_i ($a_i^\dagger$) denotes the annihilation (creation) operator for the photonic mode of frequency ω_{di}, and atomic ladder operator $\sigma_{m,m-1} = \sigma_{m-1,m}^\dagger = |m\rangle\langle m-1|$. The superscript $^{(I)}$ indicates that the Hamiltonian is expressed in the interaction picture.

The dynamics of this system are governed by the Schrodinger equation:

$$i\hbar\frac{d}{dt}U(t;t_0) = H_{\text{int}}^{(I)}(t)\,U(t;t_0), \tag{1.3.8}$$

where $U(t;t_0)$ stands for the unitary time-evolution operator with initial condition $U(t_0;t_0) = \mathbb{I}_M$, and $\mathbb{I}_M$ denotes the $M \times M$ identity matirx. By expressing the time-evolution operator

doi:10.6342/NTU202503909

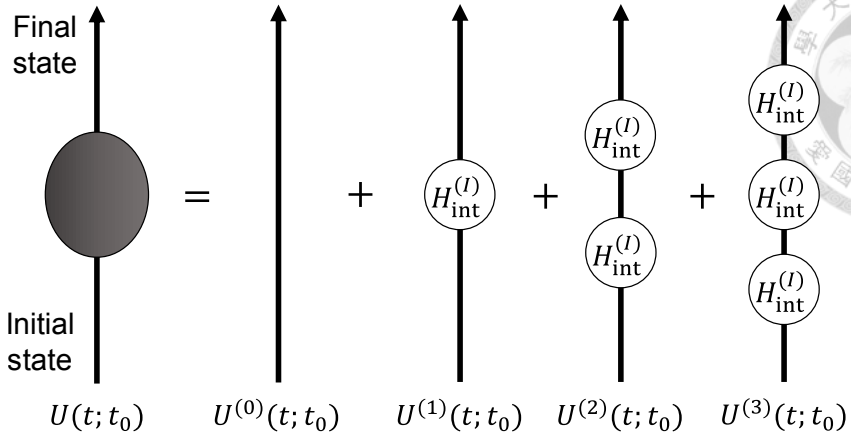

Figure 1.3: Diagrammatic representation of the Dyson series for the time-evolution operator in the interaction picture. Each vertical segment denotes a sequential application of the interaction Hamiltonian $H_{\text{int}}^{(I)}$, with the series summing over all possible orders of interaction events. The initial state evolves into the final state through these successive perturbative processes. Notably, wave-mixing processes first emerge at second order and beyond, where the time-ordered products of multiple $H_{\text{int}}^{(I)}$ at different times can generate new frequency components through interference between field modes.

as a power series in the coupling strength, we obtain the so-called Dyson series [63, 64]:

$$\begin{aligned} U(t;t_0) &= I - \frac{i}{\hbar}\int_{t_0}^{t} dt_1 H_{\text{int}}^{(I)}(t_1) + \left(-\frac{i}{\hbar}\right)^2 \int_{t_0}^{t} dt_1 \int_{t_0}^{t_1} dt_2\, H_{\text{int}}^{(I)}(t_1) H_{\text{int}}^{(I)}(t_2) + \cdots \\ &= \sum_{k=0}^{\infty} U^{(k)}(t;t_0). \end{aligned} \tag{1.3.9}$$

A schematic representation of this expansion is shown in Fig. 1.3, where each term $U^{(k)}(t;t_0)$ describes an interaction process involving n photon absorption or emission events, and its amplitude scales with the k-th power of the coupling strengths g_i.

It is important to note that while the Dyson series expansion is a powerful tool for treating weakly interacting systems, it becomes problematic when the driving frequency matches the transition frequency of the atom [64]. In such cases, the interaction Hamiltonian, Eq. (1.3.7), becomes time-independent, causing the Dyson series, Eq. (1.3.9), to diverge in the long-time limit when $g_i(t-t_0) \gg 1$. Physically, this divergence reflects the onset of strong population (Rabi) oscillations, which are inherently nonperturbative and cannot be accurately described by a perturbative expansion. However, since the purpose of this section is not to describe the full dynamics in detail, but rather to conceptually il-

doi:10.6342/NTU202503909

lustrate how wave mixing arises from multiphoton processes, such issues are beyond the scope of concern here.

We now illustrate the quantum wave-mixing process by examining the contributions of each term in the Dyson series, Eq. (1.3.9), under the condition $g_i(t-t_0) \ll 1$, which allows us to approximate the interaction Hamiltonian as nearly constant over $[t_0, t]$, by evaluating it at t.

The zeroth-order term is simply the identity operator,

$$U^{(0)}(t;t_0) = I, \tag{1.3.10}$$

representing free evolution. The first-order term is approximately given by

$$\begin{aligned} U^{(1)}(t;t_0) &\approx -\frac{i(t-t_0)}{\hbar} H_{\text{int}}^{(I)}(t) \\ &= -i \sum_{i=1}^{2} \sum_{m=1}^{M-1} \sqrt{m} g_i(t-t_0) \left(a_i \sigma_{m,m-1} e^{-i\Delta_i^{(m)} t} + a_i^\dagger \sigma_{m-1,m} e^{i\Delta_i^{(m)} t} \right). \end{aligned} \tag{1.3.11}$$

In this case, the wave-mixing process does not occur, as this term corresponds to only a single photon interaction, see Fig. 1.4(a). This suggests that higher-order terms are essential for describing quantum wave mixing. We now turn to the second-order term, which describes the absorption or emission of two photons at frequencies ω_{d1} and/or ω_{d2}. It is approximately:

$$\begin{aligned} U^{(2)}(t;t_0) \approx (-i)^2 \sum_{i,j=1}^{2} \sum_{m,n=1}^{M-1} & \sqrt{nm} g_j g_i (t-t_0)^2 \\ \times \Big(& a_j a_i \sigma_{n,n-1} \sigma_{m,m-1} e^{-i\Delta_j^{(n)} t} e^{-i\Delta_i^{(m)} t} \\ & + a_j^\dagger a_i \sigma_{n-1,n} \sigma_{m,m-1} e^{i\Delta_j^{(n)} t} e^{-i\Delta_i^{(m)} t} \\ & + a_j a_i^\dagger \sigma_{n,n-1} \sigma_{m-1,m} e^{-i\Delta_j^{(n)} t} e^{i\Delta_i^{(m)} t} \\ & + a_j^\dagger a_i^\dagger \sigma_{n-1,n} \sigma_{m-1,m} e^{i\Delta_j^{(n)} t} e^{i\Delta_i^{(m)} t} \Big). \end{aligned} \tag{1.3.12}$$

doi:10.6342/NTU202503909

In this expression, we observe four distinct terms, each corresponding to a different field–atom interaction process, as illustrated in Fig. 1.4(b):

- $a_j a_i \sigma_{n,n-1}\sigma_{m,m-1}$, describing the absorption of two photons with frequencies ω_{di} and ω_{dj}; the atom is excited upward by two energy levels (see Fig. 1.4(b), leftmost panel).

- $a_j^\dagger a_i \sigma_{n-1,n}\sigma_{m,m-1}$, describing the absorption of a photon with frequency ω_{di}, followed by emission of a photon with frequency ω_{dj}; the atom first moves up one level and then returns to its original state (see Fig. 1.4(b), second panel from the left).

- $a_j a_i^\dagger \sigma_{n,n-1}\sigma_{m-1,m}$, describing the emission of a photon with frequency ω_{di}, followed by absorption of a photon with frequency ω_{dj}; the atom first drops one level and then is excited back to the original level (see Fig. 1.4(b), third panel from the left).

- $a_j^\dagger a_i^\dagger \sigma_{n-1,n}\sigma_{m-1,m}$, describing the emission of two photons with frequencies ω_{di} and ω_{dj}; the atom relaxes downward by two energy levels (see Fig. 1.4(b), rightmost panel).

These terms include both self-mode and cross-mode processes. When $i = j$, they correspond to self-mixing, where the quantum state acquires a phase oscillating at frequency $2\omega_{d1}$ or $2\omega_{d2}$. When $i \neq j$, they enable mixing between the two modes, resulting in phase oscillations at frequency $\pm(\omega_{d1} - \omega_{d2})$ during the state's evolution.

For the higher-order terms, each additional order brings an extra factor of $g_i(t - t_0)$, making their contributions progressively smaller in the limit $g_i(t - t_0) \ll 1$. This implies that the probabilities for more complex multiphoton absorption/emission processes become negligible [41]. Therefore, in this section, we restrict our analysis to the second-order effects, which dominate the quantum wave-mixing process under weak coupling/short-time conditions.

In conclusion, quantum wave mixing arises from the interference between different photon modes mediated by the discrete energy levels. The atom serves as a nonlinear

doi:10.6342/NTU202503909

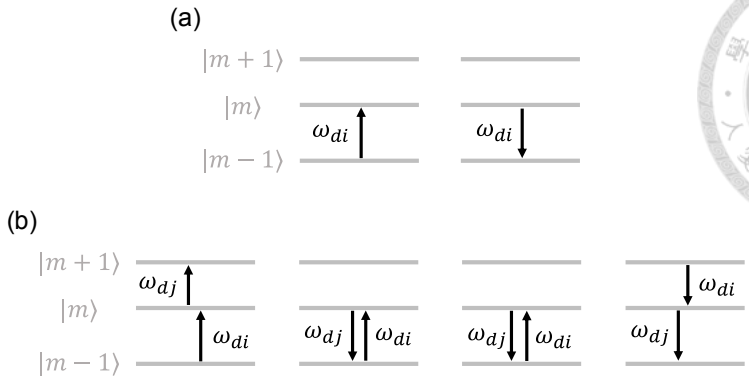

Figure 1.4: Illustration of quantum transitions contributing to wave-mixing processes. (a) First-order processes: single-photon absorption or emission at frequency ω_{di}, corresponding to transitions between adjacent levels. (b) Second-order processes: sequential two-photon absorption or emission involving frequencies ω_{di} and ω_{dj}. These processes can lead to interference and wave-mixing when both modes are involved.

element that enables these modes to interact, even in the absence of intrinsic material nonlinearity. Through successive transitions described by higher-order Dyson terms, multiphoton processes become possible, leading to the emergence of new frequency components.

1.4 Open Quantum System

In reality, physical systems are often not completely isolated from their surrounding. The interaction with the environment inevitably leads to decoherence and energy relaxation. In such cases, the system is referred to as an open quantum system, and its dynamics can no longer be described solely by the unitary Schrodinger equation.

In this section, following the standard approach [65, 66, 67], our objective is to address the dynamics of an open quantum system.

doi:10.6342/NTU202503909

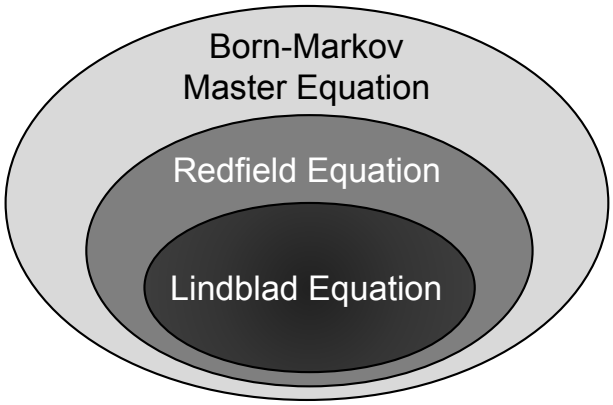

Figure 1.5: Hierarchical relationship among the master equations discussed in Sec. 1.4. The Born-Markov master equation, Eq. (1.4.14), refers to a class of approximations based on weak system-environment coupling and memoryless dynamics. The Redfield equation, Eq. (1.4.28), is a specific realization that retains coherence between all atomic transitions, including those with different transition frequencies. The Lindblad equation, Eq. (1.4.31), is a further simplification that applies a secular approximation, eliminating inter-transition coherences.

1.4.1 Born-Markov Master Equation

We consider a quantum system of interest interacting with an external environment. The total Hamiltonian in the Schrodinger picture is given by

$$H_{tot}^{(S)} = H_S^{(S)} \otimes I_B + I_S \otimes H_B^{(S)} + H_{int}^{(S)}. \tag{1.4.1}$$

Here, $H_{tot}^{(S)}$ acts on the total Hilbert space $\mathcal{H}_{tot}$, which is given by the tensor product of the system Hilbert space $\mathcal{H}_S$ and the environment Hilbert space $\mathcal{H}_B$, i.e., $\mathcal{H}_{tot} = \mathcal{H}_S \otimes \mathcal{H}_B$. Similarly, the system Hamiltonian $H_S^{(S)}$ operates on $\mathcal{H}_S$, while the environment Hamiltonian $H_B^{(S)}$ acts on $\mathcal{H}_B$. Throughout this chapter, the superscripts $^{(S)}$ and $^{(I)}$ denote the Schrodinger and interaction pictures respectively. The dynamics of the total system are governed by the Liouville-von Neumann equation, which describes the unitary evolution of the density matrix:

$$\frac{d\rho_{tot}^{(S)}(t)}{dt} = -\frac{i}{\hbar}[H_{tot}^{(S)}, \rho_{tot}^{(S)}(t)]. \tag{1.4.2}$$

doi:10.6342/NTU202503909

To simplify the analysis, we transform to the interaction picture, where oscillatory terms are removed:

$$\frac{d\rho_{tot}^{(I)}(t)}{dt} = -\frac{i}{\hbar}[H_{int}^{(I)}(t), \rho_{tot}^{(I)}(t)], \tag{1.4.3}$$

where the interaction-picture Hamiltonian and the density matrix are represented as

$$H_{int}^{(I)}(t) = U_{S\otimes B}(t) H_{int}^{(S)} U_{S\otimes B}^{\dagger}(t), \tag{1.4.4}$$

$$\rho_{tot}^{(I)}(t) = U_{S\otimes B}^{\dagger}(t) \rho_{tot}^{(S)}(t) U_{S\otimes B}(t), \tag{1.4.5}$$

with $U_{S\otimes B}(t) = e^{-\frac{i}{\hbar}(H_S^{(S)} + H_B^{(S)})t}$. Formally integrating Eq. (1.4.3) gives

$$\rho_{tot}^{(I)}(t) = \rho_{tot}^{(I)}(0) - \frac{i}{\hbar}\int_0^t dt' \Big[H_{int}^{(I)}(t'), \rho_{tot}^{(I)}(t')\Big]. \tag{1.4.6}$$

Substituting Eq. (1.4.6) into Eq. (1.4.3), we obtain

$$\frac{d\rho_{tot}^{(I)}(t)}{dt} = -\frac{i}{\hbar}\Big[H_{int}^{(I)}(t), \rho_{tot}^{(I)}(0)\Big] - \frac{1}{\hbar^2}\int_0^t \Big[H_{int}^{(I)}(t), \Big[H_{int}^{(I)}(t'), \rho_{tot}^{(I)}(t')\Big]\Big] dt'. \tag{1.4.7}$$

Since we are primarily interested in the dynamics of the system, we take the partial trace over the bath degrees of freedom to obtain

$$\begin{aligned}\frac{d\rho_S^{(I)}(t)}{dt} &= \mathrm{Tr}_B\left[\frac{d\rho_{tot}^{(I)}(t)}{dt}\right] \\ &= -\frac{i}{\hbar}\mathrm{Tr}_B\Big[H_{int}^{(I)}(t), \rho_{tot}^{(I)}(0)\Big] - \frac{1}{\hbar^2}\int_0^t \mathrm{Tr}_B\Big[H_{int}^{(I)}(t), \Big[H_{int}^{(I)}(t'), \rho_{tot}^{(I)}(t')\Big]\Big] dt'.\end{aligned} \tag{1.4.8}$$

The first term on the right-hand side of Eq. (1.4.8), $\mathrm{Tr}_B\Big[H_{int}^{(I)}(t), \rho_{tot}^{(I)}(0)\Big]$, is assumed to be zero under the assumption that the bath is in a symmetric equilibrium state. It is note that if the bath were initially in a non-equilibrium state, this assumption might no longer hold. To further simplify the derivation, we assume that the system-bath interaction is

doi:10.6342/NTU202503909

turned on at $t = 0$, resulting in a factorized initial state:

$$\rho_{tot}^{(I)}(0) = \rho_S^{(I)}(0) \otimes \rho_B^{(I)}(0), \tag{1.4.9}$$

where $\rho_S^{(I)}(0)$ and $\rho_B^{(I)}(0)$ are the initial density operators of the system and bath, respectively. We then consider a typical scenario in which the system–bath coupling is sufficiently weak that Eq. (1.4.8) can be truncated at second order. Additionally, we assume that the bath has a large number of degrees of freedom and remains approximately in thermal equilibrium. Applying these assumptions—known as the Born approximation—we obtain:

$$\rho_{tot}^{(I)}(t) \approx \rho_S^{(I)}(t) \otimes \rho_B. \tag{1.4.10}$$

By substituting Eq. (1.4.10) into Eq. (1.4.8), we have

$$\frac{d\rho_S^{(I)}(t)}{dt} = -\frac{1}{\hbar^2} \int_0^t \mathrm{Tr}_B \Big[H_{int}^{(I)}(t), \Big[H_{int}^{(I)}(t'), \rho_S^{(I)}(t') \otimes \rho_B \Big] \Big] dt'. \tag{1.4.11}$$

We observe that the integral involves the past states $\rho_S^{(I)}(t')$, meaning that the current evolution of the system depends on its entire history. As a consequence, the differential equation, Eq. (1.4.11), is difficult to solve. However, in most practical situations, the memory effect can be neglected. Thanks to the large number of bath degrees of freedom, the bath correlation time τ_B is much shorter than the characteristic system timescale τ_S. This separation of timescales justifies two key approximations:

$$\rho_S^{(I)}(t') \otimes \rho_B \to \rho_S^{(I)}(t) \otimes \rho_B, \tag{1.4.12}$$

$$\int_0^t dt' \to \int_0^\infty dt'. \tag{1.4.13}$$

Substituting Eq. (1.4.12) and Eq. (1.4.13) into Eq. (1.4.11) and changing the integration variable to $s = t - t'$, we get the Born-Markov master equation:

doi:10.6342/NTU202503909

$$\frac{d\rho_S^{(I)}(t)}{dt} = -\frac{1}{\hbar^2}\int_0^\infty \mathrm{Tr}_B\Big[H_{int}^{(I)}(t), \Big[H_{int}^{(I)}(t-s), \rho_S^{(I)}(t)\otimes\rho_B\Big]\Big]ds. \tag{1.4.14}$$

To better understand these approximations, we now consider a typical interaction Hamiltonian:

$$H_{int}^{(S)} = \hbar\sum_\alpha \left(S_\alpha^{(S)}\otimes B_\alpha^{(S)}\right), \tag{1.4.15}$$

where $S_\alpha^{(S)}$ and $B_\alpha^{(S)}$ are Hermitian operators acting on the Hilbert spaces ($\mathcal{H}_S$) and the bath ($\mathcal{H}_B$), respectively, through the coupling channel α.

Assuming the system has a discrete energy spectrum, the operator $S_\alpha^{(S)}$ can be decomposed in the basis of atomic bare states (i.e., the eigenstates of $H_S^{(S)}$) into components $S_{\alpha,\omega_a}^{(S)}$, each connecting eigenstate pairs whose energy difference is $\hbar\omega_a$:

$$S_\alpha^{(S)} = \sum_{\omega_a} S_{\alpha,\omega_a}^{(S)}, \tag{1.4.16}$$

with

$$S_{\alpha,\omega_a}^{(S)} = \sum_{E_m-E_n=\hbar\omega_a} \langle m|S_\alpha^{(S)}|n\rangle|m\rangle\langle n|. \tag{1.4.17}$$

To illustrate the meaning of the decomposition, Eq. (1.4.16), we consider a two-level system as an example. Let $|0\rangle$ and $|1\rangle$ be the ground and excited states, with energies E_0 and E_1. The operator $S_\alpha^{(S)}$ can then be decomposed into two terms: one corresponding to the downward transition $|1\rangle\langle 0|$ with frequency $\omega_a = (E_1 - E_0)/\hbar > 0$, and the other being its Hermitian conjugate $|0\rangle\langle 1|$, associated with $\omega_a = (E_0 - E_1)/\hbar < 0$.

To move to the interaction picture, we apply the following transformation:

$$S_{\alpha,\omega_a}^{(I)}(t) = e^{iH_St/\hbar}S_{\alpha,\omega_a}^{(S)}e^{-iH_St/\hbar} = e^{-i\omega_a t}S_{\alpha,\omega_a}^{(S)}, \tag{1.4.18}$$

doi:10.6342/NTU202503909

$$S^{(I)\dagger}_{\alpha,\omega_a}(t) = e^{iH_S t/\hbar} S^{(S)\dagger}_{\alpha,\omega_a} e^{-iH_S t/\hbar} = e^{i\omega_a t} S^{(S)\dagger}_{\alpha,\omega_a}. \tag{1.4.19}$$

Here, the Baker-Campbell-Hausdorff formula is used along with the following commutation relations:

$$[H_S, S^{(S)}_{\alpha,\omega_a}] = -\omega_a S^{(S)}_{\alpha,\omega_a}, \tag{1.4.20}$$

$$[H_S, S^{(S)\dagger}_{\alpha,\omega_a}] = +\omega_a S^{(S)\dagger}_{\alpha,\omega_a}, \tag{1.4.21}$$

which can be easily derived from Eq. (1.4.16). Applying Eq. (1.4.15), Eq. (1.4.18) and Eq. (1.4.19), the interaction Hamiltonian in the interacting picture is given by

$$H^{(I)}_{int}(t) = \hbar \sum_{\alpha,\omega_a} e^{-i\omega_a t} S^{(S)}_{\alpha,\omega_a} \otimes B^{(I)}_{\alpha}(t) = \hbar \sum_{\alpha,\omega_a} e^{+i\omega_a t} S^{(S)\dagger}_{\alpha,\omega_a} \otimes B^{(I)\dagger}_{\alpha}(t). \tag{1.4.22}$$

Substituting Eq. (1.4.22) into Eq. (1.4.14), we obtain:

$$\begin{aligned}
\frac{d\rho^{(I)}_S(t)}{dt} &= -\frac{1}{\hbar^2}\int_0^\infty \mathrm{Tr}_B\Big[H^{(I)}_{int}(t), \Big[H^{(I)}_{int}(t-s), \rho^{(I)}_S(t)\otimes\rho^{(I)}_B\Big]\Big] ds \\
&= \frac{1}{\hbar^2}\int_0^\infty \mathrm{Tr}_B\Big[H^{(I)}_{int}(t-s)\rho^{(I)}_S(t)\otimes\rho^{(I)}_B H^{(I)}_{int}(t) \\
&\qquad\qquad - H^{(I)}_{int}(t)H^{(I)}_{int}(t-s)\rho^{(I)}_S(t)\otimes\rho^{(I)}_B\Big] + h.c.\, ds \\
&= \int_0^\infty \sum_{\alpha,\beta}\sum_{\omega_a,\omega'_a} \Big\{ e^{-i(\omega_a-\omega'_a)t} e^{i\omega_a s} S^{(S)}_{\beta,\omega_a}\rho^{(I)}_S(t) S^{(S)\dagger}_{\alpha,\omega'_a} \mathrm{Tr}_B\Big[B^{(I)}_\beta(t-s)\rho^{(I)}_B B^{(I)\dagger}_\alpha(t)\Big] \\
&\qquad e^{-i(\omega_a-\omega'_a)t} e^{i\omega_a s} S^{(S)\dagger}_{\alpha,\omega'_a} S^{(S)}_{\beta,\omega_a}\rho^{(I)}_S(t) \mathrm{Tr}_B\Big[B^{(I)\dagger}_\alpha(t) B^{(I)}_\beta(t-s)\rho^{(I)}_B\Big]\Big\} + h.c.\, ds.
\end{aligned} \tag{1.4.23}$$

To quantify the bath-induced effects, we define

$$F_{\alpha\beta}(\nu;t) \equiv \int_0^\infty e^{i\nu s}\Big\langle B^{(I)\dagger}_\alpha(t) B^{(I)}_\beta(t-s)\Big\rangle ds, \tag{1.4.24}$$

doi:10.6342/NTU202503909

with the bath two-time correlation function is given by $\left\langle B_\alpha^{(I)\dagger}(t)B_\beta^{(I)}(t-s)\right\rangle = \mathrm{Tr}_B\left[B_\alpha^{(I)\dagger}(t)B_\beta^{(I)}(t-s)\rho_B^{(I)}\right]$. If the bath is in a stationary state (i.e. $\dot{\rho}_B(t)=0$), the two-time correlation function depends only on the time difference s, and $F_{\alpha\beta}(\nu;t)$ becomes independent of t. We now decompose $F_{\alpha\beta}(\nu)$ into

$$F_{\alpha\beta}(\nu) = \Gamma_{\alpha\beta}(\nu) + i\Delta_{\alpha\beta}(\nu), \tag{1.4.25}$$

where

$$\Gamma_{\alpha\beta}(\nu) = \frac{1}{2}\Big(F_{\alpha\beta}(\nu) + F^*_{\beta\alpha}(\nu)\Big) = \frac{1}{2}\int_{-\infty}^{\infty} e^{i\nu s}\Big\langle B_\alpha^{(I)\dagger}(s)B_\beta^{(I)}(0)\Big\rangle ds, \tag{1.4.26}$$

$$\Delta_{\alpha\beta}(\nu) = \frac{1}{2i}\Big(F_{\alpha\beta}(\nu) - F^*_{\beta\alpha}(\nu)\Big). \tag{1.4.27}$$

Here, the real part $\Gamma_{\alpha\beta}(\nu)$ describes dissipative effects like relaxation and dephasing, while the imaginary part $\Delta_{\alpha\beta}(\nu)$ accounts for energy shifts (the Lamb shift). Substituting this decomposition into the Eq. (1.4.23) and transform to the Schrodinger picture, we obtain

$$\frac{d\rho_S^{(S)}(t)}{dt} = -\frac{i}{\hbar}\left[H_S, \rho_S^{(S)}(t)\right] + \mathcal{L}_L\left[\rho_S^{(S)}(t)\right] + \mathcal{L}_D\left[\rho_S^{(S)}(t)\right], \tag{1.4.28}$$

where the superoperators $\mathcal{L}_L\left[\rho_S^{(S)}(t)\right]$ and $\mathcal{L}_D\left[\rho_S^{(S)}(t)\right]$ denote

$$\begin{aligned}\mathcal{L}_L\left[\rho_S^{(S)}(t)\right] = i\sum_{\alpha,\beta}\sum_{\omega_a,\omega'_a}\Big[&\big(\Delta_{\alpha\beta}(\omega_a) - \Delta_{\beta\alpha}(\omega'_a)\big)S^{(S)}_{\beta,\omega_a}\rho_S^{(S)}(t)S^{(S)\dagger}_{\alpha,\omega'_a} \\ &-\Delta_{\alpha\beta}(\omega_a)S^{(S)\dagger}_{\alpha,\omega'_a}S^{(S)}_{\beta,\omega_a}\rho_S^{(S)}(t) + \Delta_{\beta\alpha}(\omega'_a)\rho_S^{(S)}(t)S^{(S)\dagger}_{\alpha,\omega'_a}S^{(S)}_{\beta,\omega_a}\Big]\end{aligned} \tag{1.4.29}$$

doi:10.6342/NTU202503909

and

$$\mathcal{L}_D\left[\rho_S^{(S)}(t)\right] = \sum_{\alpha,\beta}\sum_{\omega_a,\omega_a'}\Big[\big(\Gamma_{\alpha\beta}(\omega_a)+\Gamma_{\beta\alpha}(\omega_a')\big)S^{(S)}_{\beta,\omega_a}\rho_S^{(S)}(t)S^{(S)\dagger}_{\alpha,\omega_a'} - \Gamma_{\alpha\beta}(\omega_a)S^{(S)\dagger}_{\alpha,\omega_a'}S^{(S)}_{\beta,\omega_a}\rho_S^{(S)}(t) - \Gamma_{\beta\alpha}(\omega_a')\rho_S^{(S)}(t)S^{(S)\dagger}_{\alpha,\omega_a'}S^{(S)}_{\beta,\omega_a}\Big]. \tag{1.4.30}$$

Equation (1.4.28) is known as the Redfield equation.

1.4.2 Lindblad Equation

The transition from Eq. (1.4.23) to Eq. (1.4.28) involves moving from the interaction picture to the Schrodinger picture. In this process, the rapidly oscillating terms $e^{-i(\omega_a-\omega_a')t}$ are absorbed into the time dependence of the density matrix and are no longer explicitly visible. When the frequency difference $|\omega_a-\omega_a'|^{-1}$ is large compared to the system' s relaxation rate, these terms average out and can be neglected. This leads to the secular approximation, where only the $\omega_a=\omega_a'$ terms are retained. Applying this approximation, Eq. (1.4.28) simplifies to:

$$\frac{d\rho_S^{(S)}(t)}{dt} = -\frac{i}{\hbar}\left[H_S+H_L,\rho_S^{(S)}(t)\right]+\mathcal{D}\left(\rho_S^{(S)}(t)\right), \tag{1.4.31}$$

where

$$H_L = \sum_{\alpha,\beta}\sum_{\omega_a}\Delta_{\alpha\beta}(\omega_a)S^{(S)\dagger}_{\alpha,\omega_a}S^{(S)}_{\beta,\omega_a} \tag{1.4.32}$$

is the Lamb shift Hamiltonian, which describes the energy level shifts of the system and

$$\mathcal{D}\left(\rho_S^{(S)}(t)\right) = \sum_{\alpha,\beta}\sum_{\omega_a}\Gamma_{\alpha\beta}(\omega_a)\left[S^{(S)}_{\beta,\omega_a}\rho_S^{(S)}(t)S^{(S)\dagger}_{\alpha,\omega_a}-\frac{1}{2}\left\{S^{(S)\dagger}_{\alpha,\omega_a}S^{(S)}_{\beta,\omega_a},\rho_S^{(S)}(t)\right\}\right], \tag{1.4.33}$$

doi:10.6342/NTU202503909

is the dissipator, which captures dissipation and decoherence arising from the coupling to mode ω_a in channels α and β. Equation (1.4.31) is known as the Lindblad master equation.

1.5 Thesis Outline

This thesis is organized as follows. Chapter 2 introduces the Hamiltonian and derives the equation of motion, along with the emission spectrum obtained via input-output theory. Chapter 3 compares the theoretical predictions with experimental results, focusing on the coherent spectral features and their interpretation in terms of wave mixing process. Finally, Chapter 4 summarizes our main findings.

doi:10.6342/NTU202503909

Chapter 2

Waveguide Quantum Electrodynamics Framework

2.1 Hamiltonian and Master Equation

We consider a one-dimensional waveguide with one end terminated by a small capacitor, which acts as an anti-mode mirror at $x = 0$. An M-level transmon is positioned at this end of the waveguide ($x = 0$) and is coupled to it [2, 33, 68]. The transmon is driven by two microwave fields with carrier frequencies ω_{d1} and ω_{d2}, and corresponding Rabi frequencies Ω_1 and Ω_2, respectively, as illustrated in Fig. 2.1. The number of transmon levels M must be chosen sufficiently large to ensure that the population in the $(M + 1)$th level remains negligible under any applied drive strength. The Hamiltonian describing this system is given by

$$H_{tot}^{(S)}(t) = H_S^{(S)}(t) + H_B^{(S)} + H_I^{(S)}, \tag{2.1.1}$$

where the system Hamiltonian

$$H_S^{(S)}(t) = H_A^{(S)} + H_{MW1}^{(S)}(t) + H_{MW2}^{(S)}(t), \tag{2.1.2}$$

doi:10.6342/NTU202503909

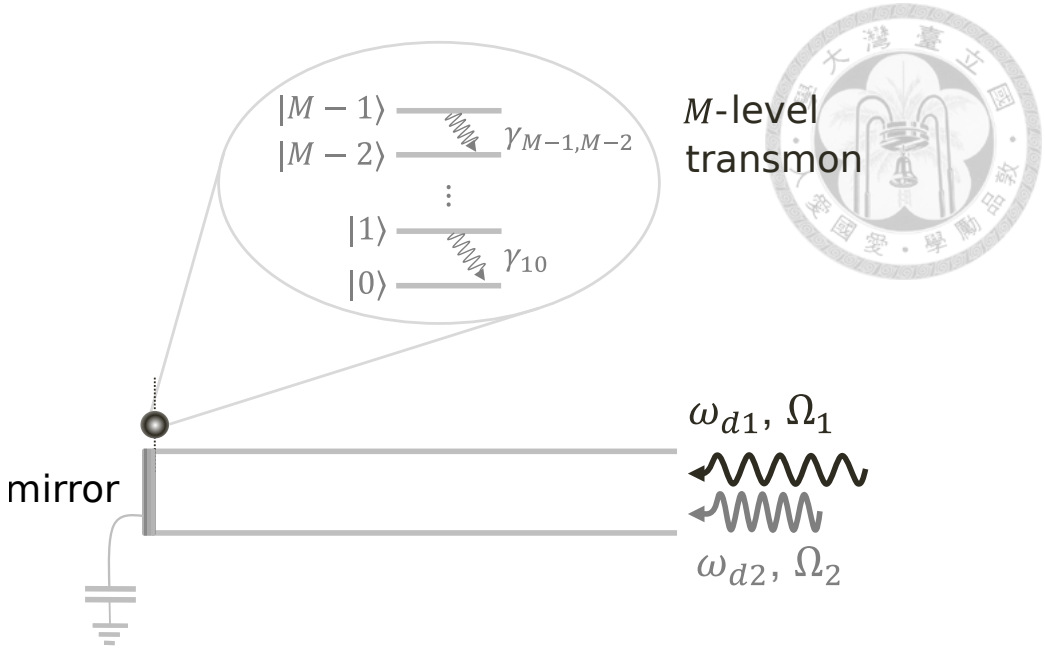

Figure 2.1: Schematic of the waveguide QED system studied in this work. An M-level transmon is coupled to the mirror end of a one-dimensional semi-infinite waveguide, where the mirror is formed by terminating the waveguide with a large capacitor. The transmon is driven by two external coherent fields with carrier frequencies ω_{d1} and ω_{d2}, and Rabi frequencies Ω_1 and Ω_2, respectively.

with

$$H_A^{(S)} = \sum_{m=0}^{M-1} \hbar\omega_m \sigma_{mm}, \tag{2.1.3}$$

describing the bare energy levels of the transmon. Here, $\sigma_{mm} = |m\rangle\langle m|$ is the atomic projection operator for $m = 0, 1, \ldots, M-1$. The two-tone driving fields are represented by

$$H_{MW1}^{(S)}(t) = \hbar \sum_{m=1}^{M-1} \frac{\sqrt{m}\Omega_1}{2} \left(\sigma_{m,m-1} e^{-i\omega_{d1}t} + h.c.\right), \tag{2.1.4}$$

$$H_{MW2}^{(S)}(t) = \hbar \sum_{m=1}^{M-1} \frac{\sqrt{m}\Omega_2}{2} \left(\sigma_{m,m-1} e^{-i\omega_{d2}t} + h.c.\right), \tag{2.1.5}$$

where $\sigma_{m,m-1} = \sigma_{m-1,m}^{\dagger} = |m\rangle\langle m-1|$ denotes the atomic ladder operator between the mth and $(m-1)$th levels. The energy of the waveguide modes is described by the

doi:10.6342/NTU202503909

Hamiltonian

$$H_B^{(S)} = \int_0^\infty d\omega \hbar\omega a_\omega^\dagger a_\omega, \tag{2.1.6}$$

where $a_\omega^\dagger$ and a_ω are the creation and annihilation operators for a waveguide photon of frequency ω, satisfying the commutation relation [69]:

$$[a_\omega, a_{\omega'}^\dagger] = \delta(\omega - \omega'). \tag{2.1.7}$$

The interaction between the transmon and the waveguide is discribed by

$$H_I^{(S)} = i\hbar \sum_{m=1}^{M-1} \int_0^\infty d\omega \sqrt{m} g(\omega) \left(\sigma_{m,m-1} a_\omega + \sigma_{m-1,m} a_\omega^\dagger\right), \tag{2.1.8}$$

where $\sqrt{m}g(\omega)$ is the coupling strength between the mth energy level of transmon and the waveguide mode at frequency ω [21].

To derive the master equation, we now follow the general formalism outlined in Sec. 1.4. By comparing Eq. (2.1.8) with Eq. (1.4.15), we identify the system and bath operators in our case as

$$S_1^{(S)} = \sum_{m=1}^{M-1} \sqrt{m}\sigma_{m-1,m}, \qquad S_2^{(S)} = \sum_{m=1}^{M-1} \sqrt{m}\sigma_{m,m-1}, \tag{2.1.9}$$

$$B_1^{(S)} = i\int_0^\infty d\omega\, g(\omega) a_\omega^\dagger, \qquad B_2^{(S)} = i\int_0^\infty d\omega\, g(\omega) a_\omega. \tag{2.1.10}$$

By substituting Eq. (2.1.10) into Eq. (1.4.25) and assuming the bath is initially in the vacuum state [47], we find that only the term with $\alpha = \beta = 1$ survives. Therefore, to obtain the master equation, it is sufficient to compute $\Gamma_{11}(\nu)$:

doi:10.6342/NTU202503909

$$F_{11}(\nu) = \int_0^\infty ds\, e^{i\nu s}\, \mathrm{Tr}_B\Big(B_1^{(I)\dagger}(s) B_1^{(I)}(0)\rho_B^{(I)}\Big) \\ = \int_0^\infty ds \int_0^\infty d\omega' \int_0^\infty d\omega'' g(\omega')g(\omega'')e^{i(\omega'-\nu)s}\langle 0|a_{\omega'}a^\dagger_{\omega''}|0\rangle. \tag{2.1.11}$$

Using the commutation relation given in Eq. (2.1.7), we have

$$F_{11}(\nu) = \int_0^\infty d\omega'\, g^2(\omega') \left[\pi\delta(\omega'-\nu) + i\mathrm{PV}\left(\frac{1}{\omega'-\nu}\right)\right]. \tag{2.1.12}$$

This leads us to

$$\Gamma_{11}(\nu) = \pi \int_0^\infty d\omega'\, g^2(\omega')\delta(\omega'-\nu) = \begin{cases} \pi g^2(\nu), & \text{if } \nu > 0, \\ 0, & \text{if } \nu < 0, \end{cases} \tag{2.1.13}$$

which shows that $\Gamma_{11}(\nu)$ is non-zero only for downward transitions (i.e. decay) and vanishes for upward ones. The factor $\Delta_{11}(\nu)$ is given by:

$$\Delta_{11}(\nu) = \mathrm{PV}\int_0^\infty d\omega' \frac{g^2(\omega')}{\omega'-\nu} \approx g^2(\nu)\,\mathrm{PV}\int_0^\infty \frac{1}{\omega'-\nu} d\omega' \approx 0. \tag{2.1.14}$$

It is noteworthy that, to obtain Eq. (2.1.14), we assume $g(\nu)$ is approximately constant over the relevant bandwidth [35]. Substituting Eqs. (2.1.2), (2.1.9), (2.1.13), and (2.1.14) into Eq. (1.4.28), the master equation is obtained [70]:

doi:10.6342/NTU202503909

$$
\begin{aligned}
\frac{d\rho}{dt} = & -i \sum_{m=0}^{M-1} \omega_m [\sigma_{mm}, \rho] \\
& + i \sum_{m=1}^{M-1} \frac{\sqrt{m}\Omega_1}{2} ([\sigma_{m,m-1} e^{-i\omega_{d1}t} + \sigma_{m-1,m} e^{i\omega_{d1}t}, \rho] \\
& + i \sum_{m=1}^{M-1} \frac{\sqrt{m}\Omega_2}{2} ([\sigma_{m,m-1} e^{-i\omega_{d2}t} + \sigma_{m-1,m} e^{i\omega_{d2}t}, \rho] \\
& + \sum_{m,n=1}^{M-1} \frac{\sqrt{mn}\gamma_{m,m-1}}{2} ([\sigma_{m-1,m}\rho, \sigma_{n,n-1}] + [\sigma_{n-1,n}, \rho\sigma_{m,m-1}]) \\
& + \sum_{m,n=1}^{M-1} \frac{mn\gamma^{\phi}}{2} ([\sigma_{mm}\rho, \sigma_{nn}] + [\sigma_{nn}, \rho\sigma_{mm}]) .
\end{aligned}
\tag{2.1.15}
$$

To simplify notation, we define $\gamma_{m,m-1} \equiv \Gamma_{11}(\omega_m - \omega_{m-1}) = 2\pi g^2(\omega_m - \omega_{m-1})$ as the decay rate for the $|m\rangle$ to $|m-1\rangle$ transition. The last term is included to account for the pure dephasing effect, with γ^{ϕ} denoting the pure dephasing rate associated with the energy levels $|0\rangle$ and $|1\rangle$ (see Appendix C.2 for details).

2.2 Emission Spectrum

The emission spectrum encodes how the driven transmon emits energy. By analyzing the spectrum, we can identify characteristic frequency components, quantify energy transfer processes, and distinguish between elastic and inelastic scattering between the photon and the transmon.

In this section, we derive the emission spectrum for our system. Sec. 2.2.1 introduces the input–output formalism [35], relating the output field to atomic operators, followed by the derivation of the general spectral expression in Sec. 2.2.2. The spectrum is then separated into coherent and incoherent components in Sec. 2.2.3. Finally, Sec. 2.2.4 provides an analytical example under monochromatic driving.

doi:10.6342/NTU202503909

2.2.1 Input-Output Formalism

We begin the discussion by considering the Heisenberg equation for the field operator $a_\omega(t)$:

$$\begin{aligned}\frac{da_\omega(t)}{dt} &= \frac{i}{\hbar}\left[H_{tot}^{(H)}, a_\omega(t)\right] \\ &= -i\omega a_\omega(t) - \sum_{m=0}^{M-1}\sqrt{m}g(\omega)\sigma_{m-1,m}(t).\end{aligned} \tag{2.2.1}$$

Integrating Eq. (2.2.1), the dynamics of the field operator is obtained

$$\tilde{a}_\omega(t_f) = \tilde{a}_\omega(t_i) - \int_{t_i}^{t_f} dt' \sum_{m=0}^{M-1}\sqrt{m}g(\omega)\tilde{\sigma}_{m-1,m}(t')e^{i(\omega-\omega_{m,m-1})t'}, \tag{2.2.2}$$

where $\tilde{a}_\omega(t) = a_\omega(t)e^{i\omega t}$ and $\tilde{\sigma}_{m-1,m}(t) = \sigma_{m-1,m}(t)e^{i\omega_{m,m-1}t}$ are the slowly varying field and atomic operators, respectively, and $\omega_{m,m-1} = \omega_m - \omega_{m-1}$ denotes the transition frequency between the mth and $(m-1)$th levels. Here, t_i and t_f denote the times at which the interaction between the transmon and the field begins and ends, respectively.

By summing over all frequency modes, the input–output relation can be obtained:

$$a_{out}(t) = a_{in}(t) - \sum_{m=0}^{M-1}\sqrt{m\gamma_{m,m-1}}\sigma_{m,m-1}(t), \tag{2.2.3}$$

where the input and output signals are given by

$$a_{in}(t) = \frac{1}{\sqrt{2\pi}}\int_0^\infty d\omega\, \tilde{a}_\omega(t_i)e^{-i\omega t}, \tag{2.2.4}$$

$$a_{out}(t) = \frac{1}{\sqrt{2\pi}}\int_0^\infty d\omega\, \tilde{a}_\omega(t_f)e^{-i\omega t}. \tag{2.2.5}$$

From this, the input–output relation, Eq. (2.2.3), shows that the output signal consists of the incoming wave and the response from the atom.

doi:10.6342/NTU202503909

2.2.2 Emission Spectrum Expression

With the input-output relation discussed in previous section, we now derive the expression for the scatter-field emission spectrum, defined as [71]:

$$S(\omega) = \frac{1}{2Z_0}\mathrm{Re}\left[\int_{-\infty}^{\infty} d\tau\, e^{-i\omega\tau} \lim_{t\to\infty} \left\langle V^{(\mathrm{sc})\dagger}(t+\tau)V^{(\mathrm{sc})}(t)\right\rangle\right], \tag{2.2.6}$$

where Z_0 is the characteristic impedance, and the scattered voltage operator is given by [2, 72]

$$V^{(\mathrm{sc})}(t) = -i\sqrt{\frac{\hbar Z_0}{4\pi}}\int_0^{\infty} d\omega\sqrt{\omega}\tilde{a}_{\omega}^{(\mathrm{sc})}(t)e^{-i\omega t}. \tag{2.2.7}$$

In this expression, the field operator $\tilde{a}_{\omega}^{(\mathrm{sc})}(t)$ is the slowly varying amplitude. By using Eq. (2.2.2), we can relate the scattered signal $\tilde{a}_{\omega}^{(\mathrm{sc})}(t)$ to atomic response through

$$\tilde{a}_{\omega}^{(\mathrm{sc})}(t) = -\int_0^t dt' \sum_{m=0}^{M-1}\sqrt{m}g(\omega)\tilde{\sigma}_{m-1,m}(t')e^{i(\omega-\omega_{m,m-1})t'}. \tag{2.2.8}$$

Substituting Eq. (2.2.8) into Eq. (2.2.7), we obtain

$$V^{(\mathrm{sc})}(t) = i\sqrt{\frac{\hbar Z_0}{4\pi}}\sum_{m=0}^{M-1}\sqrt{m}e^{i\omega_{m,m-1}t}\int_0^t dt'\tilde{\sigma}_{m-1,m}(t')\int_0^{\infty} d\omega\sqrt{\omega}g(\omega)e^{i(\omega-\omega_{m,m-1})(t'-t)}. \tag{2.2.9}$$

To evaluate the frequency integral, we assume that $\sqrt{\omega}g(\omega)$ varies slowly near $\omega_{m,m-1}$ [35], allowing it to be approximated as a constant. By changing variables $\omega' = \omega - \omega_{m,m-1}$ and extending the lower limit of integration to $-\infty$ (since $\omega_{m,m-1}$ is in the GHz range), we obtain:

doi:10.6342/NTU202503909

$$\int_0^\infty d\omega\, \sqrt{\omega} g(\omega) e^{i(\omega-\omega_{m,m-1})(t'-t)} \approx \sqrt{\omega_{m,m-1}} g(\omega_{m,m-1}) \cdot 2\pi\delta(t'-t). \quad (2.2.10)$$

Substituting Eq. (2.2.10) into Eq. (2.2.9) and perform the time integral yields the scattered voltage operator:

$$V^{(\mathrm{sc})}(t) = i\sqrt{\frac{\hbar Z_0}{2}} \sum_{m=0}^{M-1} \sqrt{m\gamma_{m,m-1}\omega_{m,m-1}}\sigma_{m-1,m}(t), \quad (2.2.11)$$

where $\sigma_{m-1,m}(t) = \tilde{\sigma}_{m-1,m}(t)e^{-i\omega_{m,m-1}t}$ and $\gamma_{m,m-1} = 2\pi g^2(\omega_m - \omega_{m-1})$. Substituting this expression into Eq. (2.2.6), we obtain

$$S(\omega) = \sum_{m,n=1}^{M-1} C_{mn} \mathrm{Re}\left[\int_0^\infty \lim_{t\to\infty} \langle \sigma_{m,m-1}(t+\tau)\, \sigma_{n-1,n}(t)\rangle\, e^{-i\omega\tau} d\tau\right], \quad (2.2.12)$$

with the coefficient

$$C_{mn} = \frac{\hbar}{4\pi}\sqrt{mn\gamma_{m,m-1}\gamma_{n,n-1}\omega_{m,m-1}\omega_{n,n-1}}. \quad (2.2.13)$$

2.2.3 Coherent and Incoherent Parts

To obtain the emission spectrum, Eq. (2.2.12), one needs to compute the steady-state two-time correlation function of the atomic operator. The fluctuation about the steady state of the atomic ladder operator is defined as

$$\delta\sigma_{m,m-1}(t) = \sigma_{m,m-1}(t) - \langle\sigma_{m,m-1}(t)\rangle_{ss}, \quad (2.2.14)$$

where $\langle\sigma_{m,m-1}(t)\rangle_{ss} = \lim_{t\to\infty}\langle\sigma_{m,m-1}(t)\rangle$ denotes the steady state of atmoic coherence. Substituting Eq. (2.2.14) into Eq. (2.2.12), the emission spectrum can be decomposed into

doi:10.6342/NTU202503909

two contributions: the coherent part

$$S_{co}(\omega) = \sum_{m,n=1}^{M-1} C_{mn} \mathrm{Re}\left[\int_0^\infty \lim_{t\to\infty} \langle \sigma_{m,m-1}(t+\tau)\rangle \langle \sigma_{n-1,n}(t)\rangle e^{-i\omega\tau} d\tau\right], \quad (2.2.15)$$

and the incoherent one

$$S_{inco}(\omega) = \sum_{m,n=1}^{M-1} C_{mn} \mathrm{Re}\left[\int_0^\infty \lim_{t\to\infty} \langle \delta\sigma_{m,m-1}(t+\tau)\, \delta\sigma_{n-1,n}(t)\rangle e^{-i\omega\tau} d\tau\right]. \quad (2.2.16)$$

2.2.4 Example: Monochromatic Driving (Mollow Triplet)

In this section, our objective is to apply the formalism developed in the previous section to illustrate the coherent and incoherent spectral behavior of a simple model: a single two-level atom is driven by a classical field with carrier frequency ω_d and Rabi frequency Ω_d [73, 74]. The dynamics of this system are governed by the master equation:

$$\frac{d\rho}{dt} = i\frac{\Delta}{2}[\sigma_z, \rho] + i\frac{\Omega_d}{2}\left([\sigma_{10} + \sigma_{01}, \rho]\right) + \frac{\gamma_{10}}{2}\left([\sigma_{01}\rho, \sigma_{10}] + [\sigma_{01}, \rho\sigma_{10}]\right), \quad (2.2.17)$$

where $\Delta = \omega_d - \omega_{10}$ is the field-to-atom detuning and $\sigma_z = \sigma_{11} - \sigma_{00}$ is the population inversion operator.

Sandwiching the master equation by atomic states, we obtain the optical Bloch equations:

$$\frac{d}{dt}\langle\sigma_{10}(t)\rangle = \left(-i\Delta - \frac{\gamma_{10}}{2}\right)\langle\sigma_{10}(t)\rangle + \frac{i\Omega_d}{2}\langle\sigma_z(t)\rangle, \quad (2.2.18)$$

$$\frac{d}{dt}\langle\sigma_{01}(t)\rangle = \left(i\Delta - \frac{\gamma_{10}}{2}\right)\langle\sigma_{01}(t)\rangle - \frac{i\Omega_d}{2}\langle\sigma_z(t)\rangle, \quad (2.2.19)$$

$$\frac{d}{dt}\langle\sigma_z(t)\rangle = i\Omega_d\Big(\langle\sigma_{10}(t)\rangle - \langle\sigma_{01}(t)\rangle\Big) - \gamma_{10}\Big(\langle\sigma_z(t)\rangle + \langle\sigma_{00}(t)\rangle + \langle\sigma_{11}(t)\rangle\Big), \quad (2.2.20)$$

doi:10.6342/NTU202503909

with the constraint $\langle\sigma_{00}(t)\rangle + \langle\sigma_{11}(t)\rangle = 1$. The steady-state solutions are given by:

$$\lim_{t\to\infty}\langle\sigma_{10}(t)\rangle = \frac{\Omega_d/2}{\Delta - i\gamma_{10}/2}\cdot\langle\sigma_z(t)\rangle, \tag{2.2.21}$$

$$\lim_{t\to\infty}\langle\sigma_{01}(t)\rangle = \Big(\lim_{t\to\infty}\langle\sigma_{10}(t)\rangle\Big)^*, \tag{2.2.22}$$

$$\lim_{t\to\infty}\langle\sigma_z\rangle = \frac{-2(\Delta^2 + (\gamma_{10}/2)^2)}{2(\Delta^2 + (\gamma_{10}/2)^2) + \Omega_d^2}. \tag{2.2.23}$$

By applying the quantum regression theorem (see Appendix D for a detailed discussion), the dynamics of the two-time correlation functions are determined through the same equations that govern the evolution of the single-time expectation values:

$$\frac{d}{d\tau}\langle\sigma_{10}(\tau)\sigma_{01}\rangle_{ss} = \Big(-i\Delta - \frac{\gamma_{10}}{2}\Big)\langle\sigma_{10}(\tau)\sigma_{01}\rangle_{ss} + \frac{i\Omega_d}{2}\langle\sigma_z(\tau)\sigma_{01}\rangle_{ss}, \tag{2.2.24}$$

$$\frac{d}{d\tau}\langle\sigma_{10}(\tau)\sigma_{01}\rangle_{ss} = \Big(i\Delta - \frac{\gamma_{10}}{2}\Big)\langle\sigma_{01}(\tau)\sigma_{01}\rangle_{ss} - \frac{i\Omega_d}{2}\langle\sigma_z(\tau)\sigma_{01}\rangle_{ss}, \tag{2.2.25}$$

$$\frac{d}{d\tau}\langle\sigma_z(\tau)\sigma_{01}\rangle_{ss} = i\Omega_d\Big(\langle\sigma_{10}(\tau)\sigma_{01}\rangle_{ss} - \langle\sigma_{01}(\tau)\sigma_{01}\rangle_{ss}\Big) \tag{2.2.26}$$

$$- \gamma_{10}\Big(\langle\sigma_z(\tau)\sigma_{01}\rangle_{ss} + \langle\sigma_{00}(\tau)\sigma_{01}\rangle_{ss} + \langle\sigma_{11}(\tau)\sigma_{01}\rangle_{ss}\Big), \tag{2.2.27}$$

where $\langle A(\tau)B\rangle_{ss} \equiv \lim_{t\to\infty}\langle A(t+\tau)B(t)\rangle$ with the initial condition:

$$\langle\sigma_+(0)\sigma_-\rangle_{ss} = \lim_{t\to\infty}\langle\sigma_+(t)\sigma_-(t)\rangle = \frac{1}{2}\Big(\lim_{t\to\infty}\langle\sigma_z(t)\rangle + 1\Big), \tag{2.2.28}$$

$$\langle\sigma_-(0)\sigma_-\rangle_{ss} = \lim_{t\to\infty}\langle\sigma_-(t)\sigma_-(t)\rangle = 0, \tag{2.2.29}$$

$$\langle\sigma_z(0)\sigma_-\rangle_{ss} = \lim_{t\to\infty}\langle\sigma_z(t)\sigma_-(t)\rangle = \lim_{t\to\infty}\langle\sigma_-(t)\rangle. \tag{2.2.30}$$

By solving Eqs. (2.2.24) to (2.2.26), we obtain, in the resonant case where $\Delta = 0$ [74]:

doi:10.6342/NTU202503909

$$\langle\sigma_+(\tau)\sigma_-\rangle_{ss} = \frac{\Omega_d^2}{\gamma_{10}^2+2\Omega_d^2}\Bigg[\frac{\gamma_{10}^2}{\gamma_{10}^2+2\Omega_d^2}e^{i\omega_{10}\tau} + \frac{1}{2}e^{-(\gamma_{10}/2-i\omega_{10})\tau}$$
$$-\frac{1}{2}\left(\frac{\gamma_{10}^2}{\gamma_{10}^2+2\Omega_d^2}\cdot\frac{3\gamma_{10}/4+\kappa}{\kappa}-\frac{\gamma_{10}/2}{\kappa}-\frac{\gamma_{10}/4+\kappa}{2\kappa}\right)\exp\left\{-\left(\frac{3\gamma_{10}}{4}-\kappa-i\omega_{10}\right)\tau\right\}$$
$$+\frac{1}{2}\left(\frac{\gamma_{10}^2}{\gamma_{10}^2+2\Omega_d^2}\cdot\frac{3\gamma_{10}/4-\kappa}{\kappa}-\frac{\gamma_{10}/2}{\kappa}-\frac{\gamma_{10}/4-\kappa}{2\kappa}\right)\exp\left\{-\left(\frac{3\gamma_{10}}{4}+\kappa-i\omega_{10}\right)\tau\right\}\Bigg], \tag{2.2.31}$$

where

$$\kappa = \sqrt{\left(\frac{\gamma_{10}}{4}\right)^2-\Omega_d^2}. \tag{2.2.32}$$

Substituting Eq. (2.2.31) into Eq. (2.2.12), we get

$$S(\omega) = S_{co}(\omega) + S_{inco}(\omega), \tag{2.2.33}$$

where

$$S_{co}(\omega) \propto 2\pi\cdot\frac{\Omega_d^2}{\gamma_{10}^2+2\Omega_d^2}\delta(\omega-\omega_{10}), \tag{2.2.34}$$
$$S_{inco}(\omega) \propto \frac{1}{2}\cdot\frac{\gamma_{10}/2}{\gamma_{10}^2/4+(\omega-\omega_{10})^2} + \frac{1}{4}\cdot\frac{3\gamma_{10}/4}{(3\gamma_{10}/4)^2+[(\omega-\omega_{10})-\Omega_d]^2} + \frac{1}{4}\cdot\frac{3\gamma_{10}/4}{(3\gamma_{10}/4)^2+[(\omega-\omega_{10})+\Omega_d]^2}. \tag{2.2.35}$$

As we can see, the coherent spectrum shows a sharp delta-function peak at the atomic transition frequency $\omega = \omega_{10}$, reflecting the phase-coherent component of the emission due to the continuous driving.

In contrast, the incoherent spectrum exhibits a broader structure with three peaks located at $\omega = \omega_{10}$ and $\omega = \omega_{10} \pm \Omega_d$, known as the Mollow triplet, as shown in Fig. 2.2. These broadened features arise from quantum fluctuations and spontaneous emission processes.

doi:10.6342/NTU202503909

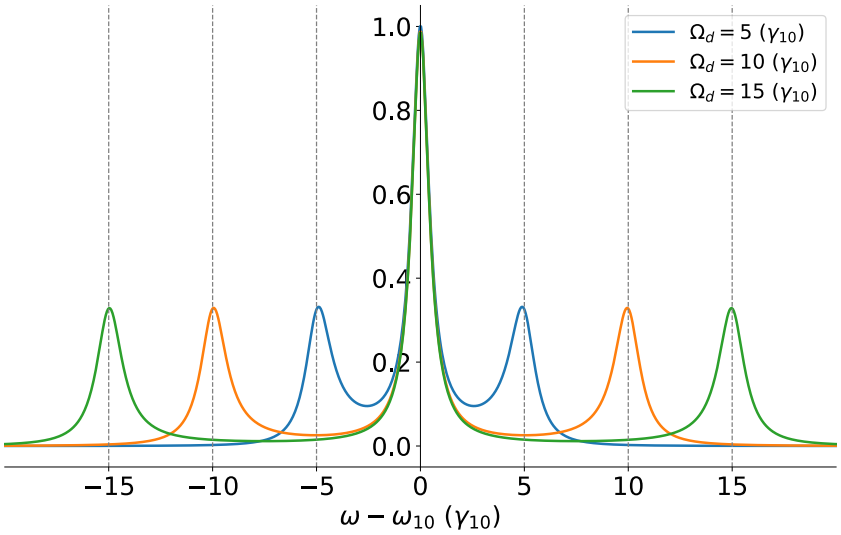

Figure 2.2: Incoherent emission spectra $S_{\text{inco}}(\omega)$ showing the Mollow triplet under different driving strengths $\Omega_d = 5, 10, 15$ (in units of γ_{10}). The three Lorentzian peaks appear around $\omega = \omega_{10}$ and $\omega = \omega_{10} \pm \Omega_d$. As Ω_d increases, the sidebands shift further apart and become more pronounced.

2.3 Bichromatic Driving: Floquet Analysis

In the previous section, we discussed the coherent and incoherent fluorescence spectra under a single-tone driving scenario. We now turn to a more general case in which a single multiple level atom is simultaneously excited by two driving fields. In such a situation, it is not possible to find an appropriate rotating frame that eliminates both carrier frequencies. As a result, the system' s dynamics become periodic in the long-time limit, and the formalism developed in the previous sections is no longer applicable. In this section, we introduce Floquet analysis to handle this type of periodic problem in the computation of emission spectra [75].

2.3.1 Periodic Steady States under Bichromatic Drivings

We begin the discussion by considering the master equation in a rotating frame with frequency $\omega_s = \frac{1}{2}(\omega_{d1} + \omega_{d2})$:

doi:10.6342/NTU202503909

$$
\begin{aligned}
\frac{d\tilde{\rho}(t)}{dt} &= i\sum_{m=0}^{M-1}\left(m\omega_s-\omega_m\right)\left[\sigma_{mm},\tilde{\rho}(t)\right] \\
&+ i\sum_{m=1}^{M-1}\frac{\sqrt{m}\Omega_{d1}}{2}[\sigma_{m,m-1}e^{i\delta t}+\sigma_{m-1,m}e^{-i\delta t},\tilde{\rho}(t)] \\
&+ i\sum_{m=1}^{M-1}\frac{\sqrt{m}\Omega_{d2}}{2}[\sigma_{m,m-1}e^{-i\delta t}+\sigma_{m-1,m}e^{i\delta t},\tilde{\rho}(t)] \\
&+ \sum_{m,n=1}^{M-1}\frac{\sqrt{mn}\gamma_{m,m-1}}{2}\left([\sigma_{m-1,m}\tilde{\rho}(t),\sigma_{n,n-1}]+[\sigma_{n-1,n},\tilde{\rho}(t)\sigma_{m,m-1}]\right) \\
&+ \sum_{m,n=1}^{M-1}\frac{mn\gamma^{\phi}}{2}\left([\sigma_{mm}\tilde{\rho}(t),\sigma_{nn}]+[\sigma_{nn},\tilde{\rho}(t)\sigma_{mm}]\right),
\end{aligned}
\tag{2.3.1}
$$

where $\delta=\frac{1}{2}\left(\omega_{d2}-\omega_{d1}\right)$ represents the frequency difference between two driving fields. It is noteworthy that this frequency is incorporated into the master equation, Eq. (2.3.1), making the solution inherently periodic with a period $2\pi/\delta$. To address this periodicity, we express the density matrix using a Fourier series representation

$$
\tilde{\rho}(t)=\sum_{l=-\infty}^{\infty}\tilde{\rho}^{(l)}(t)e^{il\delta t},
\tag{2.3.2}
$$

where $\tilde{\rho}^{(l)}(t)$ represents the lth Fourier coefficient. Substituting Eq. (2.3.2) into Eq. (2.3.1) and collecting terms, we get the following coupled differential equations:

doi:10.6342/NTU202503909

$$
\begin{aligned}
\frac{d\tilde{\rho}^{(l)}(t)}{dt} &= -il\delta\tilde{\rho}^{(l)}(t) + i\sum_{m=0}^{M-1}(m\omega_s - \omega_m)\left[\sigma_{mm}, \tilde{\rho}^{(l)}(t)\right] \\
&+ i\sum_{m=1}^{M-1}\frac{\sqrt{m}\Omega_{d1}}{2}\left(\left[\sigma_{m,m-1}, \tilde{\rho}^{(l-1)}(t)\right] + \left[\sigma_{m-1,m}, \tilde{\rho}^{(l+1)}(t)\right]\right) \\
&+ i\sum_{m=1}^{M-1}\frac{\sqrt{m}\Omega_{d2}}{2}\left(\left[\sigma_{m,m-1}, \tilde{\rho}^{(l+1)}(t)\right] + \left[\sigma_{m-1,m}, \tilde{\rho}^{(l-1)}(t)\right]\right) \\
&+ \sum_{m,n=1}^{M-1}\frac{\sqrt{mn}\gamma_{m,m-1}}{2}\left(\left[\sigma_{m-1,m}\tilde{\rho}^{(l)}(t), \sigma_{n,n-1}\right] + \left[\sigma_{n-1,n}, \tilde{\rho}^{(l)}(t)\sigma_{m,m-1}\right]\right) \\
&+ \sum_{m,n=1}^{M-1}\frac{mn\gamma^{\phi}}{2}\left(\left[\sigma_{mm}\tilde{\rho}^{(l)}(t), \sigma_{nn}\right] + \left[\sigma_{nn}, \tilde{\rho}^{(l)}(t)\sigma_{mm}\right]\right).
\end{aligned}
\tag{2.3.3}
$$

By vectorizing the density matrix, Eq. (2.3.3), (see Appendix E for details), we define

$$
\mathbf{X}^{(l)}(t) = \begin{bmatrix} X_{00}^{(l)}(t) \\ X_{10}^{(l)}(t) \\ \vdots \\ X_{M-1,0(t)}^{(l)} \\ X_{01}^{(l)}(t) \\ \vdots \\ X_{M-1,M-1}^{(l)}(t) \end{bmatrix} = \begin{bmatrix} \tilde{\rho}_{00}^{(l)}(t) \\ \tilde{\rho}_{10}^{(l)}(t) \\ \vdots \\ \tilde{\rho}_{M-1,0}^{(l)}(t) \\ \tilde{\rho}_{01}^{(l)}(t) \\ \vdots \\ \tilde{\rho}_{M-1,M-1}^{(l)}(t) \end{bmatrix}, \tag{2.3.4}
$$

where $\mathbf{X}^{(l)}(t)$ is an $M^2 \times 1$ column vector. Using this representation, we obtain the following recurrence relation:

$$
\dot{\mathbf{X}}^{(l)}(t) = A\mathbf{X}^{(l-1)}(t) + B^{(l)}\mathbf{X}^{(l)}(t) + C\mathbf{X}^{(l+1)}(t), \tag{2.3.5}
$$

where

doi:10.6342/NTU202503909

$$A = i\sum_{m=1}^{M-1}\frac{\sqrt{m}}{2}\Big[\Omega_{d1}\left(\mathbb{I}_M\otimes\sigma_{m,m-1}-\sigma_{m,m-1}^T\otimes\mathbb{I}_M\right) + \Omega_{d2}\left(\mathbb{I}_M\otimes\sigma_{m-1,m}-\sigma_{m-1,m}^T\otimes\mathbb{I}_M\right)\Big], \tag{2.3.6}$$

$$C = i\sum_{m=1}^{M-1}\frac{\sqrt{m}}{2}\Big[\Omega_{d1}\left(\mathbb{I}_M\otimes\sigma_{m-1,m}-\sigma_{m-1,m}^T\otimes\mathbb{I}_M\right) + \Omega_{d2}\left(\mathbb{I}_M\otimes\sigma_{m,m-1}-\sigma_{m,m-1}^T\otimes\mathbb{I}_M\right)\Big], \tag{2.3.7}$$

and

$$\begin{aligned} B^{(l)} = & -il\delta\mathbb{I}_{M^2} \\ & + \sum_{m,n=0}^{M-1}\Bigg\{ i\left(m\omega_s-\omega_m\right)\left(\mathbb{I}_M\otimes\sigma_{mm}\right) - i\left(n\omega_s-\omega_n\right)\left(\sigma_{nn}\otimes\mathbb{I}_M\right) \\ & + \frac{\sqrt{mn}\gamma_{m,m-1}}{2}\Big[\left(\sigma_{n,n-1}^T\otimes\sigma_{m,m-1}\right) - \left(\mathbb{I}_M\otimes\sigma_{n,n-1}\sigma_{m-1,m}\right) \\ & + \left(\sigma_{m,m-1}^T\otimes\sigma_{n,n-1}\right) - \left(\left(\sigma_{m,m-1}\sigma_{n-1,n}\right)^T\otimes\mathbb{I}_M\right)\Big] \\ & + \frac{mn\gamma^{\phi}}{2}\Big[\left(\sigma_{nn}^T\otimes\sigma_{mm}\right) - \left(\mathbb{I}_M\otimes\sigma_{nn}\sigma_{mm}\right) \\ & + \left(\sigma_{mm}^T\otimes\sigma_{nn}\right) - \left(\left(\sigma_{mm}\sigma_{nn}\right)^T\otimes\mathbb{I}_M\right)\Big]\Bigg\}. \end{aligned} \tag{2.3.8}$$

are $M^2\times M^2$ matrices. In a realistic situation, it is not necessary to perform the infinite summation in Eq. (2.3.2); instead, the series converges for sufficiently large values of l. We therefore truncate the series by setting $l = L$. To solve for the Fourier coefficients, we re-express Eq. (2.3.3) as

$$\dot{\mathbf{X}}(t) = M\mathbf{X}(t), \tag{2.3.9}$$

doi:10.6342/NTU202503909

where $\mathbf{X}(t)$ is a column vector of dimension $(2L+1)M^2 \times 1$, containing the Fourier coefficients for each order l, and M is a block matrix defined as

$$M = \begin{bmatrix} B^{(-L)} & C & 0 & 0 & 0 & 0 & 0 \\ \vdots & \ddots & \vdots & \vdots & \vdots & \vdots & \vdots \\ 0 & A & B^{(-1)} & C & 0 & 0 & 0 \\ 0 & 0 & A & B^{(0)} & C & 0 & 0 \\ 0 & 0 & 0 & A & B^{(1)} & C & 0 \\ \vdots & \vdots & \vdots & \vdots & \vdots & \ddots & \vdots \\ 0 & 0 & 0 & 0 & 0 & A & B^{(L)} \end{bmatrix}. \tag{2.3.10}$$

In this expression, the matirx $B^{(l)}$ describes the self-evolution of the lth Fourier component, while matrices A and C represent the coupling between different orders l. With this compact equation, Eq. (2.3.9), the dynamics of each Fourier component can be easily obtained using the formal solution:

$$\mathbf{X}(t) = e^{Mt}\mathbf{X}(0). \tag{2.3.11}$$

2.3.2 Coherent Spectrum and Sideband Structure

We now turn to examine the emission spectra under the two-tone driving scenario. First, we transform the emission spectrum of the coherent part described by Eq. (2.2.15) into a rotating frame with frequency ω_s, yielding

$$S_{co}(\omega) = \sum_{m,n=1}^{M-1} C_{mn} \mathrm{Re}\left[\int_0^\infty \lim_{t\to\infty} \langle \tilde{\sigma}_{m,m-1}(t+\tau)\rangle \langle \tilde{\sigma}_{n-1,n}(t)\rangle \, e^{-i(\omega-\omega_s)\tau} \, d\tau\right]. \tag{2.3.12}$$

Here, $\tilde{\sigma}_{mn}(t) = e^{-i(m-n)\omega_s t}\sigma_{mn}$. Substituting Eq. (2.3.2) into Eq. (2.3.12) and truncating the series by setting $l = L$, we obtain

doi:10.6342/NTU202503909

$$S_{co}(\omega) = \sum_{m,n=1}^{M-1} C_{mn} \mathrm{Re}\Big[\int_0^{\infty} \left(\sum_{p=-L}^{L} \langle \tilde{\sigma}_{m,m-1} \rangle_{ss}^{(p)} e^{ip\delta(t+\tau)} \right) \cdot \left(\sum_{q=-L}^{L} \langle \tilde{\sigma}_{n-1,n} \rangle_{ss}^{(q)} e^{iq\delta t} \right) e^{-i(\omega-\omega_s)\tau} \, d\tau \Big]. \tag{2.3.13}$$

To address the time-oscillating terms in Eq. (2.3.13), we compute the time-averaged spectrum and find that it remains nonzero only under the condition $p + q = 0$. As a consequence, the coherent spectrum reduces to

$$\bar{S}_{co}(\omega) = \sum_{m,n=1}^{M-1} C_{mn} \mathrm{Re} \left[\sum_{p=-L}^{L} \langle \tilde{\sigma}_{m,m-1} \rangle_{ss}^{(p)} \langle \tilde{\sigma}_{n-1,n} \rangle_{ss}^{(-p)} \int_0^{\infty} e^{-i(\omega-\omega_s-p\delta)\tau} d\tau \right]. \tag{2.3.14}$$

By integrating Eq. (2.3.14), the time-averaged coherent spectrum becomes

$$\bar{S}_{co}(\omega) = \sum_{m,n=1}^{M-1} C_{mn} \sum_{p=-L}^{L} \mathrm{Re} \left[\langle \tilde{\sigma}_{m,m-1} \rangle_{ss}^{(p)} \langle \tilde{\sigma}_{n-1,n} \rangle_{ss}^{(-p)} \right] \pi \delta \left(\omega - \omega_s - p\delta \right). \tag{2.3.15}$$

Since the delta function $\delta(\omega - \omega_s - p\delta)$ represents an idealized spectrum with zero width, which cannot be resolved in real experiments due to finite spectral resolution, we approximate the delta function with a Lorentzian profile. This leads to the expression for the time-averaged coherent spectrum as

$$\bar{S}_{co}(\omega) = \sum_{m,n=1}^{M-1} C_{mn} \sum_{p=-L}^{L} \mathrm{Re} \left[\langle \tilde{\sigma}_{m,m-1} \rangle_{ss}^{(p)} \langle \tilde{\sigma}_{n-1,n} \rangle_{ss}^{(-p)} \right] \frac{\epsilon_l}{\left(\omega - (\omega_s + p\delta) \right)^2 + \epsilon_l^2}. \tag{2.3.16}$$

2.3.3 Incoherent Spectrum via Laplace Transform Method

In this section, we analyze the emission spectrum of the incoherent part using a similar computational approach to that discussed in the previous section. The incoherent spectrum in the rotating frame of frequency ω_s is given by

doi:10.6342/NTU202503909

$$S_{inco}(\omega) = \sum_{m,n=1}^{M-1} C_{mn} \mathrm{Re}\left[\int_0^\infty \lim_{t\to\infty} \langle \delta\tilde{\sigma}_{m,m-1}(t+\tau)\, \delta\tilde{\sigma}_{n-1,n}(t)\rangle\, e^{-i(\omega-\omega_s)\tau} d\tau\right]. \tag{2.3.17}$$

with

$$\begin{aligned} &\lim_{t\to\infty} \langle \delta\tilde{\sigma}_{m,m-1}(t+\tau)\, \delta\tilde{\sigma}_{n-1,n}(t)\rangle \\ &= \lim_{t\to\infty} \left[\langle \tilde{\sigma}_{m,m-1}(t+\tau)\, \tilde{\sigma}_{n-1,n}(t)\rangle - \langle \tilde{\sigma}_{m,m-1}(t+\tau)\rangle \langle \tilde{\sigma}_{n-1,n}(t)\rangle\right]. \end{aligned} \tag{2.3.18}$$

Here, the first term on the right-hand side is a standard two-time correlation function for atomic operators, which can be evaluated using the quantum regression theorem:

$$\lim_{t\to\infty} \langle \tilde{\sigma}_{m,m-1}(t+\tau)\, \tilde{\sigma}_{n-1,n}(t)\rangle = \mathrm{Tr}\left[\tilde{\sigma}_{m,m-1}\, \tilde{\Lambda}_n(\tau)\right], \tag{2.3.19}$$

where $\tilde{\Lambda}_n(\tau)$ is the time-evolved auxiliary operator associated with the initial condition $\tilde{\Lambda}_n(0) = \sigma_{n-1,n}\tilde{\rho}_{ss}$. The second term is the product of single-time expectation values in the long-time limit

$$\lim_{t\to\infty} \langle \tilde{\sigma}_{m,m-1}(t+\tau)\rangle \langle \tilde{\sigma}_{n-1,n}(t)\rangle = \lim_{t\to\infty} \left[\mathrm{Tr}\left[\sigma_{m,m-1}\, \tilde{\rho}(t+\tau)\right] \cdot \langle \tilde{\sigma}_{n-1,n}(t)\rangle\right]. \tag{2.3.20}$$

Using Eq. (2.3.19) and Eq. (2.3.20), we now define an auxiliary density matrix to isolate the incoherent part of the correlation:

$$\tilde{\Xi}_n(\tau) = \tilde{\Lambda}_n(\tau) - \lim_{t\to\infty} \tilde{\rho}(t+\tau) \langle \tilde{\sigma}_{n-1,n}(t)\rangle. \tag{2.3.21}$$

Owing to the periodicity of the steady-state solution discussed in Sec. 2.3.1, we express this auxiliary density matrix $\tilde{\Xi}_n(\tau)$ as a Fourier series: $\tilde{\Xi}_n(\tau) = \sum_l \tilde{\Xi}_n^{(l)}(\tau) e^{il\delta\tau}$. Substituting

doi:10.6342/NTU202503909

this into the Eq. (2.3.1) and applying a Laplace transform gives the following expression:

$$\begin{aligned}
\tilde{\Xi}_n^{(l)}(0) = (s + il\delta)\,\tilde{\Xi}_n^{(l)}(s) &- i\sum_{m=0}^{M-1}(m\omega_s - \omega_m)\left[\sigma_{mm}, \tilde{\Xi}_n^{(l)}(s)\right] \\
&- i\sum_{m=1}^{M-1}\frac{\sqrt{m}\Omega_{d1}}{2}\left(\left[\sigma_{m,m-1}, \tilde{\Xi}_n^{(l-1)}(s)\right] + \left[\sigma_{m-1,m}, \tilde{\Xi}_n^{(l+1)}(s)\right]\right) \\
&- i\sum_{m=1}^{M-1}\frac{\sqrt{m}\Omega_{d2}}{2}\left(\left[\sigma_{m,m-1}, \tilde{\Xi}_n^{(l+1)}(s)\right] + \left[\sigma_{m-1,m}, \tilde{\Xi}_n^{(l-1)}(s)\right]\right) \\
&- \sum_{m,m'=1}^{M-1}\frac{\sqrt{mm'}\gamma_{m,m-1}}{2}\left(\left[\sigma_{m-1,m}\tilde{\Xi}_n^{(l)}(s), \sigma_{m',m'-1}\right] + \left[\sigma_{m'-1,m'}, \tilde{\Xi}_n^{(l)}(s)\sigma_{m,m-1}\right]\right) \\
&- \sum_{m,m'=1}^{M-1}\frac{mm'\gamma^{\phi}}{2}\left(\left[\sigma_{mm}\tilde{\Xi}_n^{(l)}(s), \sigma_{m'm'}\right] + \left[\sigma_{m'm'}, \tilde{\Xi}_n^{(l)}(s)\sigma_{mm}\right]\right).
\end{aligned} \tag{2.3.22}$$

By vectorizing the auxiliary density matrix in Eq. (2.3.22), we obtain:

$$\mathbf{Y}_n(\tau = 0) = \tilde{M}(s)\mathbf{Y}_n(s), \tag{2.3.23}$$

where $\mathbf{Y}_n(s)$ is a column vector of dimension $(2L+1)M^2 \times 1$, composed of the Fourier components $\tilde{\Xi}_n^{(l)}(s)$, and $\tilde{M}(s)$ is a block matrix defined as

$$\tilde{M}(s) = \begin{bmatrix}
D^{(-L)}(s) & -C & 0 & 0 & 0 & 0 & 0 \\
\vdots & \ddots & \vdots & \vdots & \vdots & \vdots & \vdots \\
0 & -A & D^{(-1)}(s) & -C & 0 & 0 & 0 \\
0 & 0 & -A & D^{(0)}(s) & -C & 0 & 0 \\
0 & 0 & 0 & -A & D^{(1)}(s) & -C & 0 \\
\vdots & \vdots & \vdots & \vdots & \vdots & \ddots & \vdots \\
0 & 0 & 0 & 0 & 0 & -A & D^{(L)}(s)
\end{bmatrix}, \tag{2.3.24}$$

with

doi:10.6342/NTU202503909

$$
\begin{aligned}
D^{(l)}(s) = {} & (s + il\delta)\,\mathbb{I}_{M^2} \\
& - \sum_{m,m'=0}^{M-1} \Bigg\{ i\left(m\omega_s - \omega_m\right)\left(\mathbb{I}_M \otimes \sigma_{mm}\right) - i\left(n\omega_s - \omega_{m'}\right)\left(\sigma_{m'm'} \otimes \mathbb{I}_M\right) \\
& + \frac{\sqrt{mm'}\gamma_{m,m-1}}{2}\Big[\left(\sigma^T_{m',m'-1} \otimes \sigma_{m,m-1}\right) - \left(\mathbb{I}_M \otimes \sigma_{m',m'-1}\sigma_{m-1,m}\right) \\
& + \left(\sigma^T_{m,m-1} \otimes \sigma_{m',m'-1}\right) - \left(\left(\sigma_{m,m-1}\sigma_{m'-1,m'}\right)^T \otimes \mathbb{I}_M\right) \Big] \\
& + \frac{mm'\gamma^{\phi}}{2}\Big[\left(\sigma^T_{m'm'} \otimes \sigma_{mm}\right) - \left(\mathbb{I}_M \otimes \sigma_{m'm'}\sigma_{mm}\right) \\
& + \left(\sigma^T_{mm} \otimes \sigma_{m'm'}\right) - \left(\left(\sigma_{mm}\sigma_{m'm'}\right)^T \otimes \mathbb{I}_M\right) \Big] \Bigg\}.
\end{aligned}
\tag{2.3.25}
$$

By solving Eq. (2.3.23) and substituting $s = -i\left(\omega - \omega_s\right)$ [75], the incoherent spectrum can be obtained as:

$$
S_{inco}(\omega) = \sum_{m,n=1}^{M-1} C_{mn}\mathrm{Re}\left[Y^{(0)}_{n;m-1,m}\left(-i\left(\omega - \omega_s\right)\right)\right], \tag{2.3.26}
$$

where $Y^{(0)}_{n;m-1,m}(s)$ denotes the $(m-1,m)$ element of $\tilde{\Xi}^{(0)}_n(s)$.

doi:10.6342/NTU202503909

Chapter 3

Experimental Comparison and Interpretation

In the previous chapter, we developed a formalism that goes beyond the conventional two- or three-level approximation to compute both coherent and incoherent emission spectra under strong two-tone driving. In this chapter, we investigate the effects of higher transmon levels on the wave-mixing process in realistic conditions by comparing the spectra predicted by our method with experimental results. Additionally, we analyze the frequencies generated in single-atom wave mixing using the Dyson series formalism introduced in Sec. 1.3.2.

It is important to note that all the experiments discussed in this chapter were conducted by Mr. Fahad Aziz in Professor Io-Chun Hoi's group at National Tsing Hua University.

3.1 Characterizing the Transmon Used in Experiment

To obtain the spectral results presented in the following sections, it is necessary to first characterize the fundamental parameters of the transmon. Experimentally, this is achieved by sending a weak probe field—with carrier and Rabi frequencies denoted by ω_{d2} and Ω_2, respectively—to interact with a transmon that is simultaneously driven by a pump field characterized by carrier frequency ω_{d1} and Rabi frequency Ω_1. The response of the transmon is analyzed via the reflection of the probe field, and the reflection coefficient is

doi:10.6342/NTU202503909

defined as $r = \left|\frac{\langle a_{\text{out}}(t)\rangle}{\langle a_{\text{in}}(t)\rangle}\right|$. By substituting the output field a_{out} using Eq. (2.2.3) and assuming the input is a classical single-mode probe field, the input expectation value becomes [29, 76]

$$\langle a_{\text{in}}(t)\rangle \to \frac{i\Omega_2}{2\sqrt{(\omega_{d2}/\omega_{10})\,\gamma_{10}}} e^{-i\omega_{d2}t}, \tag{3.1.1}$$

from which we obtain the reflection coefficient:

$$r = \left|1 + \sum_m \frac{2i\sqrt{m(\omega_{d2}/\omega_{10})\gamma_{m,m-1}\gamma_{10}}}{\Omega_2}\langle\sigma_{m-1,m}(t)\rangle e^{i\omega_{d2}t}\right|. \tag{3.1.2}$$

In this setup, the probe field is chosen to be sufficiently weak, i.e, $\Omega_2/\gamma_{10} \ll 1$, such that the density matrix of the driven transmon can be expanded perturbatively as

$$\tilde{\rho}(t) \approx \tilde{\rho}^{(0)}(t) + \frac{\Omega_2}{\gamma_{10}}\,\tilde{\rho}^{(1)}(t)\,e^{-i(\omega_{d2}-\omega_{d1})t}, \tag{3.1.3}$$

where $\tilde{\rho}^{(0)}(t)$ represents the zeroth-order density matrix in the absence of the probe field, and $\tilde{\rho}^{(1)}(t)$ accounts for the first-order response due to the probe. Substituting this expansion into the master equation, Eq. (2.1.15), we have

$$\begin{aligned}
\frac{d\tilde{\rho}^{(0)}}{dt} &= i\sum_{m=0}^{M-1}(m\omega_{d1}-\omega_m)\left[\sigma_{mm},\tilde{\rho}^{(0)}\right] \\
&+ i\sum_{m=1}^{M-1}\frac{\sqrt{m}\Omega_1}{2}\left[\sigma_{m,m-1}+\sigma_{m-1,m},\tilde{\rho}^{(0)}\right] \\
&+ \sum_{m,n=1}^{M-1}\frac{\sqrt{mn}\gamma_{m,m-1}}{2}\left(\left[\sigma_{m-1,m}\tilde{\rho}^{(0)},\sigma_{n,n-1}\right]+\left[\sigma_{n-1,n},\tilde{\rho}^{(0)}\sigma_{m,m-1}\right]\right) \\
&+ \sum_{m,n=1}^{M-1}\frac{mn\gamma^{\phi}}{2}\left(\left[\sigma_{mm}\tilde{\rho}^{(0)},\sigma_{nn}\right]+\left[\sigma_{nn},\tilde{\rho}^{(0)}\sigma_{mm}\right]\right),
\end{aligned} \tag{3.1.4}$$

doi:10.6342/NTU202503909

and

$$
\begin{aligned}
\frac{d\tilde{\rho}^{(1)}}{dt} &= i\left(\omega_{d2}-\omega_{d1}\right) \\
&+ i\sum_{m=0}^{M-1}\left(m\omega_{d1}-\omega_m\right)\left[\sigma_{mm},\tilde{\rho}^{(1)}\right] \\
&+ i\sum_{m=1}^{M-1}\frac{\sqrt{m}\Omega_1}{2}\left[\sigma_{m,m-1}+\sigma_{m-1,m},\tilde{\rho}^{(1)}\right] \\
&+ i\sum_{m=1}^{M-1}\sqrt{m}\gamma_{10}\left[\sigma_{m,m-1},\tilde{\rho}^{(0)}\right] \\
&+ \sum_{m,n=1}^{M-1}\frac{\sqrt{mn}\gamma_{m,m-1}}{2}\left(\left[\sigma_{m-1,m}\tilde{\rho}^{(1)},\sigma_{n,n-1}\right]+\left[\sigma_{n-1,n},\tilde{\rho}^{(1)}\sigma_{m,m-1}\right]\right) \\
&+ \sum_{m,n=1}^{M-1}\frac{mn\gamma^{\phi}}{2}\left(\left[\sigma_{mm}\tilde{\rho}^{(1)},\sigma_{nn}\right]+\left[\sigma_{nn},\tilde{\rho}^{(1)}\sigma_{mm}\right]\right).
\end{aligned}
\tag{3.1.5}
$$

By numerically solving these coupled equations, we compute the first-order correction $\tilde{\rho}^{(1)}(t)$, from which the expectation value $\langle\sigma_{m-1,m}(t)\rangle = \frac{\Omega_2}{\gamma_{10}}\mathrm{Tr}\left[\sigma_{m-1,m}\tilde{\rho}^{(1)}(t)\right]e^{i\omega_{d1}t}$ can be evaluated. This allows us to determine the reflection coefficient and thereby characterize the transmon's parameters. Fig.3.1 shows the reflection coefficient as a function of the probe frequency and pump power. We first observe that for pump powers $P < -20$ dBm, only a single resonance is visible at $\omega_{d2}/2\pi = 4.82$ GHz. In this regime, the pump field is too weak to significantly populate the second excited state $|2\rangle$, so the observed bright stripe corresponds to the $|0\rangle \leftrightarrow |1\rangle$ transition, indicating that $\omega_{10}/2\pi = 4.82$ GHz. As the pump power increases to the range -20 dBm $< P < 0$ dBm, a second bright stripe emerges at $\omega_{d2}/2\pi = 4.50$ GHz, signaling $|1\rangle \leftrightarrow |2\rangle$ transition. This allows us to extract the charging energy of the transmon as $E_C/h = \omega_{10}/2\pi - \omega_{21}/2\pi = 320$ MHz. By substituting these extracted parameters into Eq. (3.1.2), and performing a fitting procedure, we further determine the linewidth $\gamma_{10}/2\pi = 44.20$ MHz and pure dephasing rate $\gamma^{\phi}/2\pi = 0.37$ MHz. It is also noteworthy that, in this work (not shown here), we examined the steady-state population distribution under the given pump power range and found that populations for levels $M \geq 5$ are negligible. This allows us to truncate the Hilbert space at $M = 4$ for all

doi:10.6342/NTU202503909

numerical simulations. To accurately determine the Rabi frequency of the pump field, we modify the formula provided in Ref. [2] by introducing a calibration factor. Specifically, we introduce a tuning parameter η into the driving amplitude $\frac{\Omega}{2\pi} = \eta k_e \sqrt{10^{(P_{\text{ref}}+P)/10-3}}$, where we find $\eta = 2.66$, and apply this calibrated factor in all subsequent calculations.

(a)

$\omega_{10}/2\pi$ (GHz)	$\gamma_{10}/2\pi$ (MHz)	$\gamma^{\phi}/2\pi$ (MHz)	E_C/h (MHz)
4.82	44.20	0.37	320

(b)

P_{ref} (dBm)	k_e (GHz/$\sqrt{\text{W}}$)
-123.6	6886295

Table 3.1: (a) Basic parameters of the transmon sample. The quantity E_C/h denotes the charging energy, and $\omega_{10}/2\pi$ is the transition frequency between the ground and first excited states $|0\rangle \leftrightarrow |1\rangle$. The decay rate and pure dephasing rate between these two levels are given by $\gamma_{10}/2\pi$ and $\gamma^{\phi}/2\pi$, respectively. Higher-level transition frequencies are determined from Eq. (1.2.11), and the corresponding decay rates are scaled as $\gamma_{m,m-1} = \gamma_{10} \cdot (\omega_{m,m-1}/\omega_{10})$ [2]. (b) Experimental values for P_{ref} and k_e.

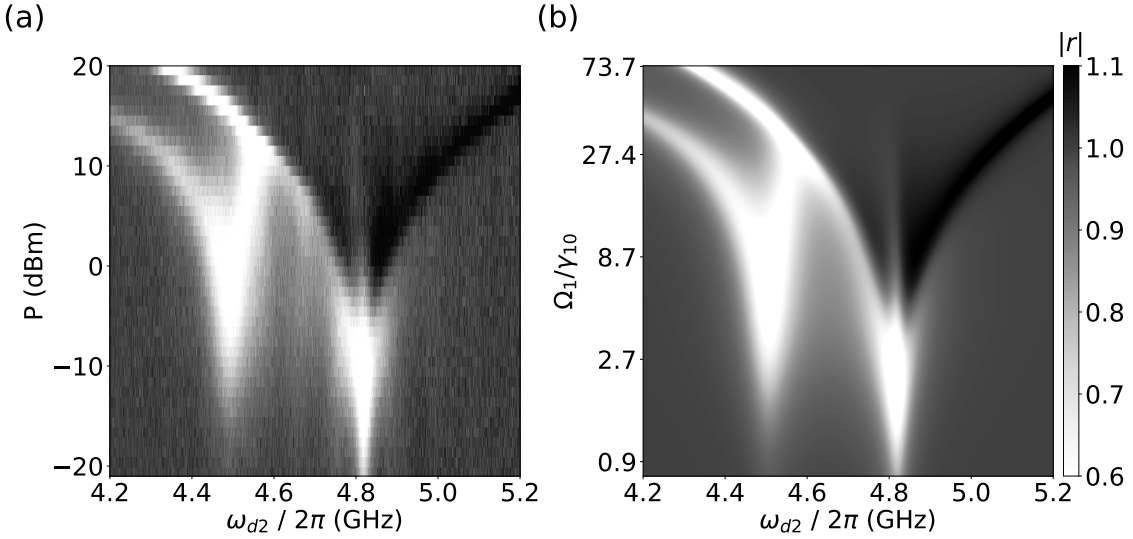

Figure 3.1: (a) Experimentally measured reflection coefficient as a function of probe frequency ω_{d2} and pump power P. The dip near $4.82\,\text{GHz}$ corresponds to the $|0\rangle \leftrightarrow |1\rangle$ transition. As the pump power increases, it splits due to the Autler–Townes splitting. The dip near $4.50\,\text{GHz}$ corresponds to the $|1\rangle \leftrightarrow |2\rangle$ transition. From the difference between these two frequencies, the charging energy is estimated to be $E_C = 320\,\text{MHz}$. (b) Theoretically calculated reflection coefficient, used to determine the scaling factor $\eta = 2.66$ by matching with the experimental result in (a).

doi:10.6342/NTU202503909

3.2 Power-Tunable Frequency Conversion

In the previous section, we discussed how the fundamental parameters of the transmon can be extracted from the reflection coefficient. We now turn our attention to the single-atom wave-mixing process by analyzing the emission spectra introduced in Chapter 2.

We begin by considering a simple case in which the carrier frequencies of the two-tone drives are set to $\omega_{d1}/2\pi = 4.82\,\text{GHz}$ and $\omega_{d2}/2\pi = 4.825\,\text{GHz}$. The power of the second drive is chosen as $P_2 = -1$ dBm. Figure 3.2 displays the emission spectrum as a function of the incident power P_1.

In this configuration, we observe that the frequency generation process can be actively manipulated by tuning the relative strengths of the two driving fields. When $P_1 > P_2$ ($P_1 < P_2$), the red (blue) sidebands dominate the spectral response, as indicated by arrows with negative (positive) indices. Notably, when the driving strengths are equal, $P_1 = P_2$, the emission spectrum becomes symmetric, resulting in the formation of a frequency comb, as shown in Fig. 3.3

Our formalism also allows for the prediction of generated frequencies through Eq. (2.3.15):

$$\omega_p = \omega_s + p\delta = \left(\frac{1-p}{2}\right)\omega_{d1} + \left(\frac{1+p}{2}\right)\omega_{d2}. \tag{3.2.1}$$

This equation reveals that frequency components associated with odd integers p can be produced. In contrast, those with even p are absent—a consequence of the inability to absorb or emit fractional photons.

doi:10.6342/NTU202503909

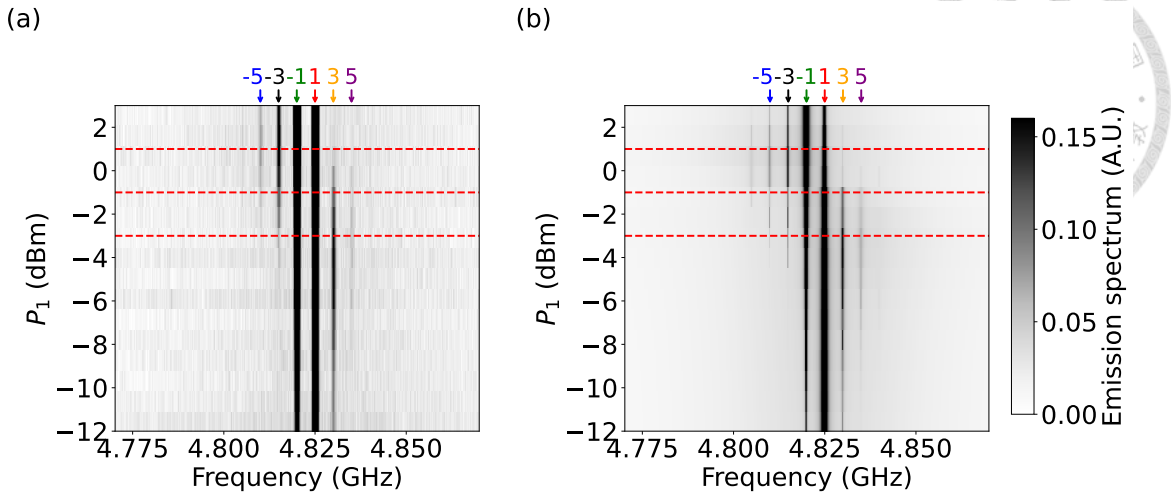

Figure 3.2: Emission spectra as function of input power P_1, with fixed driving frequencies $\omega_{d1}/2\pi = 4.82\,\text{GHz}$, $\omega_{d2}/2\pi = 4.825\,\text{GHz}$, and fixed $P_2 = -1\,\text{dBm}$. Panel (a) shows the measured spectrum, while panel (b) displays the corresponding theoretical result. The top numbers indicate the sideband index p. The two central lines correspond to the input driving tones ($p = \pm 1$). As P_1 increases, higher-order blue sidebands (e.g., $p = +3, +5$) gradually become visible, while red sidebands (e.g., $p = -3, -5$) become more pronounced once $P_1 > P_2$. Arrows mark the power levels at which the line cuts in Fig. 3.3 are taken.

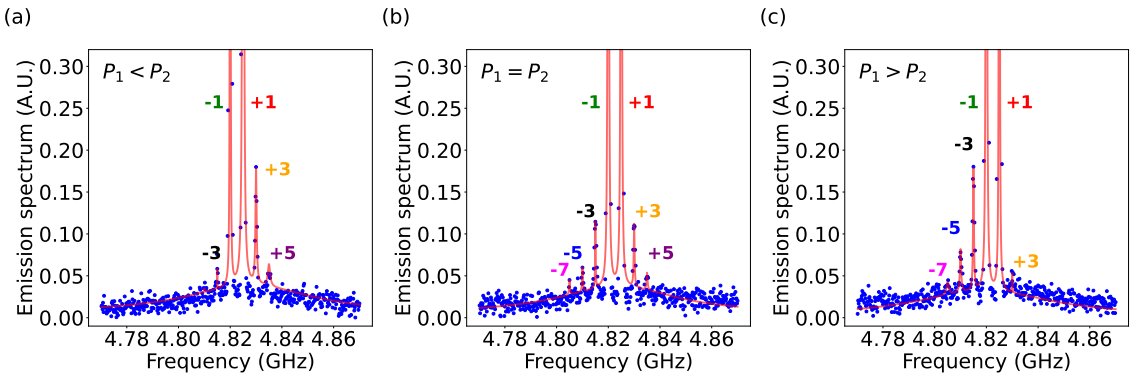

Figure 3.3: Measured and simulated emission spectra under bichromatic driving at $\omega_{d1}/2\pi = 4.82$ GHz and $\omega_{d2}/2\pi = 4.825$ GHz, with fixed $P_2 = -1$ dBm. The three panels correspond to different values of P_1: (a) $P_1 = -3\,\text{dBm}$, where blue sidebands emerge on the right side of the driving tones, such as $p = +3$ at $2\omega_{d2} - \omega_{d1}$ and $p = +5$ at $3\omega_{d2} - 2\omega_{d1}$; (b) $P_1 = -1\,\text{dBm}$, where sidebands become more symmetric, and peaks at $p = \pm 3, \pm 5$ are observed on both sides; (c) $P_1 = 1\,\text{dBm}$, where red sidebands on the left become dominant, including $p = -3$ at $2\omega_{d1} - \omega_{d2}$ and $p = -5$ at $3\omega_{d1} - 2\omega_{d2}$. Blue dots are experimental data; solid red curves are theoretical fits.

doi:10.6342/NTU202503909

3.3 Understanding Spectral Peaks via Dyson Expansion

In previous sections, we provided a heuristic explanation suggesting that the transmon cannot absorb or emit fractional photons, leading to frequency generation only at odd values of p. In this section, our objective is to quantitatively investigate the underlying mechanism using the Dyson series formalism outlined in Sec. 1.3.2.

Following a procedure similar to that in Sec. 1.3.2, we begin by expressing the atomic ladder operators as

$$\langle \tilde{\sigma}_{m-1,m}(t;t_0)\rangle = \sum_{k=0}^{\infty} \langle \sigma_{m-1,m}(t;t_0)\rangle_D^{(k)}\, e^{i\omega_s t} \quad , \tag{3.3.1}$$

where the kth-order Dyson contribution is given by

$$\begin{aligned}\langle \sigma_{m-1,m}(t;t_0)\rangle_D^{(k)} = \sum_{k'+k''=k} \mathrm{Tr}_{S\otimes B}\Big[\Big(U^{(k')}(t;t_0)\Big)^{\dagger} \\ \cdot\, \sigma_{m-1,m}\, U^{(k'')}(t;t_0)\, \rho_{tot}^{(S)}(t_0)\Big]\, e^{-i\omega_{m,m-1}(t-t_0)},\end{aligned} \tag{3.3.2}$$

with $U^{(k')}(t;t_0)$ denoting the k'th-order time-evolution operator and $\rho_{tot}^{(S)}(t_0)$ is the initial system–bath density matrix. It is important to note that the initial state of the transmon–waveguide system is required to evaluate Eq. (3.3.2). To evaluate Eq. (3.3.2), we must specify the initial state of the transmon–waveguide system. In our case, this state is given by $|\Psi(t_0)\rangle = |m\rangle \otimes |\alpha_1\rangle \otimes |\alpha_2\rangle$, where $|m\rangle$ denotes the transmon in its mth level, and $|\alpha_1\rangle$ and $|\alpha_2\rangle$ represent the two driving fields, each in a coherent photonic state.

By substituting $\rho_{tot}^{(S)}(t_0) = |\Psi(t_0)\rangle\langle\Psi(t_0)|$ into Eq. (3.3.2), we find a key result:

$$\langle \tilde{\sigma}_{m-1,m}(t)\rangle_D^{(k)} = 0 \tag{3.3.3}$$

for even k. This implies that the observable contributions to frequency generation arise only from odd-order terms in the Dyson series—providing a rigorous explanation for the absence of frequencies associated with even p coherent part of the emission spectrum. The

doi:10.6342/NTU202503909

first-order contribution, i.e., $k = 1$, is given by

$$\langle \tilde{\sigma}_{m-1,m}(t) \rangle_D^{(1)} = \sum_{i=1}^{2} g_i \alpha_i \left[C_{i,-}^{(m)}(t) \right]^* e^{-i\omega_{m,m-1}t} e^{i\omega_s t}, \tag{3.3.4}$$

where g_i is the coupling strength, α_i is the coherent amplitude of the ith driving field, and the coefficient $C_{i,-}^{(m)}(t)$ captures the corresponding one-photon pathways. All Dyson coefficients in this section, including those for higher-order terms, are listed explicitly in Appendix A. This process is illustrated schematically in Fig. 3.4(a). The third-order contribution, $k = 3$ describes various three-photon processes and is given by:

$$\begin{aligned} \langle \tilde{\sigma}_{m-1,m}(t) \rangle_D^{(3)} = \sum_{i,j,r=1}^{2} g_r g_j g_i \Big\{ & \alpha_r \alpha_j \alpha_i^* \left[C_{rji,--+}^{(m,m-1,m-1)}(t) \right]^* \\ & + \alpha_r \alpha_j^* \alpha_i \left[C_{rji,-+-}^{(m,m,m)}(t) \right]^* \\ & + \alpha_r^* \alpha_j \alpha_i \left[C_{rji,+--}^{(m+1,m+1,m)}(t) \right]^* \\ & + \alpha_r \alpha_j^* \alpha_i \left[C_{r,-}^{(m)}(t) \right]^* C_{ji,-+}^{(m+1,m+1)}(t) \\ & + \alpha_r \alpha_j \alpha_i^* \left[C_{r,-}^{(m)}(t) \right]^* C_{ji,+-}^{(m,m)}(t) \Big\} e^{-i\omega_{m,m-1}t} e^{i\omega_s t}. \end{aligned} \tag{3.3.5}$$

Each term in this expression corresponds to a distinct physical process involving three photons, as schematically illustrated in Fig. 3.4(b).

doi:10.6342/NTU202503909

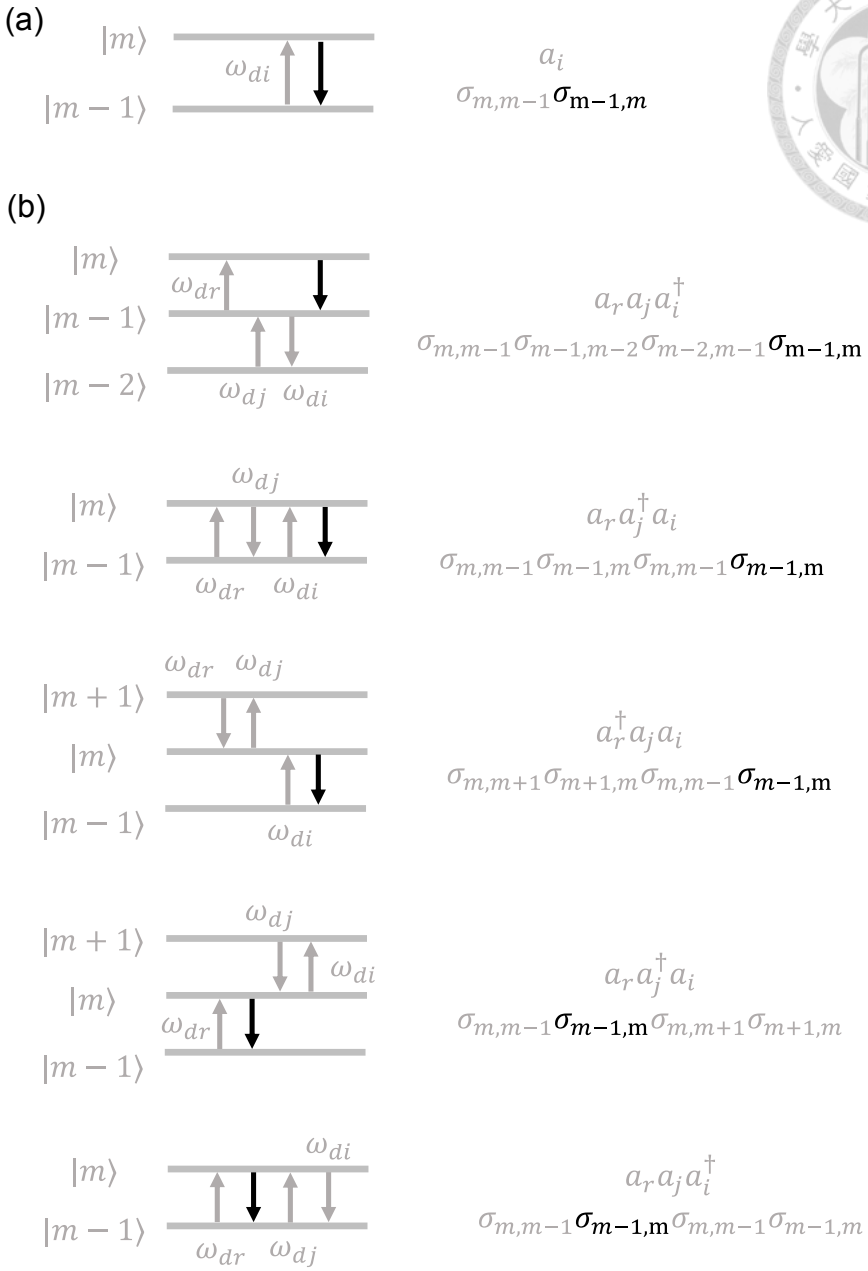

Figure 3.4: (a) Diagram of a first-order (single-photon) process contributing to the expectation value $\langle\tilde{\sigma}_{m-1,m}(t)\rangle$, where a single photon from mode i induces a direct transition between $|m-1\rangle$ and $|m\rangle$. (b) Various types of third-order (three-photon) processes. Each process involves the absorption and emission of three photons across different energy levels. The corresponding operator orderings are shown on the right, and the black arrow denotes the final observable transition.

To evaluate the coherent part of the emission spectrum, we substitute Eq. 3.3.1 into Eq. 2.3.12, yielding the first-order contribution:

doi:10.6342/NTU202503909

$$S^{(1)}_{co;mm}(\omega) = \int_0^\infty \sum_{i,i'=1}^{2} g_i g_{i'} \mathcal{I}^{(1)}(t+\tau, t) \cdot e^{i\omega_{m,m-1}\tau} e^{-i(\omega-\omega_s)\tau}\, d\tau, \tag{3.3.6}$$

with

$$\mathcal{I}^{(1)}_{i,i'}(t+\tau, t; m) = \alpha^*_i \alpha_{i'} C^{(m)}_{i,-}(t+\tau) \left(C^{(m)}_{i',-}(t)\right)^* = m \frac{e^{i\Delta^{(m)}_i (t+\tau)} e^{-i\Delta^{(m)}_{i'} t}}{\Delta^{(m)}_i \Delta^{(m)}_{i'}}. \tag{3.3.7}$$

Here, $\Delta^{(m)}_i$ represents the frequency detuning component associated with the i-th driving field and mth level of transition. It is important to note that in the time-averaged spectrum, only terms with $\Delta^{(m)}_i = \Delta^{(m)}_{i'}$ contribute, due to rapid phase oscillations averaging out the cross terms. Consequently, Eq. (3.3.6) simplifies to

$$\bar{S}^{(1)}_{co;mm}(\omega) = \sum_{i=1}^{2} \frac{m \left|g_i \alpha_i\right|^2}{\left(\Delta^{(m)}_i\right)^2} \delta\left(\omega - \omega_{di}\right), \tag{3.3.8}$$

from which we see that the coherent single-photon emission process results in two dominant peaks located at the driving frequencies ω_{d1} and ω_{d2} in the emission spectrum. These peaks reflect direct radiative transitions stimulated by the corresponding drive fields.

Following a similar procedure for the third-order term ($k = 3$), we obtain:

$$S^{(3)}_{co;mm}(\omega) = \int_0^\infty \sum_{i,j,r,i',j',r'=1}^{2} g_i g_j g_r g_{i'} g_{j'} g_{r'} \mathcal{I}^{(3)}_{i,j,r,i',j',r'}(t+\tau, t; m) \cdot e^{i\omega_{m,m-1}\tau} e^{-i(\omega-\omega_s)\tau}\, d\tau. \tag{3.3.9}$$

In the time-averaged spectrum, the dominant contributions arise from resonant conditions among the detunings. Specifically, only the terms satisfying any of the following resonance conditions contribute significantly:

doi:10.6342/NTU202503909

$$\begin{aligned}
&\Delta_r^{(m)} + \Delta_j^{(m-1)} - \Delta_i^{(m-1)} + \Delta_{r'}^{(m-1)} - \Delta_{j'}^{(m-1)} - \Delta_{i'}^{(m)} = 0, \\
&\Delta_r^{(m)} - \Delta_j^{(m)} + \Delta_i^{(m)} - \Delta_{r'}^{(m)} + \Delta_{j'}^{(m)} - \Delta_{i'}^{(m)} = 0, \\
&\Delta_r^{(m)} + \Delta_j^{(m+1)} - \Delta_i^{(m+1)} + \Delta_{r'}^{(m+1)} - \Delta_{j'}^{(m+1)} - \Delta_{i'}^{(m)} = 0.
\end{aligned} \tag{3.3.10}$$

Under these conditions, the third-order time-averaged spectrum takes the form:

$$\bar{S}^{(3)}_{\mathrm{co};mm}(\omega) \propto \sum_{i,j,r=1}^{2} \left|g_i g_j g_r \alpha_i \alpha_j \alpha_r\right|^2 \delta\left(\omega - (\omega_{di} + \omega_{dj} - \omega_{dr})\right), \tag{3.3.11}$$

which represents three-photon processes generating new frequencies, such as ω_{d1}, ω_{d2}, $2\omega_{d1} - \omega_{d2}$, and $2\omega_{d2} - \omega_{d1}$, as combinations of the input drive tones. This result highlights the nonlinear nature of the frequency mixing process mediated by the multilevel structure of the transmon.

By the same reasoning, a K-photon process (i.e., $k = K$) can generate emission at frequencies up to

$$\omega_K = \pm\left(K\omega_{d1} - (K-1)\omega_{d2}\right), \tag{3.3.12}$$

representing the highest-order sideband from the process. A comprehensive summary of the emission frequencies generated by various multi-photon processes is presented in Fig. 3.5.

doi:10.6342/NTU202503909

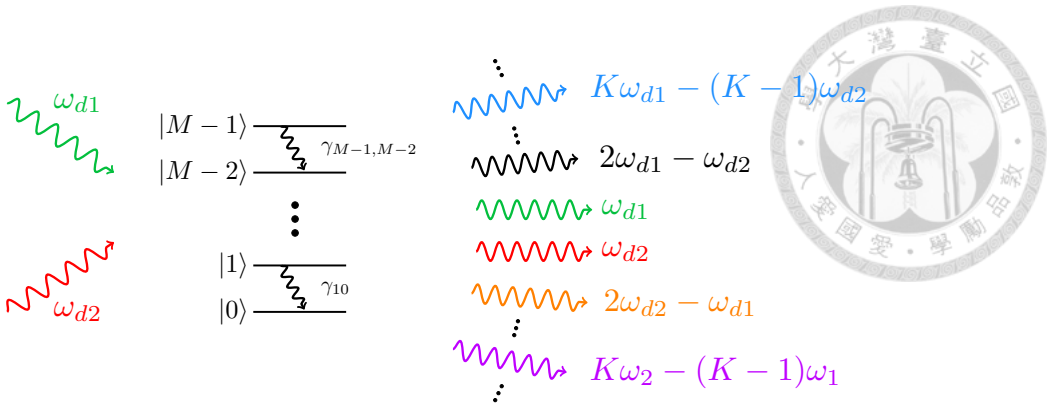

Figure 3.5: Schematic illustration of the emitted frequency components resulting from wave-mixing process in an M-level atom driven by two coherent fields at frequencies ω_{d1} and ω_{d2}. Each colored arrow on the right indicates a frequency component generated through coherent multi-photon mixing of the input tones. The green and red arrows represent the input frequencies ω_{d1} and ω_{d2}, respectively. The orange and black arrows denote the first sidebands arising from three-photon processes: $2\omega_2 - \omega_1$ and $2\omega_1 - \omega_2$. The higher-order components, labeled $K\omega_{d1} - (K-1)\omega_{d2}$ and $K\omega_{d2} - (K-1)\omega_{d1}$, illustrate the general structure of sidebands produced by K-photon process.

3.4 Detuning-Controlled Frequency Conversion

In Sec. 3.2, we demonstrated that when the two driving fields have equal strengths, $P_1 = P_2$, the resulting emission spectrum exhibits a symmetric frequency comb. The Dyson-series analysis in the previous section further revealed that each peak within this spectrum corresponds to a distinct multi-photon transition pathway. Motivated by this insight, we now investigate whether higher-order sidebands can be enhanced by increasing the drive strengths. The underlying idea is that stronger driving fields can populate higher excited states of the transmon, thereby opening up more efficient multi-photon pathways responsible for generating higher-order spectral components. To explore this, we set both drive powers to a relatively strong value of $P_1 = P_2 = 2$ dBm, and apply symmetric detuning around the $|0\rangle \leftrightarrow |1\rangle$ transition frequency by a tunable offset $\Delta\omega$, such that $\omega_{d1}/2\pi = \omega_{10}/2\pi - \Delta\omega/2\pi$ and $\omega_{d2}/2\pi = \omega_{10}/2\pi + \Delta\omega/2\pi$.

Figure 3.6 presents the emission spectrum as a function of the detuning $\Delta\omega/2\pi$. The two central, prominent black lines correspond to the driving frequencies $\omega_{d1}/2\pi$ and $\omega_{d2}/2\pi$. To the right of $\omega_{d2}/2\pi$, blue sidebands appear, while to the left of $\omega_{d1}/2\pi$, red sidebands emerge. These sidebands arise from multiphoton transitions of various orders involving

doi:10.6342/NTU202503909

different combinations of the two drives. As the detuning $\Delta\omega/2\pi$ increases, the sideband frequencies shift further outward, resulting in a broader frequency comb with increased spacing between adjacent spectral peaks.

Importantly, we find that many higher-order sidebands remain visible even at large detunings, indicating that strong drive powers can effectively sustain the nonlinear mixing processes. In addition to the emergence of high-order peaks, we also observe that the amplitude of a given-order sideband remains nearly constant as $\Delta\omega$ increases. This suggests that the efficiency of a fixed-order wave-mixing process is not significantly diminished by detuning, further validating our strategy of using strong drives to achieve robust frequency conversion.

Moreover, the spacing between adjacent spectral peaks is directly controlled by the detuning $\Delta\omega$, allowing for tunable frequency spacing in the resulting comb. Fig 3.7(a) and 3.7(b) show the emission spectra at two representative detunings, $\Delta\omega/2\pi = 12\,\text{MHz}$ and $\Delta\omega/2\pi = 26\,\text{MHz}$, respectively. In both cases, the output forms a frequency comb consisting of evenly spaced peaks, with clearly different spacings between the two panels. This confirms that the comb spacing can be flexibly tuned by adjusting the drive detuning.

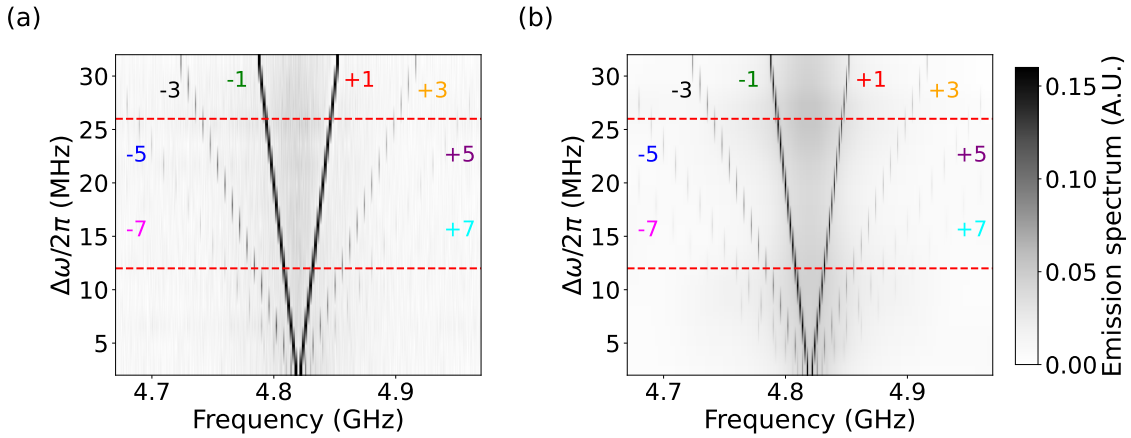

Figure 3.6: Emission spectra as function of detuning $\Delta\omega/2\pi$, with fixed input powers $P_1 = P_2 = 2\,\text{dBm}$. The driving frequencies are chosen as $\omega_{d1}/2\pi = \omega_{10}/2\pi - \Delta\omega/2\pi$ and $\omega_{d2}/2\pi = \omega_{10}/2\pi + \Delta\omega/2\pi$, where $\omega_{10}/2\pi = 4.82\,\text{GHz}$. Panel (a) shows the experimental results, and panel (b) displays the corresponding theoretical simulation. As detuning increases, frequency-converted sidebands emerge and shift accordingly.

doi:10.6342/NTU202503909

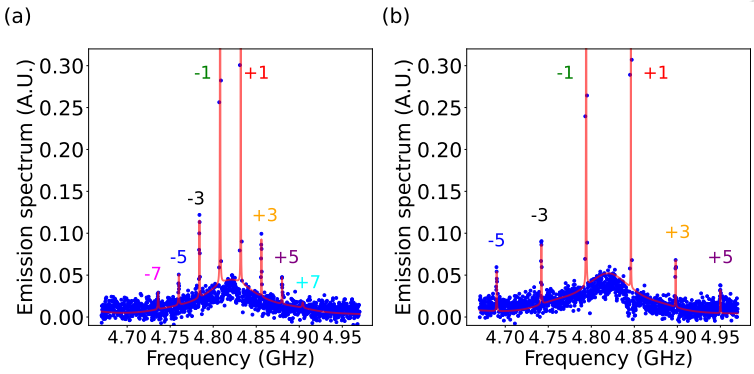

Figure 3.7: Linecuts of the emission spectrum at two different drive detunings: (a) $\Delta\omega/2\pi = 12\,\text{MHz}$ and (b) $\Delta\omega/2\pi = 26\,\text{MHz}$. Both spectra exhibit a frequency comb structure resulting from wave-mixing processes between the two drives. The spacing between adjacent peaks is determined by the detuning $\Delta\omega/2\pi$, allowing for tunable frequency conversion. In panel (a), higher-order components such as $p = \pm 7$ at $\pm\left(4\omega_{d1} - 3\omega_{d2}\right)$ are also observed, although with reduced amplitude.

3.5 Influence of Number of Atomic Levels

Building on the analysis in Sec. 3.3, where the height of a side peak is shown to arise from multiple quantum pathways, it follows that the number of atomic levels involved can significantly impact the side peak strength. In this section, we numerically investigate how the inclusion of different numbers of atomic levels affects the side peaks in a comb-like spectrum. We perform simulations using two-, three-, four-, and five-level atomic models, systematically varying the input power while keeping the drive frequencies fixed. This approach allows us to assess the influence of level truncation on the formation and intensity of side peaks.

Figure 3.8 illustrates the relative height of four representative side peaks—$p = \pm 3$ and ± 5—as a function of input power, under fixed drive frequencies $\omega_{d1/d2}/2\pi = 4.82\,\text{GHz} \pm 12\,\text{MHz}$. For each case, we compare the simulation results using atomic models truncated at two, three, four, and five levels. At low power (-30 to -20 dBm), the population in higher excited states remains negligible, and the dynamics are well described by lower-level truncations. As a result, the simulation results from all four truncation cases closely overlap in this regime. As the input power increases, we observe that models including more atomic levels generally yield significantly stronger side peaks, particularly in the

doi:10.6342/NTU202503909

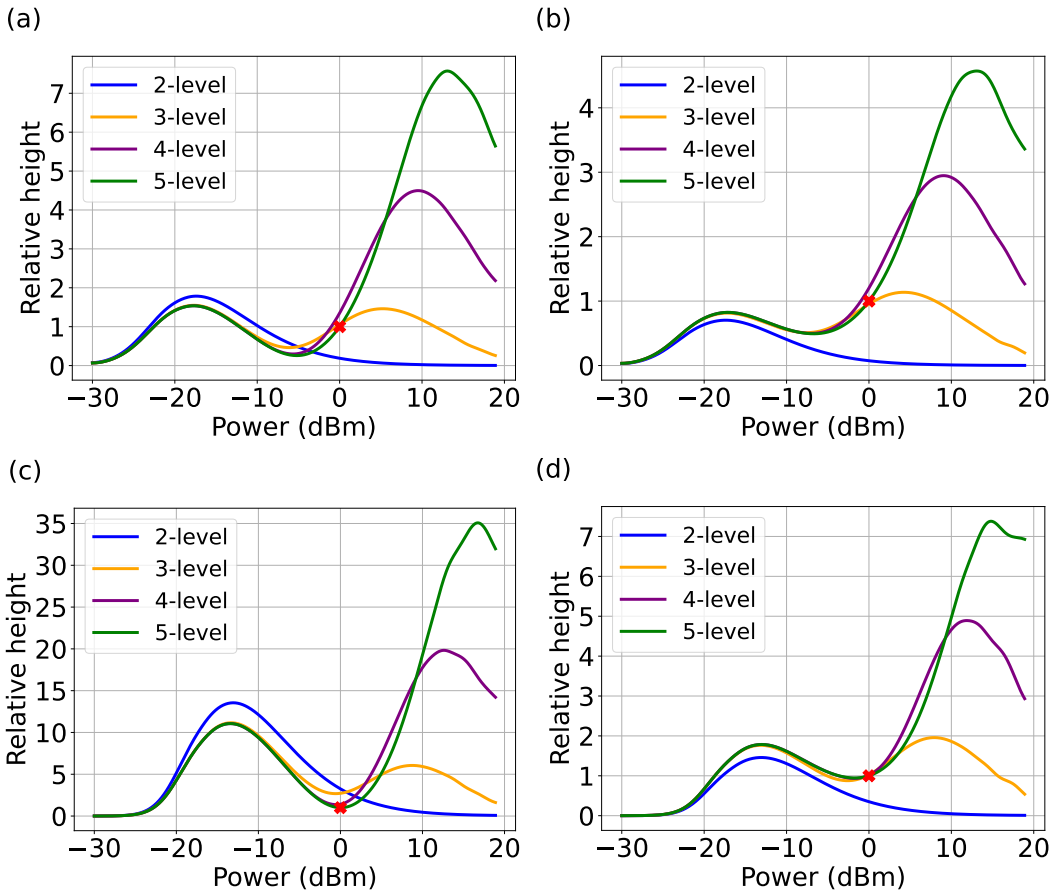

Figure 3.8: Relative height of selected side peaks as a function of driving power, comparing two-, three-, four-, and five-level atomic models. Panels (a)–(d) correspond to the side peaks with indices $p = +3$, -3, $+5$, and -5, respectively. The drive frequencies are fixed at $\omega_{d1/d2}/2\pi = 4.82\,\mathrm{GHz} \pm 12\,\mathrm{MHz}$, and the input power is varied from -30 to 20 dBm. Each curve is normalized by the corresponding peak height obtained from the five-level model at 0 dBm. Red crosses indicate the normalization reference points.

doi:10.6342/NTU202503909

high-power regime (5 to 20 dBm). This reflects the growing importance of higher-order quantum pathways that involve transitions through higher excited states.

These results highlight the breakdown of the few-level approximation in the strong-driving regime and emphasize the necessity of including higher excited states to accurately capture the nonlinear spectral response. In particular, the emergence of secondary peak maxima at higher input powers—absent in the two-level model—demonstrates how higher-order quantum pathways enabled by additional atomic levels can substantially enhance the side peak strength.

doi:10.6342/NTU202503909

Chapter 4

Conclusions

In this thesis, we have investigated quantum wave mixing in a waveguide QED system consisting of a multi-level transmon artificial atom driven by two coherent microwave fields. By combining Floquet analysis with a Dyson series formalism, we systematically identified the underlying multi-photon processes responsible for the formation of spectral sidebands. This theoretical framework offers a comprehensive approach to interpreting wave-mixing behavior in strongly driven quantum systems.

Our results demonstrate that the strength and asymmetry of the generated sidebands can be dynamically controlled by tuning the relative amplitudes of the two driving fields, thereby enabling efficient and tunable frequency conversion. Additionally, we have shown that the inclusion of higher excited states in the transmon significantly modifies the nonlinear optical response by introducing new quantum pathways. These higher-level pathways affect both the amplitude and structure of the spectral sidebands in ways that are not captured by simpler few-level models.

Theoretical predictions based on our approach closely match experimental observations, providing deeper insight into light–matter interactions in the strongly driven, multi-level regime. These findings open up promising opportunities for quantum photonic technologies, including controllable frequency converters, frequency comb generators, frequency-selective photon routers, and chip-integrated quantum light sources.

Looking ahead, we propose extending the Dyson-series-based framework to incorporate dissipation and decoherence effects. This would enable us to study how environmental

doi:10.6342/NTU202503909

interactions impact individual quantum pathways, potentially allowing selective enhancement or suppression of specific multi-photon processes. Such control could pave the way for engineered wave-mixing dynamics tailored to generate desired frequency components or quantum states on demand.

doi:10.6342/NTU202503909

doi:10.6342/NTU202503909

doi:10.6342/NTU202503909

Appendix A

Dyson Series for a M-Level Atom Coupled to Two Coherent Fields

This appendix provides the explicit expressions for the Dyson expansion terms for an M-level atomic system coupled to two classical coherent fields. These expressions are intended as a reference to support the analysis in Sec. 3.3.

Let $U(t;t_0)$ denote the interaction-picture time-evolution operator generated by the interaction Hamiltonian given in Eq. (1.3.7). By Eq. (1.3.9), the time-evolution operator $U(t)$ is expanded as a Dyson series in powers of the coupling constants:

$$U(t;t_0) = \sum_{k=0}^{\infty} U^{(k)}(t;t_0), \tag{A.0.1}$$

with the kth order term

$$U^{(k)}(t;t_0) = \left(-\frac{i}{\hbar}\right)^k \int_{t_0}^{t} dt_k \int_{t_0}^{t_k} dt_{k-1} \cdots \int_{t_0}^{t_2} dt_1 \, H_{\text{int}}^{(I)}(t_k) \cdots H_{\text{int}}^{(I)}(t_1). \tag{A.0.2}$$

In the steady-state limit, we average over the initial time t_0 according to

$$\bar{U}^{(k)}(t) = \lim_{T\to\infty} \frac{1}{T} \int_{-T}^{0} dt_0 \, U^{(k)}(t;t_0). \tag{A.0.3}$$

doi:10.6342/NTU202503909

Below, we list the explicit expressions for $\bar{U}^{(k)}(t)$ up to $k = 3$.

- **Zeroth-order Dyson term.** This term corresponds to the identity operator, representing free evolution:

$$\bar{U}^{(0)}(t) = I. \tag{A.0.4}$$

- **First-order Dyson term.** The time-averaged first-order contribution is given by

$$\bar{U}^{(1)}(t) = \sum_{i=1}^{2} \sum_{m=1}^{M-1} g_i \left(C_{i,+}^{(m)}(t) a_i \sigma_{m,m-1} + C_{i,-}^{(m)}(t) a_i^\dagger \sigma_{m-1,m} \right), \tag{A.0.5}$$

where the coefficients are

$$\frac{1}{\sqrt{m}} C_{i,+}^{(m)}(t) = \frac{e^{-i\Delta_i^{(m)} t}}{\Delta_i^{(m)}}, \tag{A.0.6}$$

$$C_{i,-}^{(m)}(t) = -\left[C_{i,+}^{(m)}(t) \right]^*. \tag{A.0.7}$$

- **Second-order Dyson term.** The time-averaged second-order contribution takes the form

$$\begin{aligned} \bar{U}^{(2)}(t) = \sum_{i,j=1}^{2} \sum_{m,n=1}^{M-1} g_j g_i \Big(& C_{ji,++}^{(nm)}(t) a_j a_i \sigma_{n,n-1} \sigma_{m,m-1} \\ & + C_{ji,-+}^{(nm)}(t) a_j^\dagger a_i \sigma_{n-1,n} \sigma_{m,m-1} \\ & + C_{ji,+-}^{(nm)}(t) a_j a_i^\dagger \sigma_{n,n-1} \sigma_{m-1,m} \\ & + C_{ji,--}^{(nm)}(t) a_j^\dagger a_i^\dagger \sigma_{n-1,n} \sigma_{m-1,m} \Big), \end{aligned} \tag{A.0.8}$$

where the coefficients are

$$\frac{1}{\sqrt{mn}} C_{ji,\pm+}^{(nm)}(t) = \frac{1}{\Delta_i^{(m)}} \frac{e^{-i\left(\pm\Delta_j^{(n)} + \Delta_i^{(m)}\right) t}}{\pm\Delta_j^{(n)} + \Delta_i^{(m)}} \tag{A.0.9}$$

doi:10.6342/NTU202503909

and

$$C^{(nm)}_{ji,\mp-}(t) = \left[C^{(nm)}_{ji,\pm+}(t)\right]^*. \tag{A.0.10}$$

- **Third-order Dyson term.** The time-averaged third-order contribution is expressed as

$$\begin{aligned}
\bar{U}^{(3)}(t) = \sum_{i,j,k=1}^{2} \sum_{m,n,p=1}^{M-1} & g_k g_j g_i \\
& \times \Big(C^{(pnm)}_{kji,+++}(t) a_k a_j a_i \sigma_{p,p-1}\sigma_{n,n-1}\sigma_{m,m-1} \\
& + C^{(pnm)}_{kji,-++}(t)\, a_k^\dagger a_j a_i \sigma_{p-1,p}\sigma_{n,n-1}\sigma_{m,m-1} \\
& + C^{(pnm)}_{kji,+-+}(t)\, a_k a_j^\dagger a_i \sigma_{p,p-1}\sigma_{n-1,n}\sigma_{m,m-1} \\
& + C^{(pnm)}_{kji,--+}(t)\, a_k^\dagger a_j^\dagger a_i \sigma_{p-1,p}\sigma_{n-1,n}\sigma_{m,m-1} \\
& + C^{(pnm)}_{kji,++-}(t)\, a_k a_j a_i^\dagger \sigma_{p,p-1}\sigma_{n,n-1}\sigma_{m-1,m} \\
& + C^{(pnm)}_{kji,-+-}(t)\, a_k^\dagger a_j a_i^\dagger \sigma_{p-1,p}\sigma_{n,n-1}\sigma_{m-1,m} \\
& + C^{(pnm)}_{kji,+--}(t)\, a_k a_j^\dagger a_i^\dagger \sigma_{p,p-1}\sigma_{n-1,n}\sigma_{m-1,m} \\
& + C^{(pnm)}_{kji,---}(t)\, a_k^\dagger a_j^\dagger a_i^\dagger \sigma_{p-1,p}\sigma_{n-1,n}\sigma_{m-1,m} \Big),
\end{aligned} \tag{A.0.11}$$

where the coefficients are

$$\frac{1}{\sqrt{pnm}} C^{(pnm)}_{kji,\pm++}(t) = \frac{1}{\Delta_i^{(m)}} \frac{1}{\Delta_j^{(n)} + \Delta_i^{(m)}} \frac{e^{i\left(\pm\Delta_k^{(p)} + \Delta_j^{(n)} + \Delta_i^{(m)}\right)t}}{\pm\Delta_k^{(p)} + \Delta_j^{(n)} + \Delta_i^{(m)}}, \tag{A.0.12}$$

$$\frac{1}{\sqrt{pnm}} C^{(pnm)}_{kji,\pm-+}(t) = \frac{1}{\Delta_i^{(m)}} \frac{1}{-\Delta_j^{(n)} + \Delta_i^{(m)}} \frac{e^{i\left(\pm\Delta_k^{(p)} - \Delta_j^{(n)} + \Delta_i^{(m)}\right)t}}{\pm\Delta_k^{(p)} - \Delta_j^{(n)} + \Delta_i^{(m)}}, \tag{A.0.13}$$

and

$$C^{(pnm)}_{kji,\mp+-}(t) = -\left[C^{(pnm)}_{kji,\pm-+}(t)\right]^*, \tag{A.0.14}$$

doi:10.6342/NTU202503909

$$C^{(pnm)}_{kji,\mp--}(t) = -\left[C^{(pnm)}_{kji,\pm++}(t)\right]^{*}. \tag{A.0.15}$$

doi:10.6342/NTU202503909

Appendix B

Comparison of Classical and Quantum Wave Mixing

This appendix provides a brief comparison between the classical (Sec. 1.3.1) and quantum perspectives (Secs. 1.3.2 and 3.3) on wave mixing, focusing on their underlying mechanisms, implementation platforms, and the resulting frequency components.

- **Mechanism:** In the classical picture, wave mixing arises from the nonlinear polarization response of a medium, where new frequencies are generated through higher-order susceptibilities $\chi^{(n)}$ in the electric field expansion. This nonlinear polarization acts as a source term in Maxwell's equations, leading to the generation of new frequency components. In contrast, the quantum perspective describes wave mixing as the result of interference of quantum transition amplitudes between discrete energy levels. This interference leads to the emission of new frequencies corresponding to the energy differences between the initial, intermediate, and final states involved in the multi-photon process.

- **Platform:** Classical wave mixing typically occurs in macroscopic nonlinear media, such as bulk dielectric materials [77, 78, 79] or optical fiber [80, 81, 82], where the response arises from the collective behavior of a large number of atoms or molecules. In contrast, quantum wave mixing can occur in systems where individual quantum system, such as (artificial) atoms [41, 83, 84, 85, 86] or quantum

doi:10.6342/NTU202503909

dots [87, 88], interact with quantized electromagnetic fields. These platforms allow the study of quantum coherence, photon statistics, and few-photon interactions that have no classical analog.

- **Generated frequencies:** If we draw an analogy between the classical nonlinear susceptibility $\chi^{(l)}$ and the lth-order term in the Dyson expansion, and assume that the input consists of only two frequencies ω_{d1} and ω_{d2}, both approaches predict the generation of new frequency components formed by linear combinations of the inputs.

  – In the classical picture, the lth-order polarization term $\chi^{(l)}\mathbf{E}^l$ gives rise to output frequencies

  $$\omega_{\text{new}} = n_1\omega_{d1} + n_2\omega_{d2}, \tag{B.0.1}$$

  where $n_1, n_2 \in \mathbb{Z}$ and $|n_1| + |n_2| = l$. For example, at second order ($\chi^{(2)}$), possible output frequencies include

  $$2\omega_{d1}, \quad 2\omega_{d2}, \quad \omega_{d1} \pm \omega_{d2}, \tag{B.0.2}$$

  as well as their negative counterparts. At third order ($\chi^{(3)}$), the generated frequencies include

  $$3\omega_{d1}, \quad 3\omega_{d2}, \quad 2\omega_{d1} \pm \omega_{d2}, \quad 2\omega_{d2} \pm \omega_{d1}, \tag{B.0.3}$$

  along with their negative counterparts.

  – On the quantum side, the lth-order Dyson term represents a multi-photon process involving l interactions between the atom and the field. The quantum picture imposes two important constraints:

    1. Dipole-forbidden transitions: In transmon, certain transitions between energy levels are forbidden by dipole selection rules, even if the energy

doi:10.6342/NTU202503909

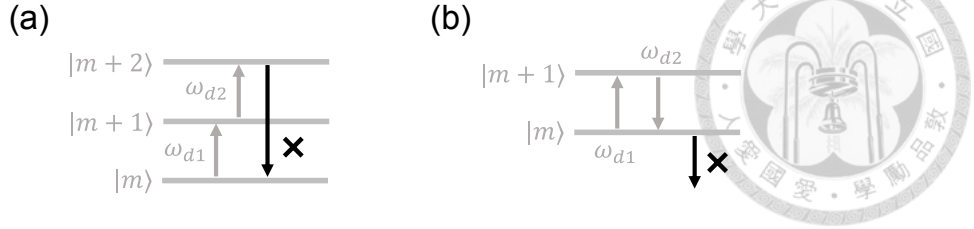

Figure B.1: (a) A transition from $|m+2\rangle \rightarrow |m\rangle$ is forbidden due to the dipole selection rule, preventing the observation of second-harmonic or sum-frequency signals. (b) A sequential two-photon process $|m\rangle \rightarrow |m+1\rangle \rightarrow |m\rangle$ leads to no net energy exchange, resulting in a vanishing contribution to observables such as the emission spectrum.

difference matches that of a single photon. For example, a direct transition between non-adjacent levels (e.g., $|m+2\rangle \rightarrow |m\rangle$) may be dipole-forbidden. As a result, frequency components that would correspond to such transitions—such as second-harmonic signals ($2\omega_{d1}$ and $2\omega_{d2}$) and sum-frequency signals ($\omega_{d1}+\omega_{d2}$)—cannot appear in the spectrum, despite being allowed in the classical picture (see Fig. B.1a).

2. Energy conservation and orthogonality: Some frequencies allowed in classical wave mixing, such as $\omega_{d1}-\omega_{d2}$, do not appear in the quantum case because they violate energy conservation. For instance, a second-order process where the atom interacts sequentially with ω_{d1} and ω_{d2} may return it to the original state without net energy exchange. Such terms vanish in observables, as the corresponding final state is orthogonal to the initial state in the Dyson expansion (see Fig. B.1b).

A direct comparison of the generated frequencies up to the fifth order is summarized in Table B.1.

doi:10.6342/NTU202503909

Order	Classical	Quantum
1st	$\omega_{d1},\ \omega_{d2}$	$\omega_{d1},\ \omega_{d2}$
2nd	$2\omega_{d1},\ 2\omega_{d2},\ \omega_{d1} \pm \omega_{d2}$	–
3rd	$3\omega_{d1},\ 3\omega_{d2},\ 2\omega_{d1} \pm \omega_{d2},$ $2\omega_{d2} \pm \omega_{d1}$	$2\omega_{d1} - \omega_{d2},\ 2\omega_{d2} - \omega_{d1}$
4th	$4\omega_{d1},\ 4\omega_{d2},\ 3\omega_{d1} \pm \omega_{d2},$ $3\omega_{d2} \pm \omega_{d1},\ 2\omega_{d1} \pm 2\omega_{d2}$	–
5th	$5\omega_{d1},\ 5\omega_{d2},\ 4\omega_{d1} \pm \omega_{d2},$ $4\omega_{d2} \pm \omega_{d1},\ 3\omega_{d1} \pm 2\omega_{d2},$ $3\omega_{d2} \pm 2\omega_{d1}$	$3\omega_{d1} - 2\omega_{d2},\ 3\omega_{d2} - 2\omega_{d1}$

Table B.1: Comparison between classical and quantum wave mixing frequencies generated by two coherent input fields at frequencies ω_{d1} and ω_{d2}. The left column lists the classically allowed frequencies arising from nonlinear polarization, as obtained from standard perturbative expansions in $\chi^{(n)}$ (see Sect. 1.3.1). The right column shows the quantum mixing frequencies derived from the coherent spectrum of an M-level cascade atomic system interacting with the same input fields (see Sect. 3.3). In contrast to the classical case, the quantum scenario is subject to additional constraints, resulting in fewer accessible frequency components at each order.

doi:10.6342/NTU202503909

Appendix C

Examples for Applying the Formalism in Sec. 1.4

C.1 Model: Multiple Transmons in a Semi-Infinite Waveguide

As an application of the master equation derived in Sec. 1.4, we consider a system of transmon qubits coupled to a semi-infinite waveguide, as illustrated in Fig. C.1. This configuration follows the setup studied in Ref. [2], except that we do not include the classical driving field. The total Hamiltonian includes the system, bath, and interaction terms. The

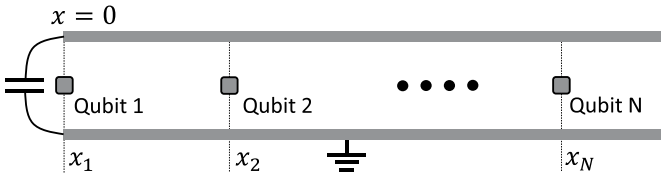

Figure C.1: Schematic of a system consisting of N transmon qubits coupled to a semi-infinite one-dimensional waveguide. The left end of the waveguide is terminated by a large capacitor, effectively forming a mirror at $x = 0$. The qubits are placed at positions $x_1, x_2, \ldots, x_N$ along the waveguide. The figure is adapted from Ref. [2].

system Hamiltonian is given by

$$H_{\mathrm{S}} = \hbar \sum_{i=1}^{N} \omega_i \sigma_i^+ \sigma_i^-, \tag{C.1.1}$$

where ω_i is the transition frequency of the i-th qubit, and $\sigma_i^{\pm}$ are the raising and lowering operators of the i-th qubit. The bath Hamiltonian describing the waveguide photon modes is

$$H_{\mathrm{B}} = \int_0^{\infty} d\omega\, \hbar\omega\, a_\omega^\dagger a_\omega, \tag{C.1.2}$$

where a_ω and $a_\omega^\dagger$ are the annihilation and creation operators of the waveguide mode with frequency ω. The interaction Hamiltonian is

$$H_{\mathrm{int}} = i\hbar \sum_{i=1}^{N} \int_0^{\infty} d\omega\, g(\omega) \cos(k_\omega x_i) \left(a_\omega \sigma_i^+ - a_\omega^\dagger \sigma_i^- \right), \tag{C.1.3}$$

where $k_\omega = \omega/v$ is the wavevector corresponding to frequency ω, and $g(\omega)$ is the coupling strength between the qubit and the waveguide mode. The $\cos(k_\omega x_i)$ factor reflects the standing wave pattern due to the mirror.

By comparing Eq. (C.1.3) with Eq. (1.4.15), we obtain the following identifications:

$$S_{i^-}^{(S)} = \sigma_i^- \tag{C.1.4}$$

$$S_{i^+}^{(S)} = \sigma_i^+ \tag{C.1.5}$$

$$B_{i^-}^{(S)} = i \int_0^{\infty} d\omega\, g_i(\omega) \cos(k_\omega x_i) a_\omega^\dagger \tag{C.1.6}$$

$$B_{i^+}^{(S)} = i \int_0^{\infty} d\omega\, g_i(\omega) \cos(k_\omega x_i) a_\omega. \tag{C.1.7}$$

Here, the summation over α (β) in Eq. (1.4.15) runs over the values

$$1^-, 1^+, 2^-, 2^+, \ldots, N^-, N^+. \tag{C.1.8}$$

Let us calculate $F_{\alpha\beta}(\omega)$, assuming that the bath is in the vacuum state. We first consider

doi:10.6342/NTU202503909

the case of $F_{i^-,j^-}(\omega)$:

$$
\begin{aligned}
F_{i^-,j^-}(\omega) &= \int_0^\infty ds\, e^{i\omega s}\langle B_{i^-}^{(I)\dagger}(s) B_{j^-}^{(I)}(0)\rangle \\
&= \int_0^\infty ds \int_0^\infty d\omega' \int_0^\infty d\omega'' g_i(\omega') g_j(\omega'') \\
&\qquad \cos(k_{\omega'} x_i)\cos(k_{\omega''} x_j) e^{-i(\omega'-\omega)}\langle 0|a_{\omega'} a_{\omega''}^\dagger|0\rangle \\
&= \int_0^\infty ds \int_0^\infty d\omega' g_i(\omega') g_j(\omega') \cos(k_{\omega'} x_i)\cos(k_{\omega'} x_j) e^{-i(\omega'-\omega)s} \\
&= \int_0^\infty d\omega' g_i(\omega') g_j(\omega') \\
&\qquad \cos(k_{\omega'} x_i)\cos(k_{\omega'} x_j)\Big[\pi\delta(\omega'-\omega) - i\mathrm{PV}\Big(\frac{1}{\omega'-\omega}\Big)\Big].
\end{aligned}
\tag{C.1.9}
$$

According to Eq. (1.4.25), we can identify the real and imaginary parts as follows:

$$
\begin{aligned}
\Gamma_{i^-,j^-}(\omega) &= \int_0^\infty d\omega' g_i(\omega') g_j(\omega') \cos(k_{\omega'} x_i)\cos(k_{\omega'} x_j)\pi\delta(\omega'-\omega) \\
&= \pi g_i(\omega) g_j(\omega)\cos(k_\omega x_i)\cos(k_\omega x_j) \\
&= \frac{\pi}{2} g_i(\omega) g_j(\omega)\Big[\cos\Big(k_\omega(x_i+x_j)\Big) + \cos\Big(k_\omega(x_i-x_j)\Big)\Big] \\
&\equiv \Gamma_{ij}(\omega)
\end{aligned}
\tag{C.1.10}
$$

and

$$
\begin{aligned}
\Delta_{i^-,j^-}(\omega) &= -\mathrm{PV}\int_0^\infty d\omega' g_i(\omega') g_j(\omega') \frac{\cos(k_{\omega'} x_i)\cos(k_{\omega'} x_j)}{\omega'-\omega} \\
&\approx -g_i(\omega) g_j(\omega)\mathrm{PV}\int_0^\infty d\omega' \frac{\cos(k_{\omega'} x_i)\cos(k_{\omega'} x_j)}{\omega'-\omega} \\
&= \frac{\pi}{2} g_i(\omega) g_j(\omega)\Big[\sin\Big(k_\omega(x_i+x_j)\Big) + \sin\Big(k_\omega(x_i-x_j)\Big)\Big] \\
&\equiv \Delta_{ij}(\omega),
\end{aligned}
\tag{C.1.11}
$$

where the approximation assumes that the coupling constants are flat around the transition frequency.

For the other terms $\Gamma_{\alpha\beta}(\omega)$, such as $\Gamma_{i^-,j^+}(\omega)$, $\Gamma_{i^+,j^-}(\omega)$, and $\Gamma_{i^+,j^+}(\omega)$, the corresponding expectation values involve terms like $\langle 0|aa|0\rangle$, $\langle 0|a^\dagger a^\dagger|0\rangle$, and $\langle 0|a^\dagger a|0\rangle$, all of

doi:10.6342/NTU202503909

which vanish in the vacuum state. Therefore, in the system considered here, the Lamb shift superoperator given by Eq. (1.4.29) reduces to

$$\mathcal{L}_{\mathrm{L}}\left[\rho(t)\right] = i\sum_{i,j}\Big[\big(\Delta_{ij}(\omega_j) - \Delta_{ji}(\omega_i)\big)\sigma_j^-\rho(t)\sigma_i^+ \\ -\Delta_{ij}(\omega_j)\sigma_i^+\sigma_j^-\rho(t) + \Delta_{ji}(\omega_i)\rho(t)\sigma_i^+\sigma_j^-\Big]\,, \tag{C.1.12}$$

where α and β each run over the values defined in Eq. (C.1.8), but only the terms with $(\alpha,\beta) = (i^-, j^-)$ contribute. As the atoms are two-level systems, ω and ω' need not be summed over, but are fixed by their respective transition frequencies. For clarity, we have dropped the superscript $^{(S)}$ and the subscript S on the density matrix $\rho_S^{(S)}(t)$ in the expression. For the dissipation superoperator, Eq. (1.4.30) takes the form:

$$\mathcal{L}_{\mathrm{D}}\left[\rho(t)\right] = \sum_{i,j}\Big[\big(\Gamma_{ij}(\omega_j) + \Gamma_{ji}(\omega_i)\big)\sigma_j^-\rho(t)\sigma_i^+ \\ -\Gamma_{ij}(\omega_j)\sigma_i^-\sigma_j^+\rho(t) - \Gamma_{ji}(\omega_i)\rho(t)\sigma_i^+\sigma_j^-\Big]\,. \tag{C.1.13}$$

Together with Eqs. (1.4.28), (C.1.1), (C.1.12), and (C.1.13), we obtain the (Redfield) master equation for this system.

C.2 Pure Dephasing

The contribution of pure dephasing to the master equation can also be derived using the formalism introduced in Sec. 1.4. In what follows, we illustrate how pure dephasing arises from environmental fluctuations in superconducting circuits.

Environmental fluctuations in electrical circuits lead not only to energy relaxation but also to the so-called pure dephasing, both of which influence quantum coherence. While energy relaxation results in population decay, pure dephasing disrupts phase coherence without affecting populations. These fluctuations, originating from charge noise, flux noise, and TLS defects, cause random shifts in transition frequencies. To model this effect, consider a M-level system, the fluctuations in energy levels can be incorporated into the

doi:10.6342/NTU202503909

Hamiltonian as [89, 90]:

$$H_{\mathrm{S}} + H_{\mathrm{int}}^{(\mathrm{fluc})}(t) = \hbar \sum_{m=1}^{M-1} \Big(\omega_m + \delta\omega_m(t)\Big)\sigma_{mm}, \tag{C.2.1}$$

where ω_m is the frequency of the mth level, and $\delta\omega_m(t)$ is its fluctuation. By Eq. (1.4.15), we identify:

$$S_m^{(S)} = \sigma_{mm}, \tag{C.2.2}$$

$$B_m^{(S)}(t) = \delta\omega_m(t) I_B. \tag{C.2.3}$$

Here, we explicitly include the identity operator on the bath Hilbert space to avoid any confusion. One might wonder why we do not instead assign $S_m^{(S)}(t) = \delta\omega_m(t)\sigma_{mm}$ and $B_m^{(S)} = I_B$. This is because we consistently collect all time-dependent factors into the bath operator, as shown in the decomposition of the interaction Hamiltonian in Eq. (1.4.22) during the derivation process.

According to Eq. (1.4.24)The factor $F_{mn}(\omega)$ now evaluated as

$$\begin{aligned} F_{mn}(\omega; t) &= \int_0^\infty ds\, e^{i\omega s} \delta\omega_m(t)\, \delta\omega_n(t-s) \langle I_B \rangle \\ &= \int_0^\infty ds\, e^{i\omega s} \delta\omega_m(t)\, \delta\omega_n(t-s). \end{aligned} \tag{C.2.4}$$

To account for the statistical nature of the frequency fluctuations, we define the averaged quantity [91]

$$F_{mn}^{\phi}(\omega) \equiv 2\langle\langle F_{mn}(\omega; t)\rangle\rangle = 2\int_0^\infty ds\, e^{i\omega s} \langle\langle \delta\omega_m(t)\, \delta\omega_n(t-s)\rangle\rangle, \tag{C.2.5}$$

where the double brackets $\langle\langle\cdot\rangle\rangle$ denote an average over all possible realizations of noise. Under the assumption that the noise is stationary (i.e., its statistical properties do not change with time), the autocorrelation depends only on the time difference s, and we may

doi:10.6342/NTU202503909

rewrite the above as

$$F^{\phi}_{mn}(\omega) = 2\int_0^{\infty} ds\, e^{i\omega s}\langle\langle \delta\omega_m(s)\, \delta\omega_n(0)\rangle\rangle, \tag{C.2.6}$$

which is independent of the absolute time t. The evolution of the system's density matrix is given by

$$\frac{d\rho(t)}{dt} = -\frac{i}{\hbar}\left[H_S, \rho(t)\right] + \mathcal{L}_{\phi}\left[\rho(t)\right], \tag{C.2.7}$$

where, for clarity, we again omit the superscript and subscript on the density matrix $\rho_S^{(S)}(t)$. The pure dephasing superoperator is

$$\begin{aligned}\mathcal{L}_{\phi}\left[\rho(t)\right] &= \sum_{m,n}\frac{F^{\phi}_{mn}(0)}{2}\left\{\sigma_{nn}\rho(t)\sigma_{mm} - \sigma_{mm}\sigma_{nn}\rho(t)\right\} + h.c. \\ &= \sum_{m,n}\frac{F^{\phi}_{mn}(0)}{2}\Big\{\left[\sigma_{mm}\rho(t), \sigma_{nn}\right] + \left[\sigma_{nn}, \rho(t)\sigma_{mm}\right]\Big\}.\end{aligned} \tag{C.2.8}$$

Note that both ω and ω' take the value zero because σ_{mm} do not induce transitions between energy levels. As a result, we always have $\omega = 0$ in the definition of $F^{\phi}_{mn}(\omega)$, making it a real quantity that we refer to as the pure dephasing rate. Now, if the frequency fluctuations satisfy the relation

$$\delta\omega_m(t) = m\delta\omega_1(t), \tag{C.2.9}$$

where $\delta\omega_1(t)$ is the fluctuation of the transition frequency between the ground and first excited states, then the dephasing superoperator simplifies to

$$\mathcal{L}_{\phi}\left[\rho(t)\right] = \sum_{m,n}\frac{mn\gamma^{\phi}}{2}\Big\{\left[\sigma_{mm}\rho(t), \sigma_{nn}\right] + \left[\sigma_{nn}, \rho(t)\sigma_{mm}\right]\Big\}, \tag{C.2.10}$$

where $\gamma^{\phi} \equiv F^{\phi}_{11}(0)$ denotes the pure dephasing rate associated with the $|0\rangle \leftrightarrow |1\rangle$ transition.

doi:10.6342/NTU202503909

Appendix D

Quantum Regression Theorem

The quantum regression theorem (QRT) provides a method for calculating two-time correlation functions in open quantum systems [92, 93]. It extends the dynamics governed by the master equation, originally derived for the single-time evolution of the system's density matrix, to compute two-time correlations such as $\langle A(t+\tau)B(t)\rangle$, where both A and B are system operators.

Let us begin by calculating the single-time expectation value of an operator A:

$$\langle A(t)\rangle = \mathrm{Tr}[A(t)\rho_{\mathrm{tot}}], \tag{D.0.1}$$

where ρ_{tot} is the total (system + bath) density matrix. We now switch to the Schrodinger picture, where the operator evolves according to $A(t) = U^{\dagger}(t,0)\,A\,U(t,0)$, with $U(t,0)$ being the time-evolution operator from time 0 to t. Therefore,

$$\begin{aligned}
\langle A(t)\rangle &= Tr[A(t)\rho_{\mathrm{tot}}] \\
&= Tr[U^{\dagger}(t,0)AU(t,0)\rho_{\mathrm{tot}}] \\
&= Tr[AU(t,0)\rho_{\mathrm{tot}}U^{\dagger}(t,0)] \\
&= Tr[A\rho_{\mathrm{tot}}(t)] \\
&= Tr_S[A\rho(t)],
\end{aligned} \tag{D.0.2}$$

where $\rho(t)$ is the system density matrix, obtained by tracing out the bath degrees of free-

doi:10.6342/NTU202503909

dom:

$$\rho(t) = Tr_B[\rho_{\text{tot}}(t)] = Tr_B[U(t,0)\rho_{\text{tot}}U^\dagger(t,0)]. \tag{D.0.3}$$

The system density matrix $\rho(t)$ evolves according to the master equation:

$$\frac{d\rho(t)}{dt} = \mathcal{L}(t)\rho(t), \tag{D.0.4}$$

where $\mathcal{L}(t)$ is the Liouvillian superoperator [67] that governs the open-system dynamics. Once $\rho(t)$ is obtained from this equation, the single-time expectation value $\langle A(t)\rangle$ can be directly computed.

Now consider the two-time correlation function $\langle A(t+\tau)B(t)\rangle$, where $A(t)$ and $B(t)$ are arbitrary system operators in the Heisenberg picture:

$$\begin{aligned}
\langle A(t+\tau)B(t)\rangle &= Tr[A(t+\tau)B(t)\rho_{\text{tot}}] \\
&= Tr[U^\dagger(t+\tau,0)AU(t+\tau,0)U^\dagger(t,0)BU(t,0)\rho_{\text{tot}}] \\
&= Tr[U^\dagger(t+\tau,0)AU(t+\tau,t)BU(t,0)\rho_{\text{tot}}] \\
&= Tr[U^\dagger(t,0)U^\dagger(t+\tau,t)AU(t+\tau,t)BU(t,0)\rho_{\text{tot}}] \\
&= Tr[U^\dagger(t+\tau,t)AU(t+\tau,t)BU(t,0)\rho_{\text{tot}}U^\dagger(t,0)] \\
&= Tr[U^\dagger(t+\tau,t)AU(t+\tau,t)B\rho_{\text{tot}}(t)] \\
&= Tr[AU(t+\tau,t)B\rho_{\text{tot}}(t)U^\dagger(t+\tau,t)] \\
&\equiv Tr_S[A\Lambda(t+\tau,t)],
\end{aligned} \tag{D.0.5}$$

where we have used the following properties of the time-evolution operator:

$$U(t_1,t_0) = U(t_1,t_2)U(t_2,t_0) \qquad \text{(associativity)}, \tag{D.0.6}$$

$$U^\dagger(t_0,t_1) = U(t_1,t_0) \qquad \text{(time reversal)}. \tag{D.0.7}$$

doi:10.6342/NTU202503909

The operator $\Lambda(t+\tau,t)$, known as the two-time operator, is defined as

$$\Lambda(t+\tau,t) \equiv Tr_R[U(t+\tau,t)B\rho_{\text{tot}}(t)U^\dagger(t+\tau,t)]. \tag{D.0.8}$$

By comparing Eqs. (D.0.3) and (D.0.8), we find that the two-time operator $\Lambda(t+\tau,t)$ evolves under the same master equation as the system density matrix:

$$\frac{d\Lambda(t+\tau,t)}{d\tau} = \mathcal{L}(\tau)\Lambda(t+\tau,t), \tag{D.0.9}$$

with the initial condition

$$\begin{aligned}\Lambda(t,t) &= Tr_B[U(t,t)B\rho_{SR}(t)U^\dagger(t,t)] \\ &= Tr_B[B\rho_{\text{tot}}(t)] \\ &= B\rho(t)\end{aligned} \tag{D.0.10}$$

In summary, the quantum regression theorem shows that both the single-time density matrix $\rho(t)$ and the two-time operator $\Lambda(t+\tau,t)$ obey the same master equation. This result allows us to compute two-time correlation functions using the same dynamical tools developed for single-time observables.

doi:10.6342/NTU202503909

doi:10.6342/NTU202503909

Appendix E

Numerical Method: Vectorization of Master Equation

In many problems of quantum optics and open quantum systems, we encounter the Markovian master equation of the form:

$$\frac{d\rho(t)}{dt} = \mathcal{L}(t)[\rho(t)], \tag{E.0.1}$$

where $\mathcal{L}(t)\,[\cdots]$ denotes a (possibly time-dependent) superoperator that encapsulates both unitary evolution and bath-induced effects. A typical example is the Redfield equation, which is given in Eq. (1.4.28). We note that every term appearing on the right-hand side of the Redfield equation can be expressed in the form

$$A\rho B, \tag{E.0.2}$$

where A and B are operators. For instance, it contains terms such as

$$S_{\beta,\omega}\rho S^{\dagger}_{\alpha,\omega'}, \tag{E.0.3}$$

which clearly fit the $A\rho B$ structure with $A = S_{\beta,\omega}$ and $B = S^{\dagger}_{\alpha,\omega'}$, or

doi:10.6342/NTU202503909

$$S^{\dagger}_{\alpha,\omega'} S_{\beta,\omega} \rho, \tag{E.0.4}$$

which fits the same structure with $A = S^{\dagger}_{\alpha,\omega'} S_{\beta,\omega}$ and $B = I$.

To solve such equations numerically, it is convenient to vectorize the density matrix and rewrite the operator evolution in matrix form. Vectorization is a standard linear algebra technique where an $n \times n$ operator (e.g., the density matrix ρ) is flattened into an $n^2 \times 1$ column vector, denoted by $\rho_c = \text{vec}(\rho)$. Under this transformation, operator expressions such as $A\rho B$ can be rewritten using the Kronecker product identity [94]:

$$A\rho B = (B^T \otimes A)\, \rho_c, \tag{E.0.5}$$

where $\otimes$ denotes the Kronecker product. Explicitly, if the original matrix ρ is written as

$$\rho = \begin{bmatrix} \rho_{11} & \rho_{12} & \cdots & \rho_{1n} \\ \rho_{21} & \rho_{22} & \cdots & \rho_{2n} \\ \vdots & \vdots & \ddots & \vdots \\ \rho_{n1} & \rho_{n2} & \cdots & \rho_{nn} \end{bmatrix}, \quad \text{then} \quad \rho_c = \begin{bmatrix} \rho_{11} \\ \rho_{21} \\ \vdots \\ \rho_{n1} \\ \rho_{12} \\ \vdots \\ \rho_{nn} \end{bmatrix}.$$

This allows the master equation, Eq. (E.0.1), to be cast as a matrix differential equation:

$$\frac{d\rho_c}{dt} = \mathcal{L}_M(t)\, \rho_c, \tag{E.0.6}$$

where $\mathcal{L}_M(t)$ is now understood as a $n^2 \times n^2$ matrix acting on the vectorized state ρ_c.

Once vectorized, the operator evolution problem reduces to the standard numerical integration of a system of first-order ordinary differential equations (ODEs). The formal

doi:10.6342/NTU202503909

solution depends on how $\mathcal{L}_M(t)$ varies with time. We distinguish three typical cases:

1. **Time-independent**

   When $\mathcal{L}_M(t)$=$\mathcal{L}_M$ is constant in time, the equation becomes:

   $$\frac{d\rho_c}{dt} = \mathcal{L}_M \rho_c, \tag{E.0.7}$$

   whose solution is simply

   $$\rho_c(t) = e^{\mathcal{L}_M t}\rho_c(0). \tag{E.0.8}$$

   An important advantage is that, numerically, one can bypass step-by-step time integration and directly evaluate the solution at any desired time using the matrix exponential.

2. **Time-dependent and mutually commuting**

   If $\mathcal{L}_M(t)$ depends on time but satisfies $[\mathcal{L}_M(t_1), \mathcal{L}_M(t_2)] = 0$ for all t_1, t_2, the solution can be written as:

   $$\rho^c(t) = \exp\left(\int_0^t \mathcal{L}_M(s)\, ds\right)\rho^c(0). \tag{E.0.9}$$

   In this case, we first compute the time integral of $\mathcal{L}_M(s)$, and then take the matrix exponential of the result.

3. **Time-dependent and non-commuting**

   In the most general case, where $\mathcal{L}_M(t)$ does not commute at different times, the solution must be written as a time-ordered exponential:

   $$\rho^c(t) = \mathcal{T}\exp\left(\int_0^t \mathcal{L}_M(s)\, ds\right)\rho^c(0). \tag{E.0.10}$$

   Here $\mathcal{T}$ denotes the time-ordering operator, which ensures that the matrix exponentiation accounts for the non-commuting property of $\mathcal{L}_M(t)$ at different times.

doi:10.6342/NTU202503909

doi:10.6342/NTU202503909

Appendix F

Tranforming the Master Equation to a Rotating Frame

In the laboratory frame, master equations often contain explicitly time-dependent oscillatory terms, which significantly complicates both analytical and numerical treatment of the system dynamics. It is often useful to transform the system's dynamics into a rotating frame. This is done to eliminate fast oscillations or time dependencies in the Hamiltonian or dissipator, thereby simplifying the structure of the master equation. The rotating frame transformation is performed via a time-dependent unitary operator $U(t)$, such that the density matrix in the rotating frame is given by:

$$\tilde{\rho}(t) = U(t)\rho(t)U^{\dagger}(t). \tag{F.0.1}$$

Throughout this section, we adopt the convention that quantities with a tilde (e.g., $\tilde{\rho}(t)$ or $\tilde{H}(t)$) refer to the rotating frame, while those without a tilde are defined in the laboratory frame. Taking time derivative to Eq. (F.0.1) leads:

$$\frac{d\tilde{\rho}(t)}{dt} = \left(\frac{dU(t)}{dt}\right)\rho(t)U^{\dagger}(t) + U(t)\rho(t)\left(\frac{dU^{\dagger}(t)}{dt}\right) + U(t)\left(\frac{d\rho(t)}{dt}\right)U^{\dagger}(t). \tag{F.0.2}$$

doi:10.6342/NTU202503909

Inserting the identity $I = U^\dagger U = UU^\dagger$ into the first two terms allows us to rewrite them as:

$$\begin{aligned}\frac{dU(t)}{dt}\rho(t)U^\dagger(t) + U(t)\rho(t)\frac{dU^\dagger(t)}{dt} &= \frac{dU(t)}{dt}U^\dagger(t)\tilde{\rho}(t) + \tilde{\rho}(t)U(t)\frac{dU^\dagger(t)}{dt} \\ &= -U(t)\frac{dU^\dagger(t)}{dt}\tilde{\rho}(t) + \tilde{\rho}(t)U(t)\frac{dU^\dagger(t)}{dt} \\ &= -\left[U(t)\frac{dU^\dagger(t)}{dt}, \tilde{\rho}(t)\right],\end{aligned} \tag{F.0.3}$$

where we have used the identity $\frac{dU}{dt}U^\dagger + U\frac{dU^\dagger}{dt} = 0$, which follows from the unitarity of U.

$$0 = \frac{d}{dt}\left(U(t)U^\dagger(t)\right) = \frac{dU(t)}{dt}U^\dagger(t) + U(t)\frac{dU^\dagger(t)}{dt}. \tag{F.0.4}$$

We now turn to the third term, which involves the time derivative of the density matrix in the laboratory frame. Assuming the density matrix satisfies the Redfield master equation in the laboratory frame, Eq. (1.4.28):

$$\frac{d\rho(t)}{dt} = -\frac{i}{\hbar}\left[H(t), \rho(t)\right] + \mathcal{L}_L\left[\rho(t)\right] + \mathcal{L}_D\left[\rho(t)\right], \tag{F.0.5}$$

the third term in Eq. (F.0.2) becomes:

$$\begin{aligned}U(t)\frac{d\rho(t)}{dt}U^\dagger(t) &= -\frac{i}{\hbar}U(t)\left[H(t), \rho(t)\right]U^\dagger(t) + U(t)\mathcal{L}_L\left[\rho(t)\right]U^\dagger(t) + U(t)\mathcal{L}_D\left[\rho(t)\right]U^\dagger(t) \\ &\equiv -\frac{i}{\hbar}\left[U(t)H(t)U^\dagger(t), \tilde{\rho}(t)\right] + \tilde{\mathcal{L}}_L\left[\tilde{\rho}(t)\right] + \tilde{\mathcal{L}}_D\left[\tilde{\rho}(t)\right].\end{aligned} \tag{F.0.6}$$

Here, $H(t)$ is understood to include both the free and driving terms in the laboratory frame, and is therefore time-dependent. The transformed superoperators are defined as:

doi:10.6342/NTU202503909

$$\tilde{\mathcal{L}}_L\left[\tilde{\rho}(t)\right] \equiv U(t)\left(\mathcal{L}_L\left[\rho(t)\right]\right)U^\dagger(t), \tag{F.0.7}$$

$$\tilde{\mathcal{L}}_D\left[\tilde{\rho}(t)\right] \equiv U(t)\left(\mathcal{L}_D\left[\rho(t)\right]\right)U^\dagger(t). \tag{F.0.8}$$

Substituting Eq. (F.0.3) and Eq. (F.0.6) into Eq. (F.0.2), we arrive at the Redfield master equation in the rotating frame:

$$\frac{d\tilde{\rho}(t)}{dt} = -\frac{i}{\hbar}\left[\tilde{H}(t), \tilde{\rho}(t)\right] + \tilde{\mathcal{L}}_L\left[\tilde{\rho}(t)\right] + \tilde{\mathcal{L}}_D\left[\tilde{\rho}(t)\right], \tag{F.0.9}$$

with the effective Hamiltonian in the rotating frame defined as:

$$\tilde{H}(t) = U(t)H(t)U^\dagger(t) - i\hbar U(t)\frac{dU^\dagger(t)}{dt}. \tag{F.0.10}$$

F.1 Example: Application to the Main-Text Master Equation

We now apply a rotating-frame transformation to the main-text master equation, Eq. (2.1.15), moving into a frame rotating at frequency ω_s as an example. Comparing Eq. (2.1.15) with Eq. (F.0.5), the Hamiltonian in the laboratory frame is given by

$$\begin{aligned} H(t) = &\sum_{m=0}^{M-1} \hbar\omega_m \sigma_{mm} \\ &+ \sum_{m=0}^{M-1} \hbar\frac{\sqrt{m}\Omega_1}{2}\left(\sigma_{m,m-1}e^{-i\omega_{d1}t} + \sigma_{m-1,m}e^{i\omega_{d1}t}\right) \\ &+ \sum_{m=0}^{M-1} \hbar\frac{\sqrt{m}\Omega_2}{2}\left(\sigma_{m,m-1}e^{-i\omega_{d2}t} + \sigma_{m-1,m}e^{i\omega_{d2}t}\right). \end{aligned} \tag{F.1.1}$$

doi:10.6342/NTU202503909

Moreover, there is no Lamb shift contribution (i.e., $\mathcal{L}_L[\rho(t)] = 0$), and the dissipation term is

$$\begin{aligned}\mathcal{L}_D[\rho(t)] = &\sum_{m,n=1}^{M-1} \frac{\sqrt{mn}\gamma_{m,m-1}}{2}([\sigma_{m-1,m}\rho, \sigma_{n,n-1}] + [\sigma_{n-1,n}, \rho\sigma_{m,m-1}]) \\ &+ \sum_{m,n=1}^{M-1} \frac{mn\gamma^{\phi}}{2}([\sigma_{mm}\rho, \sigma_{nn}] + [\sigma_{nn}, \rho\sigma_{mm}]).\end{aligned} \tag{F.1.2}$$

To perform the transformation, we define the rotating-frame unitary operator as

$$U(t) = \exp\left(-i\sum_{m=0}^{M-1} m\omega_s t\sigma_{mm}\right) = \sum_{m=0}^{M-1} e^{-im\omega_s t}\sigma_{mm}. \tag{F.1.3}$$

The first term in Eq. (F.0.10) becomes

$$\begin{aligned}U(t)H(t)U^{\dagger}(t) = &\sum_{m=0}^{M-1} \hbar\omega_m\sigma_{mm} \\ &+ \sum_{m=0}^{M-1} \hbar\frac{\sqrt{m}\Omega_1}{2}\left(\sigma_{m,m-1}e^{-i(\omega_{d1}-\omega_s)t} + \sigma_{m-1,m}e^{i(\omega_{d1}-\omega_s)t}\right) \\ &+ \sum_{m=0}^{M-1} \hbar\frac{\sqrt{m}\Omega_2}{2}\left(\sigma_{m,m-1}e^{-i(\omega_{d2}-\omega_s)t} + \sigma_{m-1,m}e^{i(\omega_{d2}-\omega_s)t}\right).\end{aligned} \tag{F.1.4}$$

The second term of Eq. (F.0.10), is evaluated as

$$i\hbar U(t)\frac{dU^{\dagger}(t)}{dt} = -\sum_{m=0}^{M-1} \hbar m\omega_s\sigma_{mm}. \tag{F.1.5}$$

Therefore, the effective Hamiltonian in the rotating frame reads

doi:10.6342/NTU202503909

$$\begin{aligned}\tilde{H}(t) = &\sum_{m=0}^{M-1} \hbar\left(\omega_m - m\omega_s\right)\sigma_{mm} \\ &+ \sum_{m=0}^{M-1} \hbar\frac{\sqrt{m}\Omega_1}{2}\left(\sigma_{m,m-1}e^{-i(\omega_{d1}-\omega_s)t} + \sigma_{m-1,m}e^{i(\omega_{d1}-\omega_s)t}\right) \\ &+ \sum_{m=0}^{M-1} \hbar\frac{\sqrt{m}\Omega_2}{2}\left(\sigma_{m,m-1}e^{-i(\omega_{d2}-\omega_s)t} + \sigma_{m-1,m}e^{i(\omega_{d2}-\omega_s)t}\right).\end{aligned} \tag{F.1.6}$$

For the dissipation term, we apply the transformation in Eq. (F.0.8), using the identity

$$U(t)\sigma_{mn}U^{\dagger}(t) = e^{-i(m-n)\omega_s t}\sigma_{mn}. \tag{F.1.7}$$

Notably, in each commutator, the phase factor introduced by one operator is exactly canceled by its counterpart. As a result, the form of the dissipation term remains unchanged in the rotating frame:

$$\tilde{\mathcal{L}}_D\left[\tilde{\rho}(t)\right] = \mathcal{L}_D\left[\rho(t)\right]. \tag{F.1.8}$$

So, together with Eq. (F.0.9), (F.1.6), (F.1.8) and (F.1.2), we obtain the main-text master equation in the rotating frame with respect to frequency ω_s:

doi:10.6342/NTU202503909

$$
\begin{aligned}
\frac{d\tilde{\rho}}{dt} &= i\sum_{m=0}^{M-1}(m\omega_s-\omega_m)\left[\sigma_{mm},\tilde{\rho}\right] \\
&+ i\sum_{m=1}^{M-1}\frac{\sqrt{m}\Omega_1}{2}\left[\sigma_{m,m-1}e^{-i(\omega_{d1}-\omega_s)t}+\sigma_{m-1,m}e^{i(\omega_{d1}-\omega_s)t},\tilde{\rho}\right] \\
&+ i\sum_{m=1}^{M-1}\frac{\sqrt{m}\Omega_2}{2}\left[\sigma_{m,m-1}e^{-i(\omega_{d2}-\omega_s)t}+\sigma_{m-1,m}e^{i(\omega_{d2}-\omega_s)t},\tilde{\rho}\right] \\
&+ \sum_{m,n=1}^{M-1}\frac{\sqrt{mn}\gamma_{m,m-1}}{2}\left(\left[\sigma_{m-1,m}\tilde{\rho},\sigma_{n,n-1}\right]+\left[\sigma_{n-1,n},\tilde{\rho}\sigma_{m,m-1}\right]\right) \\
&+ \sum_{m,n=1}^{M-1}\frac{mn\gamma^{\phi}}{2}\left(\left[\sigma_{mm}\tilde{\rho},\sigma_{nn}\right]+\left[\sigma_{nn},\tilde{\rho}\sigma_{mm}\right]\right).
\end{aligned}
\tag{F.1.9}
$$

doi:10.6342/NTU202503909

Appendix G

Fitting Formula for Experimental Spectra

In the experiment, the signal is measured using a pump-on and pump-off method [95], and the results are presented as the power ratio in decibels (dB). To relate these measurements with theoretical quantities, we first express the measured power difference x in dB

$$x = 10 \log_{10} \left(\frac{P_{\text{on}}}{P_{\text{off}}} \right), \tag{G.0.1}$$

where P_{on} and P_{off} are the measured powers with the pump and without the pump (background noise), respectively. Since the total measured power includes both the background and pump-induced signal, we write $P_{\text{on}} = P_{\text{off}} + P_{\text{signal}}$, leading to

$$\frac{P_{\text{on}}}{P_{\text{off}}} = 1 + \frac{P_{\text{signal}}}{P_{\text{off}}}, \tag{G.0.2}$$

with P_{signal} denoting the signal power induced by the bichromatic drive.

To connect this experimental signal with theory, we assume that P_{signal} is proportional to the theoretical emission spectrum. The total theoretical spectrum consists of incoherent and coherent parts, $S(\omega) = \bar{S}_{co}(\omega) + S_{inco}(\omega)$, which leads to the following fitting

doi:10.6342/NTU202503909

function:

$$F(\omega) = 10\log\left(1 + \left[\bar{S}_{co}(\omega) + S_{inco}(\omega)\right]\frac{\Delta\omega_{\text{RBW}}}{P_{\text{off}}}\right), \tag{G.0.3}$$

where $\Delta\omega_{\text{RBW}} = 910\,\text{kHz}$ is the resolution bandwidth determined by the spectrum analyzer, and P_{off} is treated as a fitting parameter.

doi:10.6342/NTU202503909

Appendix H

Summary of Fitting Parameters for Theoretical Models

This appendix provides the fitted parameters used in the theoretical spectra presented in Chapter 3.

doi:10.6342/NTU202503909

P_1 (dBm) \ Peak index p	Fitted value of peak width (MHz)							
	-7	-5	-3	-1	$+1$	$+3$	$+5$
-12	-	-	-	0.0918	0.1104	0.1513	-
-11	-	-	-	0.1076	0.1187	0.2525	0.1951
-10	-	-	-	0.1103	0.1170	0.3066	0.2007
-9	-	-	-	0.1129	0.1196	0.3264	0.2100
-8	-	-	-	0.0874	0.1123	0.1810	0.2028
-7	-	-	-	0.1115	0.1187	0.3608	0.2013
-6	-	0.0204	0.1341	0.0987	0.1152	0.2385	0.2007
-5	-	0.0433	0.2248	0.1171	0.1116	0.3076	0.3466
-4	-	0.0662	0.1560	0.0874	0.1181	0.2591	0.4924
-3	-	0.0662	0.1424	0.0920	0.1184	0.2728	0.5356
-2	-	0.0856	0.1521	0.0968	0.1150	0.3616	0.6203
-1	0.1941	0.1710	0.1152	0.0993	0.1185	0.3360	0.6203
0	0.5142	0.3246	0.1737	0.0993	0.0906	0.1964	0.7425
1	0.5056	0.2786	0.1950	0.0924	0.0727	0.0987	-
2	0.1462	0.1716	0.1418	0.0883	0.0556	0.1835	-
3	0.2998	0.1216	0.1287	0.0764	0.0469	-	-

η_1	η_2	P_{off} (W)
2.54	2.78	8.11×10^{-18}

Table H.1: Fitted peak widths (MHz) of sidebands in Fig. 3.3. Each entry represents the fitted linewidth of a sideband peak labeled by index p, evaluated at a specific input power P_1. The parameters used are $\omega_{d1}/2\pi = 4.82\,\text{GHz}$, $\omega_{d2}/2\pi = 4.825\,\text{GHz}$, and $P_2 = -1\,\text{dBm}$. Also shown are the fitted scaling factors η_1, η_2 for the two drives, and the background noise offset power P_{off}.

doi:10.6342/NTU202503909

Fitted value of peak width (MHz)											
$\frac{\Delta}{2\pi}$ (dBm)	Peak index p	-7	-5	-3	-1	$+1$	$+3$	$+5$	$+7$
	2	0.5466	0.3322	0.2752	0.0358	0.0354	0.0295	0.3323	0.9423
	4	0.4770	0.4409	0.3362	0.0447	0.0420	0.3326	0.3724	0.6364
	6	0.4048	0.3087	0.2564	0.0468	0.0383	0.2684	0.2991	0.4920
	8	0.8423	0.3877	0.3520	0.0473	0.0364	0.2658	0.4908	0.3237
	10	1.0895	0.2806	0.2965	0.0477	0.0335	0.2172	0.3211	0.4497
	12	1.0835	0.3594	0.2735	0.0482	0.0313	0.2003	0.2760	0.7451
	14	0.8023	0.4170	0.2235	0.0478	0.0291	0.1739	0.4183	0.5232
	16	0.5282	0.3770	0.2516	0.0473	0.0274	0.1739	0.4439	0.6442
	18	0.5950	0.3694	0.2321	0.0473	0.0255	0.1494	0.2501	0.3810
	20	0.3700	0.416	0.2513	0.0459	0.0240	0.1634	0.2501	0.3810
	22	-	0.3435	0.2624	0.0453	0.0226	0.2195	0.2521	-
	24	-	0.2864	0.3074	0.0458	0.0208	0.1849	0.2728	-
	26	-	0.2718	0.3512	0.0450	0.0201	0.2249	0.2225	-
	28	-	0.2950	0.3230	0.0431	0.0202	0.2392	0.1785	-
	30	-	-	0.2923	0.0412	0.0192	0.2186	-	-
	32	-	-	0.2708	0.0417	0.0173	0.1526	-	-

η_1	η_2	P_{off} (W)
2.63	2.69	8.11×10^{-18}

Table H.2: Fitted peak widths (MHz) of sidebands in Fig. 3.6. Each entry represents the fitted linewidth of a sideband peak labeled by index p, evaluated at a specific detuning $\Delta/2\pi$. The parameters used are $\omega_{d1/d2}/2\pi = 4.82\,\text{GHz} \pm \Delta/2\pi$ and $P_1 = P_2 = 2\,\text{dBm}$. Also shown are the fitted scaling factors η_1, η_2 for the two drives, and the background noise offset power P_{off}.

doi:10.6342/NTU202503909

doi:10.6342/NTU202503909

Bibliography

[1] A. F. Kockum and F. Nori, *Quantum Bits with Josephson Junctions*, pp. 703–741. Cham: Springer International Publishing, 2019.

[2] K.-T. Lin, T. Hsu, C.-Y. Lee, I.-C. Hoi, and G.-D. Lin, "Scalable collective lamb shift of a 1d superconducting qubit array in front of a mirror," *Scientific Reports*, vol. 9, Dec. 2019.

[3] D. E. Chang, V. Vuletić, and M. D. Lukin, "Quantum nonlinear optics — photon by photon," *Nature Photonics*, vol. 8, pp. 685–694, Aug. 2014.

[4] Y. Cai, J. Feng, H. Wang, G. Ferrini, X. Xu, J. Jing, and N. Treps, "Quantum-network generation based on four-wave mixing," *Phys. Rev. A*, vol. 91, p. 013843, Jan 2015.

[5] A. Dutt, A. Mohanty, A. L. Gaeta, and M. Lipson, "Nonlinear and quantum photonics using integrated optical materials," *Nature Reviews Materials*, vol. 9, pp. 321–346, May 2024.

[6] J. Zhong, Rituraj, F. Dinc, and S. Fan, "Detecting the relative phase between different frequency components of a photon using a three-level Λ atom coupled to a waveguide," *Phys. Rev. A*, vol. 107, p. L051702, May 2023.

[7] H. Zhang and H. Wang, "Entanglement concentration of microwave photons based on the kerr effect in circuit qed," *Phys. Rev. A*, vol. 95, p. 052314, May 2017.

[8] J. Guo, Q. He, and M. Fadel, "Quantum metrology with a squeezed kerr oscillator," *Phys. Rev. A*, vol. 109, p. 052604, May 2024.

doi:10.6342/NTU202503909

[9] M. Ma, Q. Zhu, and F.-F. Du, "Kerr-Effect-Based High-Dimensional Entanglement Generation for Qudit Systems," *Adv. Quantum Technol.*, vol. 8, no. 5, p. 2500010, 2025.

[10] X. Qiao, Z. Yao, and H. Yang, "Strongly enhanced photon-pair blockade with three-wave mixing by quantum interference," *Phys. Rev. A*, vol. 110, p. 053702, Nov 2024.

[11] M. Chen, J. Tang, L. Tang, H. Wu, and K. Xia, "Photon blockade and single-photon generation with multiple quantum emitters," *Phys. Rev. Res.*, vol. 4, p. 033083, Jul 2022.

[12] J. Tang, L. Tang, H. Wu, Y. Wu, H. Sun, H. Zhang, T. Li, Y. Lu, M. Xiao, and K. Xia, "Towards on-demand heralded single-photon sources via photon blockade," *Phys. Rev. Appl.*, vol. 15, p. 064020, Jun 2021.

[13] L. Chang, S. Liu, and J. E. Bowers, "Integrated optical frequency comb technologies," *Nature Photonics*, vol. 16, pp. 95–108, Feb. 2022.

[14] J. Rivera Hernández, F. Lingua, S. W. Jolin, and D. B. Haviland, "Control of multimodal scattering in a microwave frequency comb," *APL Quantum*, vol. 1, no. 3, 2024.

[15] S. W. Jolin, G. Andersson, J. C. R. Hernández, I. Strandberg, F. Quijandría, J. Aumentado, R. Borgani, M. O. Tholén, and D. B. Haviland, "Multipartite entanglement in a microwave frequency comb," *Phys. Rev. Lett.*, vol. 130, p. 120601, Mar 2023.

[16] A. V. Venkatramani, *Quantum nonlinear optics: controlling few-photon interactions*. PhD thesis, Harvard University, 2021.

[17] C. Joshi, A. Farsi, A. Dutt, B. Y. Kim, X. Ji, Y. Zhao, A. M. Bishop, M. Lipson, and A. L. Gaeta, "Frequency-domain quantum interference with correlated photons from an integrated microresonator," *Phys. Rev. Lett.*, vol. 124, p. 143601, Apr 2020.

[18] A. F. Kockum, V. Macrì, L. Garziano, S. Savasta, and F. Nori, "Frequency conversion in ultrastrong cavity qed," *Scientific Reports*, vol. 7, July 2017.

doi:10.6342/NTU202503909

[19] Y. Zhang, F. Wen, and M. Xiao, *Quantum Control of Multi-Wave Mixing*. Wiley-VCH, July 2013.

[20] R. W. Boyd, "Chapter 3 - quantum-mechanical theory of the nonlinear optical susceptibility," in *Nonlinear Optics (Third Edition)* (R. W. Boyd, ed.), pp. 135–206, Burlington: Academic Press, third edition ed., 2008.

[21] J. Koch, T. M. Yu, J. Gambetta, A. A. Houck, D. I. Schuster, J. Majer, A. Blais, M. H. Devoret, S. M. Girvin, and R. J. Schoelkopf, "Charge-insensitive qubit design derived from the cooper pair box," *Phys. Rev. A*, vol. 76, p. 042319, Oct 2007.

[22] M. K. Tey, Z. Chen, S. A. Aljunid, B. Chng, F. Huber, G. Maslennikov, and C. Kurtsiefer, "Strong interaction between light and a single trapped atom without the need for a cavity," *Nature Physics*, vol. 4, pp. 924–927, Oct. 2008.

[23] Y. Wang, J. c. v. Minář, L. Sheridan, and V. Scarani, "Efficient excitation of a two-level atom by a single photon in a propagating mode," *Phys. Rev. A*, vol. 83, p. 063842, Jun 2011.

[24] I.-C. Hoi, C. M. Wilson, G. Johansson, T. Palomaki, B. Peropadre, and P. Delsing, "Demonstration of a single-photon router in the microwave regime," *Phys. Rev. Lett.*, vol. 107, p. 073601, Aug 2011.

[25] O. Astafiev, A. M. Zagoskin, A. Abdumalikov Jr, Y. A. Pashkin, T. Yamamoto, K. Inomata, Y. Nakamura, and J. S. Tsai, "Resonance fluorescence of a single artificial atom," *Science*, vol. 327, no. 5967, pp. 840–843, 2010.

[26] A. Wallraff, D. I. Schuster, A. Blais, L. Frunzio, R.-S. Huang, J. Majer, S. Kumar, S. M. Girvin, and R. J. Schoelkopf, "Strong coupling of a single photon to a superconducting qubit using circuit quantum electrodynamics," *Nature*, vol. 431, pp. 162–167, Sept. 2004.

[27] A. Abdumalikov Jr, O. Astafiev, Y. A. Pashkin, Y. Nakamura, and J. Tsai, "Dynamics of coherent and incoherent emission from an artificial atom in a 1d space," *Physical review letters*, vol. 107, no. 4, p. 043604, 2011.

doi:10.6342/NTU202503909

[28] D. Toyli, A. Eddins, S. Boutin, S. Puri, D. Hover, V. Bolkhovsky, W. Oliver, A. Blais, and I. Siddiqi, "Resonance fluorescence from an artificial atom in squeezed vacuum," *Physical Review X*, vol. 6, no. 3, p. 031004, 2016.

[29] K.-T. Lin, T. Hsu, F. Aziz, Y.-C. Lin, P.-Y. Wen, I.-C. Hoi, and G.-D. Lin, "Single-atom amplification assisted by multiple sideband interference in waveguide qed systems," *New Journal of Physics*, 2025.

[30] Q. Miao and G. S. Agarwal, "Transparency, nonclassicality, and nonreciprocity in chiral waveguide quantum electrodynamics," *Phys. Rev. Res.*, vol. 7, p. 013138, Feb 2025.

[31] Y.-L. L. Fang and H. U. Baranger, "Multiple emitters in a waveguide: Nonreciprocity and correlated photons at perfect elastic transmission," *Phys. Rev. A*, vol. 96, p. 013842, Jul 2017.

[32] L. Du, Y.-T. Chen, and Y. Li, "Nonreciprocal frequency conversion with chiral Λ-type atoms," *Phys. Rev. Res.*, vol. 3, p. 043226, Dec 2021.

[33] P. Y. Wen, K.-T. Lin, A. F. Kockum, B. Suri, H. Ian, J. C. Chen, S. Y. Mao, C. C. Chiu, P. Delsing, F. Nori, G.-D. Lin, and I.-C. Hoi, "Large collective lamb shift of two distant superconducting artificial atoms," *Phys. Rev. Lett.*, vol. 123, p. 233602, Dec 2019.

[34] J. A. Mlynek, A. A. Abdumalikov, C. Eichler, and A. Wallraff, "Observation of dicke superradiance for two artificial atoms in a cavity with high decay rate," *Nature Communications*, vol. 5, Nov. 2014.

[35] K. Lalumière, B. C. Sanders, A. F. van Loo, A. Fedorov, A. Wallraff, and A. Blais, "Input-output theory for waveguide qed with an ensemble of inhomogeneous atoms," *Phys. Rev. A*, vol. 88, p. 043806, Oct 2013.

[36] A. Albrecht, L. Henriet, A. Asenjo-Garcia, P. B. Dieterle, O. Painter, and D. E. Chang, "Subradiant states of quantum bits coupled to a one-dimensional waveguide," *New Journal of Physics*, vol. 21, no. 2, p. 025003, 2019.

doi:10.6342/NTU202503909

[37] T. Hönigl-Decrinis, I. V. Antonov, R. Shaikhaidarov, V. N. Antonov, A. Y. Dmitriev, and O. V. Astafiev, "Mixing of coherent waves in a single three-level artificial atom," *Phys. Rev. A*, vol. 98, p. 041801, Oct 2018.

[38] C. Wu, H. R. Hamedi, C. Kong, W. Li, and Z. Wang, "Vortex modulation via four-wave mixing in superconducting artificial atoms," *Chaos, Solitons & Fractals*, vol. 196, p. 116293, 2025.

[39] H.-C. Li, G.-Q. Ge, and H.-Y. Zhang, "Coexistence of three-wave, four-wave, and five-wave mixing processes in a superconducting artificial atom," *Opt. Lett.*, vol. 40, pp. 1133–1136, Mar 2015.

[40] A. Y. Dmitriev, R. Shaikhaidarov, T. Hönigl-Decrinis, S. E. de Graaf, V. N. Antonov, and O. V. Astafiev, "Probing photon statistics of coherent states by continuous wave mixing on a two-level system," *Phys. Rev. A*, vol. 100, p. 013808, Jul 2019.

[41] A. Y. Dmitriev, R. Shaikhaidarov, V. N. Antonov, T. Hönigl-Decrinis, and O. V. Astafiev, "Quantum wave mixing and visualisation of coherent and superposed photonic states in a waveguide," *Nature Communications*, vol. 8, Nov. 2017.

[42] W. V. Pogosov, A. Y. Dmitriev, and O. V. Astafiev, "Effects of photon statistics in wave mixing on a single qubit," *Phys. Rev. A*, vol. 104, p. 023703, Aug 2021.

[43] Y.-x. Liu, H.-C. Sun, Z. H. Peng, A. Miranowicz, J. S. Tsai, and F. Nori, "Controllable microwave three-wave mixing via a single three-level superconducting quantum circuit," *Scientific Reports*, vol. 4, Dec. 2014.

[44] A. V. Vasenin, A. Y. Dmitriev, S. V. Kadyrmetov, A. N. Bolgar, and O. V. Astafiev, "Dynamics of multiphoton scattering in a two-level mixer," *Phys. Rev. A*, vol. 106, p. L041701, Oct 2022.

[45] S. A. Gunin, A. Y. Dmitriev, A. V. Vasenin, K. S. Tikhonov, G. P. Fedorov, and O. V. Astafiev, "Quantum and classical field scattered on a single two-level system," *Phys. Rev. A*, vol. 108, p. 033723, Sep 2023.

doi:10.6342/NTU202503909

[46] P. Yanes-Thomas, R. Gutiérrez-Jáuregui, P. Barberis-Blostein, D. Sahagún-Sánchez, R. Jáuregui, and A. Kunold, "Collective coupling of driven multilevel atoms and its effect on four-wave mixing," *Phys. Rev. Res.*, vol. 7, p. 013028, Jan 2025.

[47] T. E. Roth, R. Ma, and W. C. Chew, "The transmon qubit for electromagnetics engineers: An introduction," *IEEE Antennas and Propagation Magazine*, vol. 65, no. 2, pp. 8–20, 2023.

[48] B. Josephson, "Possible new effects in superconductive tunnelling," *Physics Letters*, vol. 1, no. 7, pp. 251–253, 1962.

[49] A. Blais, A. L. Grimsmo, S. M. Girvin, and A. Wallraff, "Circuit quantum electrodynamics," *Rev. Mod. Phys.*, vol. 93, p. 025005, May 2021.

[50] J. Q. You and F. Nori, "Atomic physics and quantum optics using superconducting circuits," *Nature*, vol. 474, pp. 589–597, June 2011.

[51] L. N. Cooper, "Bound electron pairs in a degenerate fermi gas," *Phys. Rev.*, vol. 104, pp. 1189–1190, Nov 1956.

[52] M. Tinkham, *Introduction to superconductivity*. Mineola, N.Y: Dover Publications, 2nd ed. ed., 1996.

[53] J. J. García Ripoll, *Superconductivity*, pp. 19–33. Cambridge University Press, 2022.

[54] M. Devoret, *Quantum fluctuations in electrical circuits*. Edition de Physique, Jan. 1995.

[55] B. Yurke and J. S. Denker, "Quantum network theory," *Phys. Rev. A*, vol. 29, pp. 1419–1437, Mar 1984.

[56] J. J. García Ripoll, *Quantum Circuit Theory*, pp. 34–62. Cambridge University Press, 2022.

[57] J. Lisenfeld, A. Bilmes, A. Megrant, R. Barends, J. Kelly, P. Klimov, G. Weiss, J. M. Martinis, and A. V. Ustinov, "Electric field spectroscopy of material defects in transmon qubits," *npj Quantum Information*, vol. 5, Nov. 2019.

doi:10.6342/NTU202503909

[58] J. J. García Ripoll, *Superconducting Qubits*, p. 106 – 155. Cambridge University Press, 2022.

[59] M. H. Devoret and R. J. Schoelkopf, "Superconducting circuits for quantum information: An outlook," *Science*, vol. 339, no. 6124, pp. 1169–1174, 2013.

[60] R. W. Boyd, "Chapter 1 - the nonlinear optical susceptibility," in *Nonlinear Optics (Third Edition)* (R. W. Boyd, ed.), pp. 1–67, Burlington: Academic Press, third edition ed., 2008.

[61] Y.-R. Shen, *Principles of Nonlinear Optics*. New York: John Wiley & Sons, 1984. Introduction.

[62] P. D. Drummond and M. Hillery, *Classical nonlinear optics*, p. 4 – 36. Cambridge University Press, 2014.

[63] F. J. Dyson, "The s matrix in quantum electrodynamics," *Phys. Rev.*, vol. 75, pp. 1736–1755, Jun 1949.

[64] S. Weinberg, *General scattering theory*, p. 282 – 324. Cambridge University Press, 2015.

[65] D. Manzano, "A short introduction to the lindblad master equation," *AIP Advances*, vol. 10, p. 025106, 02 2020.

[66] H.-P. Breuer and F. Petruccione, "Quantum master equations," in *The Theory of Open Quantum Systems*, pp. 109–218, Oxford University Press, 01 2007.

[67] H. J. Carmichael, *Dissipation in Quantum Mechanics: The Master Equation Approach*, pp. 1–28. Berlin, Heidelberg: Springer Berlin Heidelberg, 1999.

[68] K.-T. Lin, T. Hsu, F. Aziz, Y.-C. Lin, P.-Y. Wen, I.-C. Hoi, and G.-D. Lin, "Single-atom amplification assisted by multiple sideband interference in 1d waveguide qed systems," *arXiv preprint*, 2023.

doi:10.6342/NTU202503909

[69] M. O. Scully and M. S. Zubairy, *Quantum theory of radiation*, p. 1–45. Cambridge University Press, 1997.

[70] H. J. Carmichael, *Two-Level Atoms and Spontaneous Emission*, pp. 29–74. Berlin, Heidelberg: Springer Berlin Heidelberg, 1999.

[71] D. M. Pozar, "Microwave network analysis," in *Microwave Engineering*, ch. 4, pp. 165–227, Wiley, 4 ed., 2012.

[72] B. Peropadre, J. Lindkvist, I.-C. Hoi, C. M. Wilson, J. J. Garcia-Ripoll, P. Delsing, and G. Johansson, "Scattering of coherent states on a single artificial atom," *New Journal of Physics*, vol. 15, p. 035009, mar 2013.

[73] B. R. Mollow, "Power spectrum of light scattered by two-level systems," *Phys. Rev.*, vol. 188, pp. 1969–1975, Dec 1969.

[74] D. Walls and G. J. Milburn, *Interaction of Radiation with Atoms*, pp. 197–211. Berlin, Heidelberg: Springer Berlin Heidelberg, 2008.

[75] Z. Ficek and H. S. Freedhoff, "Fluorescence and absorption by a two-level atom in a bichromatic field with one strong and one weak component," *Phys. Rev. A*, vol. 53, pp. 4275–4287, Jun 1996.

[76] I. Strandberg, Y. Lu, F. Quijandría, and G. Johansson, "Numerical study of wigner negativity in one-dimensional steady-state resonance fluorescence," *Phys. Rev. A*, vol. 100, p. 063808, Dec 2019.

[77] B. Sain, C. Meier, and T. Zentgraf, "Nonlinear optics in all-dielectric nanoantennas and metasurfaces: a review," *Advanced Photonics*, vol. 1, no. 2, pp. 024002–024002, 2019.

[78] Y. Zheng and X. Chen, "Nonlinear wave mixing in lithium niobate thin film," *Advances in Physics: X*, vol. 6, no. 1, p. 1889402, 2021.

doi:10.6342/NTU202503909

[79] S. Liu, Y. Zheng, Z. Fang, X. Ye, Y. Cheng, and X. Chen, "Effective four-wave mixing in the lithium niobate on insulator microdisk by cascading quadratic processes," *Optics letters*, vol. 44, no. 6, pp. 1456–1459, 2019.

[80] J. E. Sharping, M. Fiorentino, A. Coker, P. Kumar, and R. S. Windeler, "Four-wave mixing in microstructure fiber," *Opt. Lett.*, vol. 26, pp. 1048–1050, Jul 2001.

[81] O. Aso, M. Tadakuma, and S. Namiki, "Four-wave mixing in optical fibers and its applications," *dEp*, vol. 1, no. 2, 1999.

[82] K. Hill, D. Johnson, B. Kawasaki, and R. MacDonald, "cw three-wave mixing in single-mode optical fibers," *Journal of Applied Physics*, vol. 49, no. 10, pp. 5098–5106, 1978.

[83] Y. Li, Z. Yao, and H. Yang, "One-photon and two-photon blockades in a four-wave-mixing system embedded with an atom," *Phys. Rev. A*, vol. 109, p. 043702, Apr 2024.

[84] A. Vasenin, A. Dmitriev, S. Kadyrmetov, and O. Astafiev, "Simulation and design of a superconducting qubit for the quantum wave mixing experiment," in *AIP Conference Proceedings*, vol. 2241, AIP Publishing, 2020.

[85] A. Elistratov, S. Remizov, W. Pogosov, A. Y. Dmitriev, and O. Astafiev, "Quantum theory of wave mixing on a two-level system," *arXiv preprint arXiv:2309.01444*, 2023.

[86] H. Wang, Q. Zeng, H. Ma, and Z. Yuan, "Progress on chip-based spontaneous four-wave mixing quantum light sources," *Advanced Devices and Instrumentation*, vol. 5, p. 0032, 2024.

[87] D. Groll, D. Wigger, K. Jürgens, T. Hahn, C. Schneider, M. Kamp, S. Höfling, J. Kasprzak, and T. Kuhn, "Four-wave mixing dynamics of a strongly coupled quantum-dot–microcavity system driven by up to 20 photons," *Phys. Rev. B*, vol. 101, p. 245301, Jun 2020.

doi:10.6342/NTU202503909

[88] M. Zajnulina, B. Lingnau, and K. Lüdge, "Four-wave mixing in quantum-dot semiconductor optical amplifiers: A detailed analysis of the nonlinear effects," *IEEE Journal of Selected Topics in Quantum Electronics*, vol. 23, no. 6, pp. 1–12, 2017.

[89] J. Li, G. S. Paraoanu, K. Cicak, F. Altomare, J. I. Park, R. W. Simmonds, M. A. Sillanpää, and P. J. Hakonen, "Decoherence, autler-townes effect, and dark states in two-tone driving of a three-level superconducting system," *Phys. Rev. B*, vol. 84, p. 104527, Sep 2011.

[90] J. Li, M. A. Sillanpää, G. S. Paraoanu, and P. J. Hakonen, "Pure dephasing in a superconducting three-level system," *Journal of Physics: Conference Series*, vol. 400, p. 042039, dec 2012.

[91] T. Ramos and J. J. García-Ripoll, "Correlated dephasing noise in single-photon scattering," *New Journal of Physics*, vol. 20, no. 10, p. 105007, 2018.

[92] M. O. Scully and M. S. Zubairy, *Resonance fluorescence*, p. 291–326. Cambridge University Press, 1997.

[93] M. Lax, "Formal theory of quantum fluctuations from a driven state," *Phys. Rev.*, vol. 129, pp. 2342–2348, Mar 1963.

[94] F. Campaioli, J. H. Cole, and H. Hapuarachchi, "Quantum master equations: Tips and tricks for quantum optics, quantum computing, and beyond," *PRX Quantum*, vol. 5, p. 020202, Jun 2024.

[95] G. Khitrova, P. R. Berman, and M. Sargent, "Theory of pump–probe spectroscopy," *J. Opt. Soc. Am. B*, vol. 5, pp. 160–170, Jan 1988.

doi:10.6342/NTU202503909